DOT/FAA/TC-13/29

Federal Aviation Administration
William J. Hughes Technical Center
Aviation Research Division
Atlantic City International Airport
New Jersey 08405

Small and Large Crack Damage Tolerance Databases for Rotorcraft Materials

June 2014

Final Report

This document is available to the U.S. public through the National Technical Information Services (NTIS), Springfield, Virginia 22161.

This document is also available from the Federal Aviation Administration William J. Hughes Technical Center at actlibrary.tc.faa.gov.

U.S. Department of Transportation
Federal Aviation Administration

NOTICE

This document is disseminated under the sponsorship of the U.S. Department of Transportation in the interest of information exchange. The U.S. Government assumes no liability for the contents or use thereof. The U.S. Government does not endorse products or manufacturers. Trade or manufacturers' names appear herein solely because they are considered essential to the objective of this report. The findings and conclusions in this report are those of the author(s) and do not necessarily represent the views of the funding agency. This document does not constitute FAA policy. Consult the FAA sponsoring organization listed on the Technical Documentation page as to its use.

This report is available at the Federal Aviation Administration William J. Hughes Technical Center's Full-Text Technical Reports page: actlibrary.tc.faa.gov in Adobe Acrobat portable document format (PDF).

Technical Report Documentation Page

1. Report No.	2. Government Accession No.	3. Recipient's Catalog No.
DOT/FAA/TC-13/29		

4. Title and Subtitle	5. Report Date
SMALL AND LARGE CRACK DAMAGE TOLERANCE DATABASES FOR ROTORCRAFT MATERIALS	June 2014
	6. Performing Organization Code Mississippi State University
7. Author(s) James C. Newman, Jr., Yoshinori Yamada, Brett M. Ziegler, and Justin W. Shaw	8. Performing Organization Report No.
9. Performing Organization Name and Address Mississippi State University P.O. Box 6156 Mississippi State, MS 39762	10. Work Unit No. (TRAIS) 11. Contract or Grant No. DTFACT-06-C-00026
12. Sponsoring Agency Name and Address U.S. Department of Transportation Federal Aviation Administration Southwest Region—Aircraft Certification Service Rotorcraft Directorate 2601 Meacham Blvd. Fort Worth, TX 76137	13. Type of Report and Period Covered Final Report 14. Sponsoring Agency Code ASW-112

15. Supplementary Notes

The Federal Aviation Administration William J. Hughes Technical Center Aviation Research Division Technical Monitors were Dr. John G. Bakuckas, Jr. and Traci Stadtmueller.

16. Abstract

Rotorcraft components are subjected to high-cycle fatigue loading, in which a damage-tolerant crack (1 mm in size) may grow to failure in a short time period because of the large number of service cycles. Thus, lifing in a rotorcraft component should be accomplished by a combination of fatigue, small crack, and large crack behavior in which crack growth thresholds for small and large cracks are extremely important. Currently, for large cracks, the threshold crack growth regime is experimentally defined by using American Society for Testing and Materials (ASTM) Standard E-647, which has been shown to exhibit anomalies due to load reduction (LR) test procedures, which prematurely slows down crack growth and produce an abnormally high threshold for some materials.

The scope of this research project was to: (1) further develop the compression precracking threshold testing methods, (2) determine fatigue crack growth-(FCG) rates in the near-threshold regime and over a wide range in rates (from threshold to near-fracture) for four materials (2024-T3, 2324-T39, and 7050-T7451 aluminum alloys and 9310 steel), (3) measure crack closure (or crack opening) behavior for large cracks in the threshold regime for most of the materials considered, (4) conduct fatigue tests on two materials (7050-T7451 aluminum alloy and 9310 steel) using a new fatigue test specimen, (5) compare small and large crack behavior on several of the materials from the literature, and (6) conduct fatigue analyses on the two materials (7050-T7451 aluminum alloy and 9310 steel), using small crack theory. Three types of threshold tests were conducted on most materials: (1) the ASTM E-647 LR procedure, (2) the compression precracking constant amplitude test method, and (3) the compression precracking LR test method. Results on an additional test method, compression precracking constant-ΔK loading, were also presented on one material. All tests were conducted under a laboratory air environment at room temperature. Crack closure measurements using a local (sideface) strain gage indicated that crack closure occurred at all stress (R) ratios, even at very high-R values, where test results had been suspected to be crack closure-free data. The crack closure concept had the ability to correlate the near-threshold FCG-rate behavior onto nearly unique effective stress intensity factor range-against-rate relations. Using small crack theory, the fatigue stress-life behavior could be calculated using equivalent initial flaw sizes for several materials. Results from single-spike overloads and aircraft spectrum loading on several materials were calculated reasonably well from the strip-yield model, FASTRAN, except for the 7050-T7451 aluminum alloy that developed a very rough fatigue crack surface. Further studies are needed to develop a combined model of plasticity-, roughness-, and debris-induced crack closure behavior.

17. Key Words	18. Distribution Statement
Fatigue, Cracks, Crack growth, Thresholds, Crack closure, Stress analysis, Stress intensity factor, Fracture toughness	This document is available to the U.S. public through the National Technical Information Service (NTIS), Springfield, Virginia 22161. This document is also available from the Federal Aviation Administration William J. Hughes Technical Center at actlibrary.tc.faa.gov.

19. Security Classif. (of this report)	20. Security Classif. (of this page)	21. No. of Pages	22. Price
Unclassified	Unclassified	141	

Form DOT F 1700.7 (8-72) Reproduction of completed page authorized

TABLE OF CONTENTS

		Page
EXECUTIVE SUMMARY		xiii
1.	INTRODUCTION	1
1.1	Purpose	1
1.2	Background	2
1.3	Research Objectives	5
2.	LABORATORY TEST SPECIMENS	7
2.1	Compact	7
2.2	The SEN(B) Specimen	8
3.	MATERIALS	9
3.1	Aluminum Alloy 2024-T3	10
3.2	Aluminum Alloy 2324-T39	10
3.3	Aluminum Alloy 7050-T7451	11
3.4	Steel 9310	12
4.	TEST METHODS	12
4.1	Large Crack Testing	13
4.1.1	The BFS Gage Crack Monitoring System	13
4.1.2	The ASTM LR Threshold Testing	14
4.1.3	The CP Threshold Testing	14
4.2	Fatigue S-N Testing	21
4.2.1	Aluminum Alloy 7050-T7451	21
4.2.2	9310 Steel	22
5.	MATERIALS TESTED AND ANALYZED	23
5.1	Aluminum Alloy 2024-T3	23
5.1.1	Large Crack Behavior	23
5.1.2	Crack Closure Behavior	25
5.1.3	Crack Closure Analysis	32
5.1.4	Small Crack Behavior	36
5.1.5	Fatigue Behavior	38

5.2 Aluminum Alloy 2324-T39 42

5.2.1 Large Crack Behavior 43
5.2.2 Crack Closure Behavior 45
5.2.3 Crack Closure Analysis 51

5.3 Aluminum Alloy 7050-T7451 54

5.3.1 Large Crack Behavior 55
5.3.2 Crack Closure Behavior 56
5.3.3 Crack Closure Analysis 61
5.3.4 Small Crack Behavior 64
5.3.5 Fatigue Behavior 64

5.4 Steel 9310 69

5.4.1 Large Crack Behavior 69
5.4.2 Crack Closure Behavior 71
5.4.3 Crack Closure Analysis 73
5.4.4 Small Crack Behavior 77
5.4.5 Fatigue Behavior 79

6. ROTORCRAFT STRUCTURAL COMPONENT 81

6.1 Material 83
6.2 The CA Loading 83
6.3 Effective Stress Intensity Factor-Against-Rate Relation 84
6.4 Stress-Intensity Factor Solution for Rotorcraft Component 86
6.5 Simulated Helicopter Loading 87
6.6 Predicted Crack-Length-Against-Cycles 88
6.7 Results 89

7. CONCLUSION 90

8. REFERENCES 91

APPENDICES

A—Crack Opening Load Measurement Method
B—Stress Intensity Factor Solution for Cracks in Single-Edge-Notch-Bend Specimen
C—Machining and Heat Treatment Procedures for 9310 Steel Specimens

LIST OF FIGURES

Figure		Page
1	Expected FCG-Rate Behavior Under LR and CPCA Threshold Testing With Respect to Steady-State Behavior	3
2	Types of Compressive Loading on a Notched C(T) Specimen to Generate a Crack	4
3	Results From an ASTM LR Test and CPCA or CPLR Threshold Tests on a Ti-6Al-4V β-STOA Titanium Alloy	4
4	Small and Large Crack Data on 2024-T3 Aluminum Alloy Under $R = 0$ Conditions	6
5	Standard and Modified C(T) Specimen Configurations	7
6	Beveled or Counter-Bored Pinhole Configurations in a C(T) Specimen	7
7	Crack Front Shape Near Threshold in 4340 Steel C(T) Specimens	8
8	The SEN(B) Specimen Configuration	9
9	Definition of ASTM E-647 LR Procedure	14
10	Normalized Stress Intensity Factors for C(T) Specimen Under Compressive Loading at Pinholes or Edges	16
11	Normalized Stress Intensity Factors for Crack Emanating From V-Notch in Standard C(T) and M(T) Specimens	17
12	Crack Extension Under Compressive Loading for a Variety of Materials	18
13	Definition of CPCK Loading	19
14	Definition of CPCA Loading	20
15	Definition of CPLR Loading	20
16	Normalized Residual Stresses in SEN(B) Specimens	22
17	The FCG-Rate Data on 2024-T3 Aluminum Alloy	24
18	The C(T) Specimen With Local and Remote BFS Gages	25
19	Load-Against-Local-Strain and Reduced-Strain Record on 2024-T3 Aluminim Alloy at $R = 0.1$	26

20	Comparison of Remote and Local Strain Gage Determination of Crack Opening Loads for $R = 0.1$	27
21	Determination of Crack Opening Loads for a CPLA Threshold Test at $R = 0.1$	28
22	Determination of Crack Opening Loads for a CPLR Threshold Test at $R = 0.7$	29
23	Comparison of Remote and Local Strain Gage Determination of Crack Opening Loads for $R = 0.7$	30
24	Determination of Crack Opening Loads for a K_{max} Threshold Test	30
25	Crack Opening Load Ratios for Low R, High R, and K_{max} Test Results in Threshold Regime	31
26	Effective Stress Intensity Factor Range-Against-Rates for 2024-T3 Aluminum Alloy in the Near-Threshold Regime	32
27	Effective Stress Intensity Factor Range-Against-Rates for 2024-T3 Aluminum Alloy	33
28	Cyclic CTODs With and Without Fatigue Crack Closure	36
29	Small Crack Data and the Effective Stress Intensity Factor Range-Against-Rate Relation for 2024-T3 Aluminum Alloy	37
30	Measured and Calculated Fatigue S-N Behavior for 2024-T3 Aluminum Alloy at $R = 0.1$ on $K_t = 1$ Specimens	39
31	Fatigue Data on Circular Hole Specimens Made of 2024-T3 Aluminum Alloy Under $R = 0$ Loading	40
32	Part of the FALSTAFF Wing Spectrum	41
33	Fatigue Results on SEN(T) Specimens Made of 2024-T3 Aluminum Alloy Under Various Spectrum Loading	41
34	Fatigue Results on SEN(T) Specimens Made of 2024-T3 Aluminum Alloy Under FALSTAFF Loading	42
35	Comparison of FCG Data Generated From CPCA and CPLR Threshold Testing and Present Results	44
36	The FCG-Rate Data for Various Tests on 2324-T39 Aluminum Alloy	45
37	Comparison of Load-Reduced Strain Records Measured From Local and Remote Gages for $R = 0.1$ Loading	46

38 Reduced Load Strain Records for Several FCG Rates in Near-Threshold Conditions for $R = 0.7$ Loading 46

39 Comparison of Reduced Load Strain Records for Several FCG Rates in Near-Threshold Conditions During Constant K_{max} Test Loading 48

40 Reduced Load Strain Records for Several FCG Rates in Near-Threshold Conditions at $R = 0.9$ Loading 48

41 Crack Closure Corrected Data Using Local Strain Gages for All Tests to Form a Unique ΔK_{eff} Region and FCG Data at Extremely High R (0.95) Compared With All Other Test Data 49

42 Photographs of FCG Showing Possible Near-Crack Tip Surface Contact at $R = 0.95$ 50

43 Crack Opening Load Ratios for Low R, High R, and K_{max} Test Results in Threshold Regime 51

44 Effective Stress Intensity Factor Range-Against-Rate for the 2324-T39 Aluminum Alloy 52

45 Effective Stress Intensity Factor Range Thresholds for 2324-T39 Aluminum Alloy 53

46 Linear Elastic Stress Intensity Factor Range-Against-Rate for the 2324-T39 Aluminum Alloy 54

47 The FCG-Rate Data on the 7050-T7451 Aluminum Alloy 56

48 Load Against BFS on a C(T) Specimen Tested at Low-R on the 7050-T7451 Aluminum Alloy and Elber's Method of Determining Crack Opening Loads 57

49 Crack Opening Loads on Typical Low-R and High-R Test Cases 58

50 Crack Opening Measurements From Local Strain Gages for $R = 0.1$ Loading 59

51 Crack Opening Measurements From Local Strain Gages for $R = 0.7$ Loading 60

52 Crack Opening Measurements From Remote and Local Strain Gages for Constant K_{max} Test 60

53 The FCG-Rate Data Using Measured Crack Opening Loads on CA Tests 61

54 The FCG-Rate Data Using Calculated Crack Opening Loads on CA Tests 62

55 Comparison of FCG-Rate Data Using Measured and Calculated Crack Opening Loads 63

56 Cumulative Distribution Function for Inclusion Particle Depths on 7050-T7451 Aluminum Alloy 64

57 Fatigue Behavior Under CA Loading for the Two ΔK_{eff}-Rate Curves 65

58 Fatigue Behavior Under CA Loading for Various Initial Discontinuity Sizes Using the Lower-Bound ΔK_{eff}-Rate Curve 66

59 Fatigue Behavior Under Mini-Falstaff+ Loading for the Two ΔK_{eff}-Rate Curves 67

60 Fatigue Behavior Under Mini-TWIST+ (Level 1) Loading for the Two ΔK_{eff}-Rate Curves 67

61 Fatigue Behavior Under Mini-TWIST+ (Level 3) Loading for the Two ΔK_{eff}-Rate Curves 68

62 Suspected Crack Path After an Overload During Severe Flight Loading 68

63 The FCG-Rate Data for Constant R Tests on 9310 Steel 70

64 The FCG-Rate Data for Constant K_{max} and High R Tests on 9310 Steel 70

65 Comparison of Present FCG-Rate Data With Results From the Literature on 9310 Steel 71

66 Determination of Crack Opening Load Ratios for $R = 0.7$ CPLR Threshold Test 72

67 Determination of Crack Opening Load Ratios for Constant K_{max} Threshold Test 72

68 Effective Stress Intensity Factor Range-Against-Rate for Various Threshold Tests 73

69 Effective Stress Intensity Factor Range-Against-Rate for 9310 Steel 75

70 Effective Stress Intensity Factor Range at Threshold as a Function of Load Ratio 75

71 Elastic Fracture Toughness on C(T) Specimens as a Function of Crack Length-to-Width Ratio 77

72 Comparison of FCG-Rate Equation and Test Data on 9310 Steel 78

73 Comparison of Measured and Calculated Crack Length-Against-Cycles During Fatigue Tests on SEN(B) Specimens 79

74 Comparison of Fatigue Data From Current Testing on SEN(B) Specimens and SEN(T) Specimens From the Literature 80

75	Comparison of Measured and Calculated Fatigue Lives on SEN(B) Specimens	81
76	Complex Rotorcraft Component Used in the Round Robin Challenge Problem and Crack Configuration in the Complex Rotorcraft Component	82
77	Stress Intensity Factor Range-Against-Rate for 7010-T73651 Aluminum Alloy	84
78	Stress Intensity Factor Range-Against-Rate for 7010-T73651 Aluminum Alloy Neglecting Low *R* Threshold Data	85
79	Effective Stress Intensity Factor Range-Against-Rate for 7010-T73651/Aluminum Alloy at Various *R*	87
80	Part of the Stress Cycle History for Asterix Spectrum Loading	88
81	Measured and Predicted Crack Length-Against-Flights for Round Robin Problem	89

LIST OF TABLES

Table		Page
1	Materials and C(T) Specimen Configurations Tested and Analyzed	8
2	Materials and SEN(B) Specimen Configurations Tested and Analyzed	9
3	Chemical Composition of 2024-T3 Aluminum Alloy	10
4	Chemical Composition of 2324-T39 Aluminum Alloy	11
5	Chemical Composition of 7050-T7451 Aluminum Alloy	11
6	Chemical Composition of 9310 Steel	12
7	Effective Stress Intensity Factor Range-Against-Rate Relation for 2024-T3 Aluminum Alloy	35
8	Effective Stress Intensity Factor Range-Against-Rate Relation for 2324-T39 Aluminum Alloy	52
9	Effective Stress Intensity Factor Range-Against-Rate Relations for 7050-T7451 Aluminum Alloy	63
10	Effective Stress Intensity Factor Range-Against-Rate Relation for 9310 Steel	76
11	Effective Stress Intensity Factor Range-Against-Rate Relation for 7010-T73651 Aluminum Alloy	86

LIST OF SYMBOLS AND ACRONYMS

a	Crack depth, mm
ai	Initial crack depth, mm
a/t	Crack depth to thickness
a/c	Crack depth to crack length
B	Specimen thickness, mm
C_i	Crack growth equation coefficients
c	Crack length, mm
c_i	Initial crack length, mm
c_n	Notch length, mm
c_n/W	Notch length-to-width ratio
dc/dN	Fatigue crack growth rate, m/cycle
E	Modulus of elasticity, MPa
F	Boundary correction on stress intensity factor
Hz	Hertz
K_c	Plane-stress fracture toughness, MPa√m
K_f	Elastic-plastic fracture toughness, MPa√m
K_{Ie}	Elastic stress intensity factor at failure, MPa√m
$K_{\max}$	Maximum applied stress intensity factor, MPa√m
$K_{\min}$	Minimum applied stress intensity factor, MPa√m
K_t	Elastic stress-concentration factor
L	Length of specimen, mm
m	Elastic-plastic fracture toughness parameter
N	Number of cycles
p	Power on threshold term in crack growth equation
P	Applied load, kN
$P_{\max}$	Maximum applied load, kN
$P_{\min}$	Minimum applied load, kN
P_o	Crack-opening load, kN
q	Power on fracture term in crack growth equation
r	Radius of semicircular notch, mm
R	Stress ratio ($K_{\min}/K_{\max}$ or $P_{\min}/P_{\max}$)
R_c	Rockwell C-hardness
S	Remote applied stress, MPa
S_n	Nominal (net-section) stress, MPa
T	One-half sheet thickness for surface crack at center of notch, mm
W	Width of specimen, mm
α	Constraint factor
Δc	Crack growth increment, mm
ΔK	Stress intensity factor range, MPa√m
ΔK_o	Effective stress intensity factor range threshold, MPa√m
ΔK_{th}	Stress intensity factor range threshold, MPa√m
ΔK_{eff}	Effective stress intensity factor range, MPa√m
$(\Delta K_{\text{eff}})_T$	Effective stress intensity factor range at flat-to-slant crack growth, MPa√m
σ_o	Flow stress (average of σ_{ys} and σ_u), MPa

σ_{ys}	Yield stress (0.2 % offset), MPa
σ_u	Ultimate tensile strength, MPa
AGARD	Advisory Group for Aeronautical Research and Development
ASTM	American Society for Testing and Materials
BFS	Backface strain
CA	Constant-amplitude loading
CALR	Constant-amplitude load reduction
CMOD	Crack mouth opening displacement
CP	Compression precracking
CPCA	Compression precracking constant-amplitude
CPCK	Compression precracking constant-ΔK
CPLR	Compression precracking load reduction
C(T)	Compact specimen
CTOD	Crack tip opening displacement
D/W	Diameter-to-width
EDM	Electrical discharge machining
EIFS	Equivalent initial flaw size
FAA	Federal Aviation Administration
FCG	Fatigue crack growth
HCF	High-cycle fatigue
L-orientation	Longitudinal orientation
LaRC	Langley Research Center
LCF	Low-cycle fatigue
LR	Load reduction
LT-orientation	Longitudinal-transverse-orientation
M(T)	Middle crack tension specimen
MSU	Mississippi State University
NASA	National Aeronautics and Space Administration
OP1	One percent offset compliance
OP2	Two percent offset compliance
PICC	Plasticity-induced crack closure
RAD	Notch radius
S-orientation	Short-transverse orientation
SEN(B)	Single-edge notch bend
SEN(T)	Single-edge notched tension
S-N	Fatigue stress-life
TPFC	Two-parameter fracture criterion
VHCF	Very high-cycle fatigue

EXECUTIVE SUMMARY

Rotorcraft components are subjected to high-cycle fatigue loading in which a damage-tolerant crack (1 mm in size) may grow to failure over a short time period because of the large number of service cycles. Thus, lifing in a rotorcraft component should be accomplished by a combination of fatigue, small crack, and large crack behavior in which crack growth thresholds for small and large cracks are extremely important.

Accurate representation of fatigue crack thresholds, the region defining crack growth as either very slow or nonexistent, is extremely important for many rotorcraft applications. If the measured threshold is unconservatively high, then a structural component designed with these data may fail long before fatigue analyses predict. Currently, in North America, the threshold crack growth regime is experimentally defined by using American Society for Testing and Materials (ASTM) Standard E-647, which has been shown to exhibit anomalies due to the load reduction (LR) test procedure. The LR test procedure has been shown to induce remote crack surface closure, which prematurely slows down crack growth and produces an abnormally high threshold for some materials.

The scope of this research project was to: (1) further develop the compression precracking (CP) threshold testing methods, (2) determine fatigue crack growth (FCG) rates in the near-threshold regime and over a wide range in rates (from threshold to near fracture) for four materials (2024-T3, 2324-T39, and 7050-T7451 aluminum alloy and 9310 steel), (3) measure crack closure (or crack opening) behavior for large cracks in the threshold regime for most of the materials considered, (4) conduct fatigue tests on two materials (7050-T7451 aluminum alloy and 9310 steel) using a new fatigue test specimen, (5) compare small and large crack behavior on several of the materials from the literature, and (6) conduct fatigue analyses on the two materials (7050-T7451 aluminum alloy and 9310 steel), using small crack theory. Three types of threshold tests were conducted on most materials: (1) the ASTM E-647 LR procedure, (2) the compression precracking constant amplitude test method, and (3) the compression precracking LR test method. Results on an additional test method, compression precracking constant ΔK loading, were also presented on one material. All tests were conducted under a laboratory air environment at room temperature. Crack closure measurements using a local (sideface) strain gage indicated that crack closure occurred at all stress (R) ratios, even at very high-R values, where test results had been suspected to be crack closure-free data. The crack closure concept had the capacity to correlate the near-threshold FCG-rate behavior onto a nearly unique effective stress intensity factor range-against-rate relation. Using small crack theory, the fatigue stress-life behavior could be calculated using equivalent initial flaw sizes for several materials. Results from single-spike overloads and aircraft spectrum loading on several materials were calculated reasonably well from the strip-yield model, FASTRAN, except for the 7050-T7451 aluminum alloy that developed a very rough fatigue crack surface. Further studies are needed to develop a combined model of plasticity-, roughness-, and debris-induced crack closure behavior. In addition, the contributions of the T-stress on crack closure behavior may be needed to explain the differences between tension and bending test specimens.

1. INTRODUCTION.

The threshold stress intensity factor ranges are very important for the growth of small surface or through cracks for high-cycle rotorcraft components. However, the test procedures, which have been used in the past to generate the fatigue crack growth- (FCG-) rate data in laboratory specimens, have produced fanning with the stress ratio (*R*) in the near-threshold and threshold regimes, using bend-type specimens. During the past few years, the data generated with the standard load reduction (LR) procedure have shown configuration differences (results from tension- and bend-type specimens differ), size effects (smaller specimens have produced lower thresholds and faster FCG rates), and that environment plays a very important role in threshold development, as expected. The Federal Aviation Administration (FAA) William J. Hughes Technical Center and the Office of Naval Research have sponsored research work at Mississippi State University (MSU) and the University of Dayton Research Institute to help resolve these issues and to develop new threshold test methods—compression precracking constant-amplitude (CPCA) and compression precracking load reduction (CPLR) threshold testing. The basic flaw in the standard LR method is that the initial stress intensity factor range needed to grow a crack from a crack-starter notch has been too high, which has caused remote closure and the development of higher thresholds during the LR test. For several aluminum alloys, two titanium alloys, low-strength steel, and a superalloy (Inconel® 718), the CPCA and CPLR test procedures generated near-threshold and threshold data, which have lower thresholds and faster rates than data generated with the American Society for Testing and Materials (ASTM) LR test method. Further tests on other materials are required to see if these materials exhibit similar behavior with the stress ratio on bend-type specimens, and whether these results agree with tension-loaded specimens. These results are extremely important in verifying the transferability in fracture mechanics that allows the prediction of other crack configurations, such as cracked structural components, from laboratory specimen data. These observations have a far-reaching impact because designers have to be able to predict the crack growth behavior on complex components, which may be under tension, bending, shear, or a combination of all loading modes, from laboratory test data.

1.1 PURPOSE.

The scope of this research project was to: (1) further develop the compression precracking (CP) threshold testing methods, (2) determine FCG rates in the near-threshold regime and over a wide range in rates (from threshold to near-fracture) for four materials (2024-T3, 2324-T39, and 7050-T7451 aluminum alloys and 9310 steel), (3) measure crack closure (or crack opening) behavior for large cracks in the threshold regime for most of the materials considered, (4) conduct fatigue tests on two materials (7050-T7451 aluminum alloys and 9310 steel) using a new fatigue test specimen, (5) compare small and large crack behavior on several of the materials from the literature, and (6) conduct fatigue analyses on the two materials (7050-T7451 aluminum alloys and 9310 steel) using small crack theory.

In addition, an effort was made to validate the fracture mechanics concept of transferability from laboratory specimens to a simulated rotorcraft component. Material databases were then developed and transferred to the rotorcraft companies and to the developers of the two major life-prediction codes, NASGRO [1] and AFGROW [2].

1.2 BACKGROUND.

Accurate representation of FCG thresholds, the region defining crack growth as either very slow or nonexistent, is extremely important for many structural applications, especially high-cycle rotorcraft components. If the measured threshold is unconservatively high, then a structural component designed with these data may fail long before the fatigue analysis predicts. Currently, in North America, the threshold FCG regime is experimentally defined using ASTM Standard E-647 [3 and 4], which has been shown to exhibit anomalies due to the LR test procedure. The LR test procedure has been shown to induce remote crack surface closure [5 and 6], which prematurely slows down crack growth and produces an abnormally high threshold. However, several other investigators [7 and 8] have used other methods to generate threshold values that do not appear to have been affected by the test procedure.

The current test method defined by ASTM is designed to fully reproduce the range of FCG thresholds (e.g., low- and high-stress ratios) needed to characterize loading conditions for many structural applications. However, the thresholds determined for low-stress ratios may be abnormally high because of the LR procedure. If data generated with the LR procedure are used, this will affect the ΔK_{th}-$K_{\max}$ relationships developed by Vasudevan and Sadananda [9 and 10]. To generate FCG-rate data in the near-threshold regime for any stress ratio without LR effects, the CP method, developed over the years by Topper et al. [11], Suresh [12], Pippan et al. [13], and Forth et al. [14], was used in the current study. Using this procedure, prenotched specimens were cycled under CPCA to produce an initial crack, which naturally stops growing. Then, the specimen was subjected to constant amplitude (CA) fatigue loading to generate FCG-rate data in the near-threshold regime at the desired stress ratio and either grown to failure or grown to a low ΔK value. An LR test was then conducted.

Figure 1 shows the expected behavior for the LR procedure and the proposed CPCA loading procedure. The objective is to determine the steady-state (CA) curve (solid curve in the figure) at a constant R ratio, without any load history effects. The traditional LR scheme has been shown to induce higher ΔK_{th} thresholds than steady-state conditions [5 and 15]. Also, the thresholds have been shown to be influenced by the initial ΔK level at which the LR procedure was applied [6], as shown in figure 1. Conversely, cracks grown under the CPCA loading are fully open at the start of CA loading, rapidly slow down, and approach the steady-state curve from above. The cracks are growing because of tensile residual stresses induced by the compressive yielding at the crack-starter notch. At low initial values of ΔP_i, rates below the steady-state condition may occur in the results based on FASTRAN [16] simulations. It is estimated that the crack must be grown several compressive plastic zone sizes before steady-state conditions are met [17 and 18]. The ΔK_{eff} curve (dash-dot curve) is the ΔK-rate curve for high-R ratios and is the characteristic behavior of a fully open crack. The ΔK_{eff} curve may or may not be parallel to the steady-state curve because of three-dimensional constraint and environmental effects.

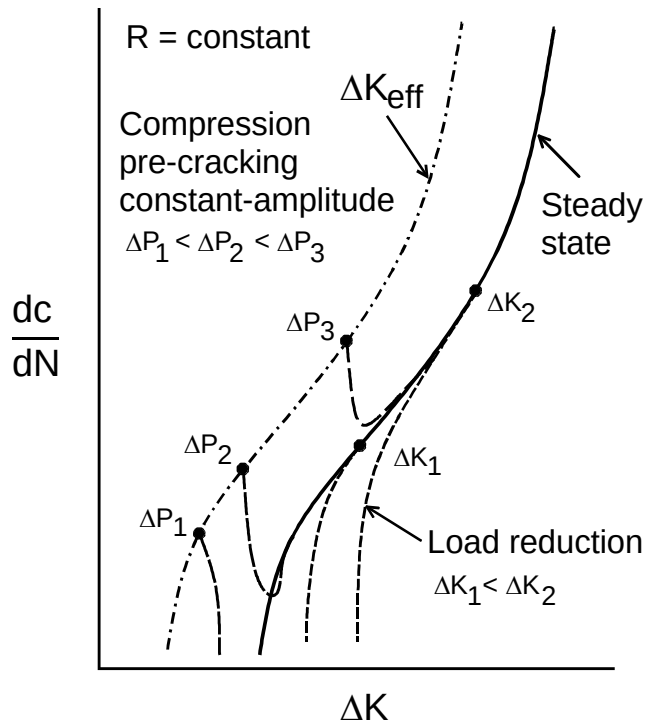

Figure 1. Expected FCG-Rate Behavior Under LR and CPCA Threshold Testing With Respect to Steady-State Behavior

There are two methods of loading that can be used to generate a compression precrack on compact C(T) specimens: either a C(T) specimen with compressive pin loading (figure 2(a)) or a C(T) specimen with the top and bottom edge-loaded (figure 2(b)). For pin loading, however, the pinholes should be mechanically polished and the compression loads must be low and applied for fewer than 100,000 cycles to prevent pinhole cracking. The pin-loading method is preferred because the compressive stress intensity factors are of slightly larger magnitude than for block loading and this method simplifies testing. Compression precracks grow to about 40% of the compressive plastic zone size [17]. The specimens are then subjected to standard tensile cyclic pin loading at the desired CA loading and the cracks are grown either to failure or to a specified ΔK value before an LR test is conducted.

Some typical FCG-rate data generated on a Ti-6Al-4V β-STOA titanium alloy [19] are shown in figure 3. These tests were conducted at an *R*-ratio of 0.4. The results from four types of tests (CPCA, CPLR, CA, and constant-amplitude load reduction (CALR)) are shown as symbols with lines. The CPCA, CPLR, and CA tests generally agreed from threshold to very high rates. Conversely, the ASTM LR test (diamond symbols) began to deviate from the other test data at rates below the ASTM maximum rate requirement. The crack was grown under CA loading to a 1E-08 m/cycle rate and the LR test was conducted. The results produced a threshold of about 6.3 MPa-m$^{1/2}$, whereas the CPLR threshold test produced a threshold value of about 4 MPa-m$^{1/2}$. Also, the CPCA test produced significantly higher rates over a significant portion of the ΔK-rate curve and even the slope of the ΔK-rate data in the midrate regime. These results show that the ASTM test procedure needs to be modified so that the load history effects from the test data can be removed. The large variations in the data are due to the use of the secant method to reduce

data instead of the seven-point polynomial smoothing method. The secant method is more sensitive to metallurgical features than the polynomial smoothing method. The β-STOA alloy has a very large grain structure and the large grains cause meandering and bifurcating cracks.

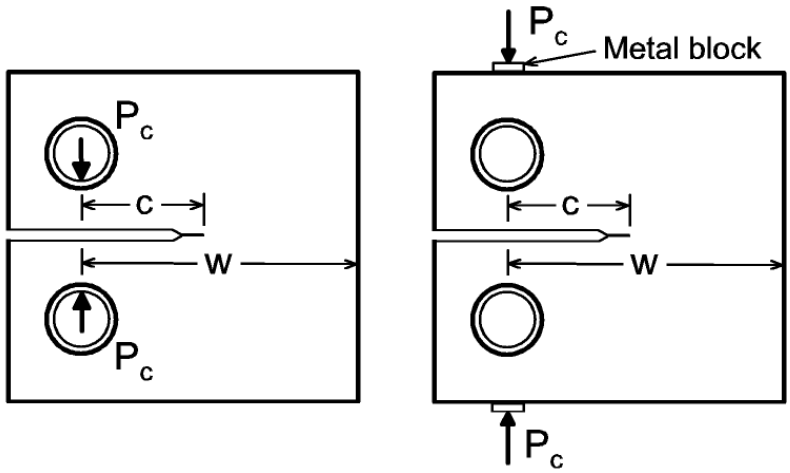

(a) Pin loading (b) Block loading

Figure 2. Types of Compressive Loading on a Notched C(T) Specimen to Generate a Crack

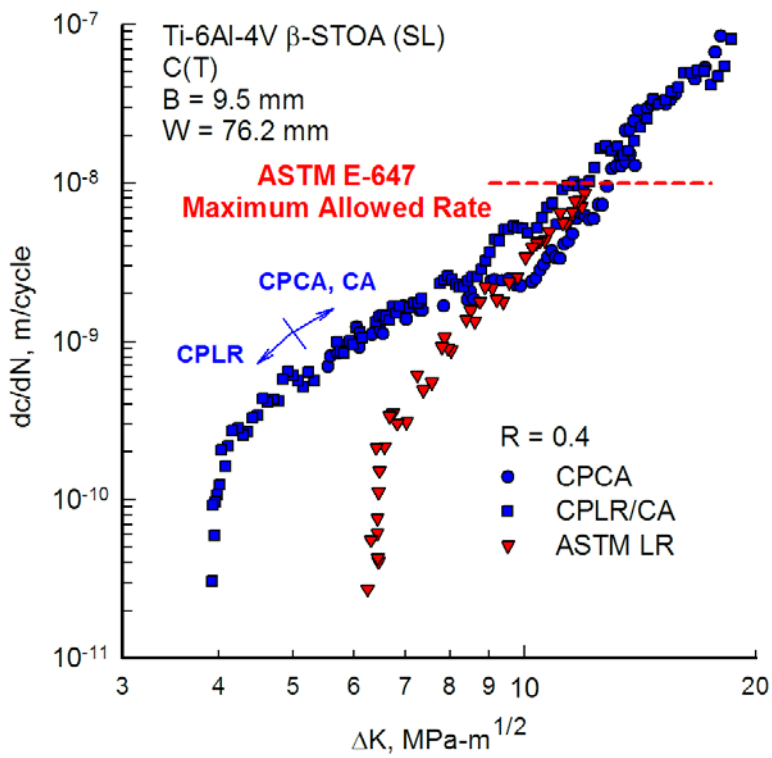

Figure 3. Results From an ASTM LR Test and CPCA or CPLR Threshold Tests on a Ti-6Al-4V β-STOA Titanium Alloy

During the past few years, the National Aeronautics and Space Administration (NASA) Langley Research Center (LaRC), with FAA support, has developed a small crack monitoring system [20]. Recently, the system has been successfully applied to small crack growth in 4340 steel using the Advisory Group for Aeronautical Research and Development (AGARD) single-edge notched tension specimen (SEN(T)) [21]. The SEN(T) specimen has a semicircular edge notch with a stress concentration factor (K_T) of about 3.2 that simulates the stresses around a fastener hole. The small crack monitoring system can locate and monitor cracks as small as 50 μm (0.002 inches) and the data compared well with the AGARD data (AGARD R-767 [21]), generated with the plastic replica method. In addition, the NASA researchers use a more reliable replica method, which employs a silicone-based material to find extremely small cracks. The researchers at NASA LaRC and their colleagues in Europe and China have been instrumental in the development of small crack methodology in a wide variety of materials and loading conditions during the 1984 to 1994 time frame [21-23].

The small crack data that were generated by AGARD [21 and 22] and NASA/Chinese Aeronautical Establishment [23] test programs showed that small cracks grow below the large crack threshold and that they grow at higher rates than large cracks. However, the large crack data were generated on middle crack tension (M(T)) specimens using the ASTM LR test procedures. Figure 4 shows some typical data on the 2024-T3 aluminum alloy sheet material. The small crack data were generated on surface cracks in the SEN(T) specimens, and the large crack data were on M(T) specimens. The large crack data showed a threshold at about 3.2 MPa-$m^{1/2}$, whereas the small crack data grew significantly below the large crack threshold and had a small crack threshold below 1 MPa-$m^{1/2}$. The question is if the large crack data would be influenced by the LR test procedure, as shown for the C(T) specimen data in figure 3, and if the steady-state constant amplitude data, using the new CPCA and/or CPLR procedures, are closer to the small crack data. No C(T) data had ever been generated on the 2024-T3 or 7075-T6 materials from the NASA LaRC special stock. Because large crack data on M(T) specimens and small crack data have been generated on both the 2024-T3 and 7075-T6 aluminum alloy materials, C(T) specimen data using the various threshold test procedures (CALR, CPCA, and CPLR) would help to answer some of these questions. However, there are small crack effects in the microstructural range (5 to 100 μm), but the differences between small crack data and load-history-free large crack data may be closer than shown in the current literature.

1.3 RESEARCH OBJECTIVES.

FCG tests using C(T) specimens were conducted on all materials. These tests were used to generate FCG-rate data from threshold to near fracture. The three types of threshold tests conducted on most materials were: (1) the ASTM E-647 LR procedure, (2) the CPCA test method, and (3) the CPLR test method. Results on an additional test method, compression precracking constant-ΔK (CPCK) loading, were also presented on one material. All tests were conducted under a laboratory air environment at room temperature.

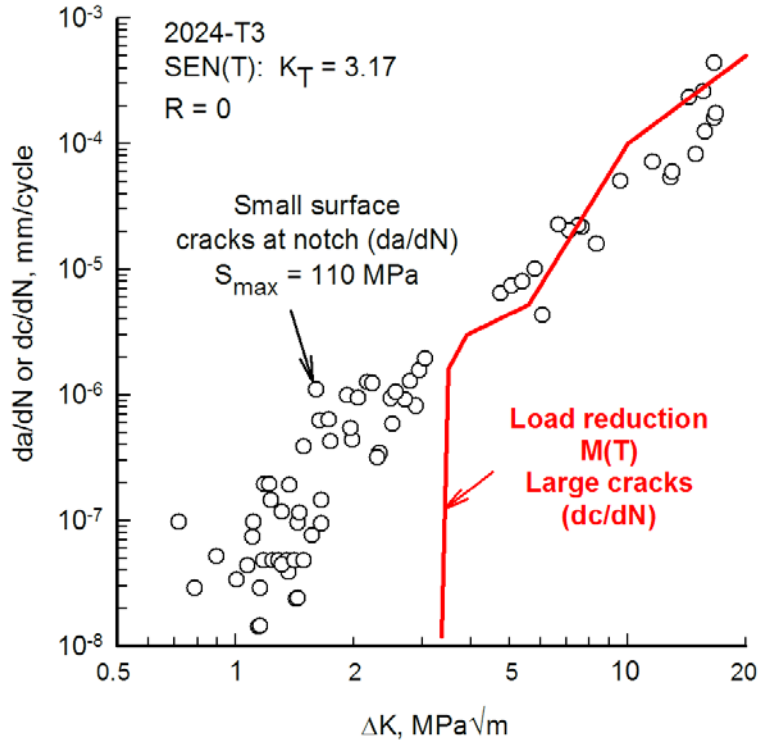

Figure 4. Small and Large Crack Data on 2024-T3 Aluminum Alloy Under R = 0 Conditions

The crack closure concept is widely used to correlate large FCG-rate data generated on these large crack test specimens. In the past, remote methods, such as the crack mouth opening displacement (CMOD) gage or backface strain (BFS) gage, have been used to measure crack opening loads. Yamada and Newman [24-27] have shown that local (sideface) strain gages give more reliable crack opening loads than the remote methods. The method used to determine the crack opening loads, which is Elber's method [28], is described in appendix A. The crack opening load method (the 2% offset compliance method (OP2)) presented in ASTM E-647 did not give reliable values, especially for high-stress ratios. Crack closure measurements using a local strain gage (about one-sheet thickness away from the crack tip and slightly below the anticipated crack path) indicated that crack closure occurred at all stress (R) ratios, even at very high R values, for which test results had been suspected to be crack closure-free data. The crack closure concept was able to correlate the near-threshold FCG-rate behavior onto a nearly unique effective stress intensity factor range-against-rate relations for all materials studied.

Fatigue tests were also conducted on two of the materials used in this study, 7050 aluminum alloy and 9310 steel. Tests were conducted under both CA and spectrum loading. Small crack growth was also monitored in the 9310 steel single-edge notch bend (SEN(B)) specimens. Small crack theory was used to calculate the fatigue stress-life (S-N) behavior using an equivalent initial flaw size (EIFS) for the two materials.

2. LABORATORY TEST SPECIMENS.

Two test specimens were used at MSU to generate fatigue data and FCG-rate data on a variety of materials used in the rotorcraft industry. Fatigue tests were conducted on SEN(B) specimens. The SEN(B) specimen is a new fatigue specimen that is subjected to tensile pin loading and the semicircular edge notch produces a high stress-concentration factor due to the induced bend on the net section. The FCG tests were conducted on standard C(T) specimens.

2.1 COMPACT.

Test specimens used were standard plan form C(T) specimens (figure 5), although the MSU tests had beveled or counter-bored pinholes to help minimize the out-of-plane bending influence on crack front shapes in threshold testing.

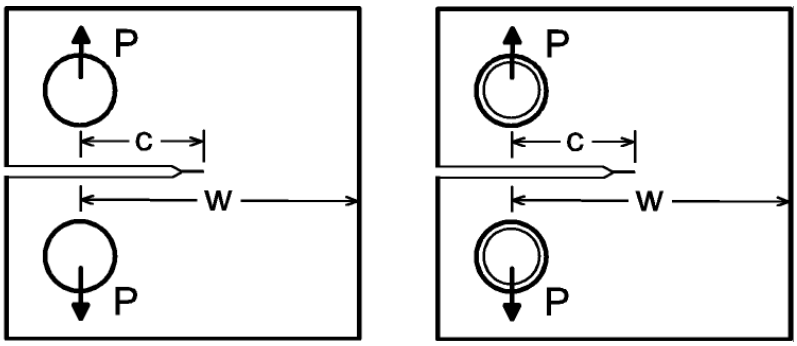

(a) Standard pinholes (b) Beveled pinholes

Figure 5. Standard and Modified C(T) Specimen Configurations

Because of slight misalignments in the compact clevis pinhole-loading fixtures, the pin may contact the outer edges of the pinholes and cause out-of-plane bending on the specimen. Thus, stress intensity factors at the crack tip on one side of the specimen would be higher than on the other side and cause a nonstraight crack front. The beveled or counter-bored pinhole (figure 6) causes the pin to automatically contact near the centerline of the specimen. This reduces the out-of-plane bending and produces a straighter crack front on 4340 steel C(T) specimens (figure 7).

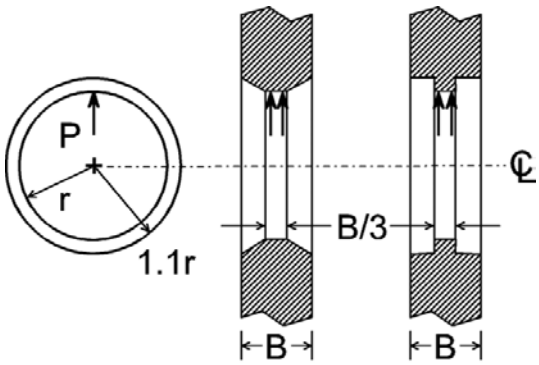

Figure 6. Beveled or Counter-Bored Pinhole Configurations in a C(T) Specimen

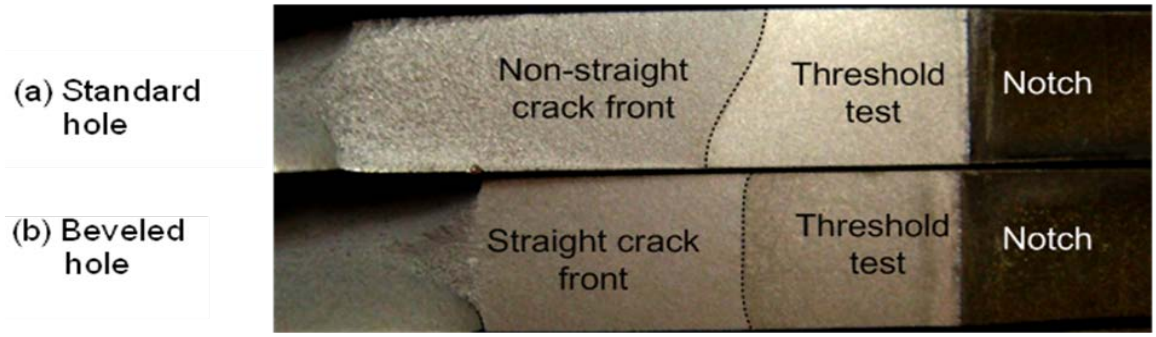

Figure 7. Crack Front Shape Near Threshold in 4340 Steel C(T) Specimens

One specimen had the standard pinhole configuration and produced a nonstraight crack front as the threshold condition was approached; however, the specimen with the beveled pinholes produced nearly a straight crack front during a similar threshold test.

The C(T) specimens tested at MSU were either nominally 51 or 76 mm (W) wide. The crack-starter V-notch had either a 45- or 60-degree included notch-tip angle. The notch length-to-width (c_n/W) ratio varied from 0.33 to 0.35 to increase the sensitivity of the BFS gage crack-monitoring system. The 7050 aluminum alloy C(T) specimens had c_n/W = 0.2.

A summary of the materials and C(T) specimen configurations tested at MSU are reviewed in table 1.

Table 1. Materials and C(T) Specimen Configurations Tested and Analyzed

Material	Alloy and Temper	*B*, mm	*W*, mm
Aluminum alloy	2024-T3	2.3	76 or 152
Aluminum alloy	2324-T39	6.35	76
Aluminum alloy	7050-T7451	6.35	51
Steel	9310	6.35	76

2.2 THE SEN(B) SPECIMEN.

The SEN(B) specimen (figure 8) was developed for performing fatigue and small crack testing using the equipment available in the Fatigue and Fracture Laboratory at MSU. Because all of the servohydraulic fatigue test frames use pin-loading clevises, a pin-loaded fatigue specimen was needed. The design of this specimen centered on modifying the SEN(T) specimen, which is a standard one used in the study of small cracks [21-23]. One major advantage for the SEN(B) specimen is a larger stress concentration factor at the notch, K_T = 11.8, compared to K_T = 3.17 for the SEN(T). This makes it possible to run a test at the same local stress level using a much lower applied load. Even with the high-stress concentration factor, the normal stress distribution near the notch is very similar to the SEN(T) specimen.

Because the SEN(B) specimen is used for testing the behavior of small surface cracks, the specimen configuration must allow for easy access to the notch surface for both visual inspection and the application of crack surface replication material. For this reason, it was important to consider how the specimen configuration fits together with the test frame clevises. As figure 8 shows, the SEN(B) configuration allows for easy access to the notch with no interference from the clevises. The initial design for the SEN(B) specimen had a test section that was 25.4 mm wide (W) and a total specimen length (L) of 190 mm. However, an opportunity arose for the SEN(B) specimen to be made from a 7050-T7451 aluminum alloy forging block, but the specimen was limited to 140 mm (L). To retain the specimen width (W = 25.4 mm), the specimen geometry was altered, including a change in total length and pinhole diameter. These changes were made with the assumption that the changes would not alter the stress concentration at the notch or the stress intensity factors for a crack at the semicircular edge notch. Having two complete sets of machined SEN(B) specimens, it was necessary to perform an elastic stress analysis for the new specimen with two different configurations. From the elastic stress analyses, it was found that the stress concentration factors and crack stress intensity factors were nearly identical (see appendix B).

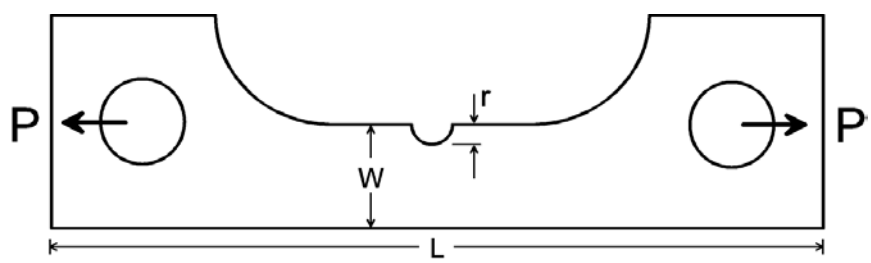

Figure 8. The SEN(B) Specimen Configuration

A summary of the materials and SEN(B) specimen configurations tested at MSU are reviewed in table 2.

Table 2. Materials and SEN(B) Specimen Configurations Tested and Analyzed

Material	Alloy and Temper	*L*	*r*, mm	*B*, mm	*W*, mm
Aluminum alloy	7050-T7451	5.5W	3.18	6.35	25.4
Steel	9310	7.5W	3.18	6.35	25.4

3. MATERIALS.

A number of materials that are used in the rotorcraft industry were used to generate fatigue S-N data and FCG-rate data over a wide range in stress ratios ($R = P_{min}/P_{max}$) from threshold to near-fracture. Those materials were: 2024-T3, 2324-T39, and 7050-T7451 aluminum alloys, and 9310 steel.

3.1 ALUMINUM ALLOY 2024-T3.

The 2024-T3 aluminum alloy material was obtained from NASA LaRC from a special stock of thin-sheet material that had been well characterized over the past 40 years [29-31]. All specimens were machined and tested in the longitudinal-transverse (LT)-orientation (crack plane perpendicular to the rolling direction). The chemical composition of this alloy is listed in table 3.

The tensile properties were obtained from ASTM Standard E8 specimens [29 and 32]. The average yield stress (0.2% offset) was 355 MPa, the ultimate tensile strength was 490 MPa, and the modulus of elasticity was 71.8 GPa.

Table 3. Chemical Composition of 2024-T3 Aluminum Alloy

Element	Symbol	Percentage
Aluminum	Al	Balance
Chromium	Cr	Max 0.1%
Copper	Cu	3.8-4.9%
Iron	Fe	Max 0.5%
Magnesium	Mg	1.2-1.8%
Manganese	Mn	0.3-0.9%
Silicon	Si	Max 0.5%
Titanium	Ti	Max 0.15%
Zinc	Zn	Max 0.25%
Others		Max 0.2%

3.2 ALUMINUM ALLOY 2324-T39.

The 2324-T39 aluminum alloy specimens were obtained from Alcoa, Inc. All specimens were tested in the LT-orientation (crack plane perpendicular to the rolling direction). The chemical composition of this alloy [33] is listed in table 4. The average yield stress (0.2% offset) was 408 MPa, the ultimate tensile strength was 519 MPa, and the modulus of elasticity was 72.4 GPa.

Table 4. Chemical Composition of 2324-T39 Aluminum Alloy

Element	Symbol	Percentage
Aluminum	Al	Balance
Chromium	Cr	Max 0.1%
Copper	Cu	3.8-4.4%
Iron	Fe	Max 0.12%
Magnesium	Mg	1.2-1.8%
Manganese	Mn	0.3-0.9%
Silicon	Si	Max 0.5%
Titanium	Ti	Max 0.15%
Zinc	Zn	Max 0.25%
Others		Max 0.2%

3.3 ALUMINUM ALLOY 7050-T7451.

NASA LaRC machined all of the 7050-T7451 C(T) specimens from a 152-mm-thick forging block that had been obtained in an overaged T7451 heat-treat condition per specification American Society for Metals 4050G. Table 5 shows the chemical composition of this alloy [33]. A significant number of C(T) specimens were provided to MSU. The remaining forging block was also provided to MSU to machine the SEN(B) specimens. Tensile tests were conducted according to ASTM Standard E8 using 6.4-mm round-bar tension specimens. The specimens were tested in the both the L-(longitudinal) and S-(short-transverse) orientations at room temperature. The yield stress, ultimate tensile strength, and modulus of elasticity were calculated from two tests for each orientation. For the L-orientation at room temperature, the yield stress was 470 MPa, the ultimate tensile strength was 525 MPa, and the modulus of elasticity was 76 GPa.

Table 5. Chemical Composition of 7050-T7451 Aluminum Alloy

Element	Symbol	Percentage
Aluminum	Al	Balance
Chromium	Cr	0.04%
Copper	Cu	2.0-2.6%
Iron	Fe	0.15%
Magnesium	Mg	1.9-2.6%
Manganese	Mn	0.1%
Silicon	Si	0.12%
Titanium	Ti	0.06%
Zinc	Zn	5.7-6.7%
Zirconium	Zr	0.08-0.15%
Others		0.2%

3.4 STEEL 9310.

A 9310 steel rod (150-mm diameter by 750-mm long) was provided by the Boeing Company. The C(T) and SEN(B) specimens were machined from the rod in the LR-(longitudinal direction of maximum grain flow) orientation and heat-treated by procedures described in appendix C. Table 6 shows the chemical composition of this alloy [34].

Table 6. Chemical Composition of 9310 Steel

Element	Symbol	Percentage
Carbon	C	0.1%
Chromium	Cr	1.2%
Iron	Fe	Balance
Manganese	Mn	0.5%
Molybdenum	Mo	0.12%
Nickel	Ni	3.25%
Silicon	Si	0.25%
Others		0.2%

Tensile properties were not obtained on this particular material. The stated yield stress and ultimate tensile strength were from 1070 to 1200 MPa, respectively. The tensile properties (yield stress and ultimate tensile strength) are important in the fracture toughness assessment of the steel.

4. TEST METHODS.

In generating FCG-rate data (crack-length-against-cycles) on metallic materials, various test methods have been used over the past 35 years (see ASTM E-647 [3]). The primary goal has been to determine the CA FCG-rate behavior at various mean and alternating load conditions. However, to generate FCG-rate data in the near-threshold regime, CA conditions have not been able to initiate a crack at a crack-starter notch at the extremely low-stress intensity factors required. Thus, Paris et al. [35], Schmidt and Paris [36], Hudak et al. [4], and Bucci [37] developed an LR scheme to initiate cracks at higher stress intensity factor ranges and slowly reduce the ΔK range until the near-threshold and threshold behavior has been obtained. The LR procedure assumed that the FCG-rate was totally controlled by the ΔK value. This procedure was standardized in ASTM E-647 and has been used for over 25 years to generate FCG-rate data from threshold to fracture conditions. Herman et al. [38] developed an LR procedure to reduce ΔK (by reducing the load amplitude), but held the K_{max} value constant. This procedure generated low crack growth rates at very small ΔK values, but the stress ratio near and at threshold was extremely high, generally greater than 0.9. Procedures to maintain a constant ΔK value have also been used to study environmental effects. This procedure, which is also an LR procedure to maintain a constant ΔK value as the crack grows, has been widely used. All of these methods assume that the crack tip behavior is totally controlled by the stress intensity factor range.

However, fatigue crack closure under cyclic loading [39] causes the load history to have an influence on FCG-rate behavior, such as the plastic wake and residual stresses. Thus, the stress intensity factor range does not control FCG. Contact of the crack surfaces and residual stresses in the plastic zone influences the FCG-rate behavior. Since Elber's discovery of plasticity-induced crack closure (PICC), several other closure (or crack tip shielding) mechanisms, such as fretting debris- and roughness-induced crack closure (DICC and RICC), have been discovered, discussed, and modeled [40-42]. The test environment, even laboratory air, has a tremendous influence on the crack growth mechanisms that are activated, which can influence the crack closure behavior and must be considered in developing any damage tolerance life prediction method.

During the past decade, there has been a renewed interest in using CP test procedures, as proposed by Hubbard [43], Topper and Au [11 and 44], Suresh [12], Pippan et al. [13 and 45], Forth et al. [14 and 46], Newman et al. [47 and 48], and Ruschau and Newman [49], to generate a crack under compressive loading and then to apply either a small stress intensity factor range or small CA slightly above the steady-state ΔK threshold at a given stress ratio. This test procedure should generate FCG-rate data in the near-threshold regime that minimizes any load history effects, after the crack has grown several compressive plastic zone sizes [47-50].

Two FCG-rate test methods are presented and discussed below: (1) ASTM LR threshold testing and (2) CP threshold testing. After CP, there are three loading procedures: (a) CPCA, (b) CPLR, and (c) CPCK. Each of these methods will be briefly presented.

4.1 LARGE CRACK TESTING.

All large crack tests of C(T) specimens were conducted using 25 kN servohydraulic test frames under laboratory air and room temperature conditions. The test frequency in the near-threshold regime was 18 hertz (Hz), but the frequency was generally lowered to about 5 to 10 Hz at higher rates approaching fracture. Crack lengths were visually monitored with a traveling microscope to validate data taken with an FTA crack monitoring system [51].

4.1.1 The BFS Gage Crack Monitoring System.

Crack lengths in all C(T) specimens were monitored by using an improved BFS gage relation [52]. Compliance relations were developed between the BFS and the crack length (c) specimen width (W) specimen thickness (B) material elastic modulus (E) and the applied load (P). Two stress analysis codes (finite element and boundary element) were used to obtain numerical results over a wide range in c/W ratios. An equation fit to the numerical results is given by:

$$c/W = A_0 + A_1 U + A_2 U^2 + A_3 U^3 + A_4 U^4 + A_5 U^5 \qquad (1)$$

where $U = 1/(\sqrt{A} + 1)$ and $A = |\varepsilon EBW/P|$ for $0.2 < c/W < 0.95$. Equation 1 is within ±0.2% of the numerical results over a wide range in c/W ratios. The validity of equation 1 for very deep cracks ($0.77 < c/W < 0.93$) was verified on tests conducted on several materials [52].

4.1.2 The ASTM LR Threshold Testing.

The current LR test method defined by ASTM E-647 is designed to fully reproduce the range of fatigue crack thresholds (e.g., low- and high-stress ratios) needed to characterize loading conditions for many structural applications. The ASTM LR test procedure [3] was based on stress intensity factors changing at an exponential rate. A typical LR example is shown in figure 9. The ratio of the current applied load (P_{max}) to the initial applied load $(P_{max})_i$ is plotted against crack length. The solid curves are based on a constant rate of change in normalized plastic zone size with crack extension. The normalized K-gradient, $(dK/dc)/K$, was -0.08 mm^{-1} for the upper solid curve, as recommended in the standard. This is equivalent to a 5% change in stress every 0.5-mm of crack extension, as shown by the stair-step lines. The standard also allows a 10% change every 0.5-mm of crack extension; if computerized, smooth LR capability is not available. This is equivalent to a normalized K-gradient of -0.2 mm^{-1}, as shown by the lower solid curve. These procedures have been used over the past 25 years to generate FCG thresholds for a wide variety of materials.

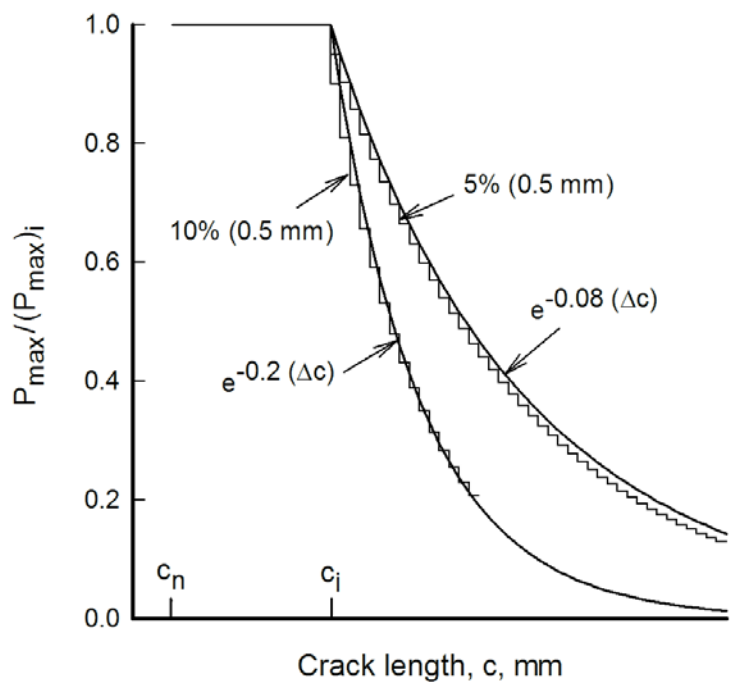

Figure 9. Definition of ASTM E-647 LR Procedure

4.1.3 The CP Threshold Testing.

For CP threshold testing, the test specimen must have a sharp V-notch so compressive yielding at the notch root tip will induce tensile residual stresses to grow the crack under compression loading. To establish the validity criteria for crack growth from the notch, several issues must be resolved. First, the stress intensity factors for a crack under compressive loading (without surface contact) must be determined. Second, the effects of the crack-starter V-notch on stress intensity factors must be calculated. The minimum compressive loading needed to initiate a crack at the V-notch must be established. Finally, the amount of crack growth from the notch tip

needed to have no (or minimal) influence of the tensile residual stresses on crack growth and the amount of crack growth for crack closure behavior to stabilize under CA loading.

For CP threshold testing, there are three loading options after CP: (1) constant stress intensity factor range testing, (2) CA load testing, and (3) standard LR testing after crack growth CA loading to meet specified crack extension criteria.

4.1.3.1 Stress Intensity Factors Under Compressive Loading.

Figure 2 in section 1.2 shows the two methods by which C(T) specimens were tested under compression loading to initiate a small fatigue crack (0.1 to 0.5 mm in length) at the crack-starter V-notch. In the first method, the standard pins are used to apply compressive loads (figure 2(a)). Here, the pins must contact the holes before the loading clevis contacts. Using this method, the pinholes have been known to crack if high compressive loads are used and if they are applied for a large number of cycles. To help prevent pinhole cracking, the lower portion of the pinhole surfaces was polished, low compressive loads were used, and fewer than 100,000 cycles were applied. The beveled holes may also induce pinhole cracking due to the higher-bearing stresses. Pinhole loading is the preferred method to simplify the testing procedures.

In the second method, small aluminum blocks were bonded to the top and bottom of the specimen edges along the load line so the blocks would contact before the loading clevis (figure 2(b)). The standard pins were removed and smaller diameter pins were installed as safety pins to prevent the specimen from coming out of the fixture during compressive loading. Typically, fewer than approximately 60,000 cycles are required to initiate a crack at the V-notch for a wide variety of materials under the specified compressive loading (discussed in section 4.1.3.3). The crack would grow and naturally develop into a nonpropagating crack, as the crack closure levels approached the threshold conditions under cyclic compression.

A boundary element code, FADD2D [53], was used to calculate the stress intensity factor (K) for cracks under compressive loading (figure 2(a)). Crack surface contact was not modeled and the stress intensity factors were negative. Normalized stress intensity factors are shown in figure 10 as a function of the crack-length-to-width (c/W) ratio. K_{CT} is the stress intensity factor solution for the standard C(T) specimen [3]. The compressive pin loading gave higher absolute stress intensity factors than standard pin loading (figure 5) for $c/W<0.5$, whereas the C(T) configuration with compressive loading applied at the top and bottom edges of the specimen gave essentially the same absolute stress intensity factor solution as the standard specimen (0.5% for $0.2 \leq c/W \leq 0.7$).

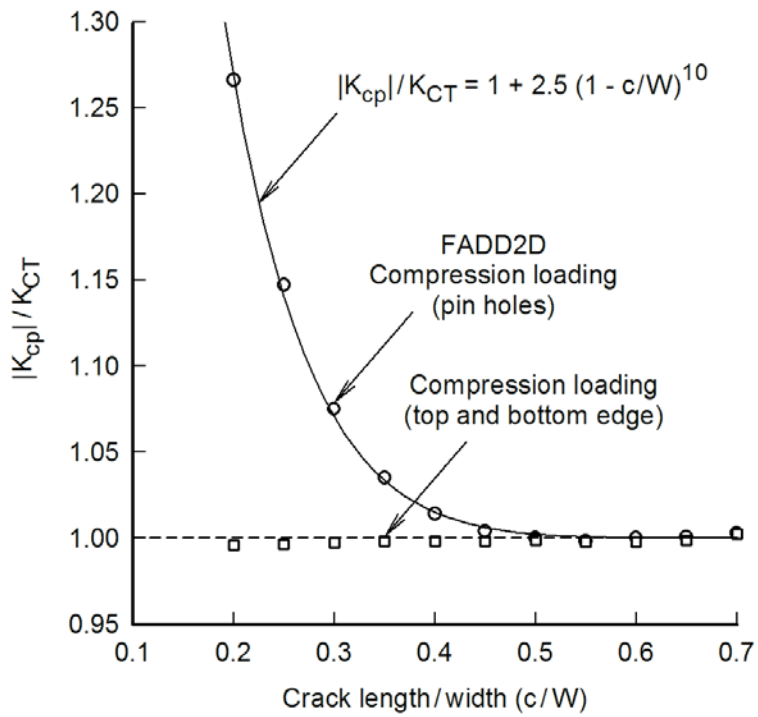

Figure 10. Normalized Stress Intensity Factors for C(T) Specimen Under Compressive Loading at Pinholes or Edges

4.1.3.2 V-Notch Effects on Stress-Intensity Factors.

Figure 11 shows the results of boundary element analyses of standard C(T) and M(T) specimens with a small crack emanating from a crack-starter V-notch with a notch root radius of 0.2 mm. Boundary element analyses were conducted with the FADD2D code [53] and additional results were provided by Mark James (NASA LaRC; unpublished) using the FRANC2DL finite element code [54]. Crack extension from the V-notch is denoted as Δc. The stress intensity factor for a crack emanating from the V-notch, K_N, is normalized by the standard stress intensity factor (K) solution for the C(T) specimen [3] or the M(T) specimen [55]. Calculations have been made for either a 45- or 60-degree notch for a 76-mm-wide specimen with a notch length-to-width (c_n/W) ratio of 0.25 (note that W is the width of the C(T) specimen and $2W$ is the total width of the M(T) specimen). The notch height, h_n, was 2.54 mm (W/h_n = 30). For crack lengths greater than or equal to $0.5h_n$ from the V-notch tip, the stress intensity factors were within about 1% of the standard K solutions for C(T) and M(T) specimens. Stress intensity factors approach the standard K solution for crack lengths greater than $0.5h_n$. Although these results here are for c_n/W = 0.25, it is expected that the ratio of K_N/K_{CT} or K_N/K_{MT} would have similar behavior to that of larger c_n/W ratios. However, the intent is not to account for the effects of the notch on stress intensity factors, but to grow the crack beyond the influence of the notch.

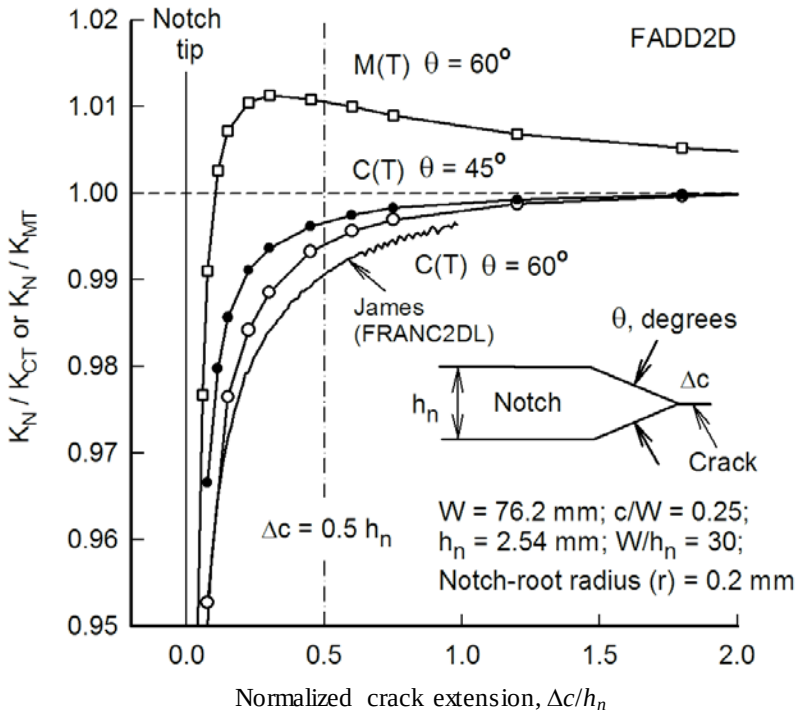

Figure 11. Normalized Stress Intensity Factors for Crack Emanating From V-Notch in Standard C(T) and M(T) Specimens

4.1.3.3 Crack Growth Under Compressive Loading.

The measured crack extension (Δc) during cyclic compression on a variety of materials, is shown in figure 12 as a function of the normalized compressive stress intensity factor, $|K_{cp}|/E$. Because the tensile residual stress zone is proportional to the compressive plastic zone size, the objective was to find the smallest compressive loading that would initiate a fatigue crack at the V-notch tip with a reasonable root radius in a variety of materials. Thus, the affected zone of residual stresses and the amount of crack extension required for valid FCG-rate data (unaffected by residual stresses) would be minimized. The maximum compressive stress intensity factor (K_{cp}) level has been reduced by a factor of two [56] from values previously used on a variety of materials [17 and 19]. Thus, a range of $|K_{cp}|/E$ values has been found to produce reasonably sized fatigue cracks and is given by:

$$|K_{cp}| / E = 0.00015 \text{ to } 0.0003 \sqrt{\text{m}} \tag{2}$$

where E is the modulus of elasticity, MPa (see dashed vertical lines in figure 12). Recently, the lower-bound $|K_{cp}|/E$ value has been found to provide reasonable compression precracks in two aluminum alloys and in low-strength steel. Further study will help validate whether the lower-bound is adequate on other materials.

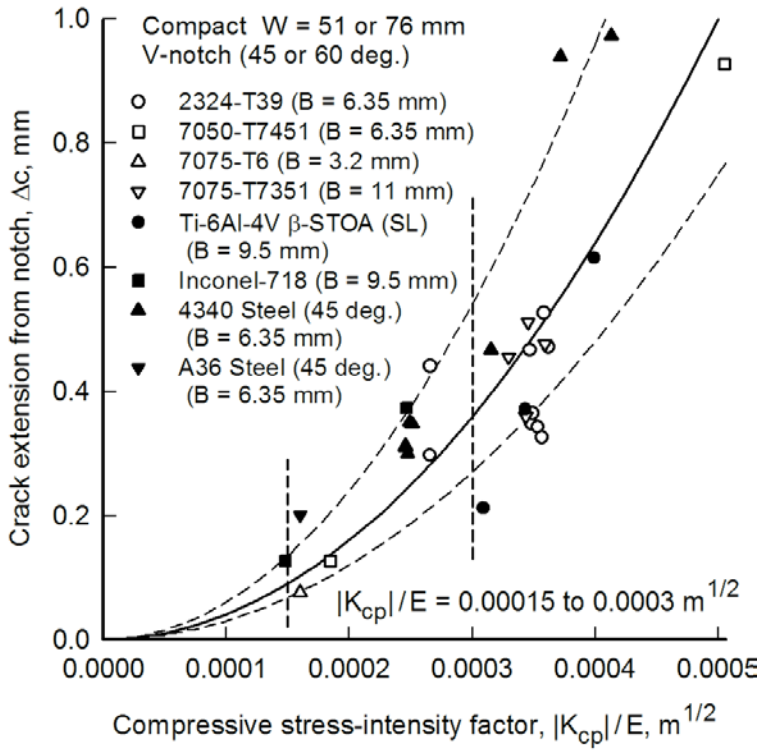

Figure 12. Crack Extension Under Compressive Loading for a Variety of Materials

4.1.3.4 The CPCK and Crack Extension Criteria.

For most of the materials and C(T) specimens in this study, the minimum compressive loading was selected as $|K_{cp}|/E$ = 0.0003 √m (0.0019 √in.). The K_{cp} is calculated from the minimum compressive load (P_{cp}) to be applied to the particular crack configuration. For C(T) specimens, the load ratio ($R = P_{cp}/P_{max}$) may be between 8 and 16; approximately 30,000 to 60,000 cycles are required to initiate a crack at the V-notch in a variety of materials. The precrack length must be grown beyond the influence of the V-notch, the tensile residual stress field caused by compressive yielding, and the stabilization of the crack closure behavior under CA loading. Based on finite element analyses [18 and 50] and CP testing on a variety of materials [17, 19, and 24-27], the crack extension criterion was selected as:

$$\Delta c \geq 3\,(1 - R)\,\rho_c \tag{3}$$

and

$$\Delta c \geq 0.5\,h_n \tag{4}$$

(whichever is the largest—ρ_c is the plane stress compressive plastic zone size and h_n is the notch height). Equation 3 usually controls the amount of crack extension, beyond which valid FCG rates are produced. However, using the lower-bound in equation 2, the minimum amount of crack extension may be controlled by equation 4. The plastic zone size is calculated from the Dugdale model [57] and is given by:

$$\rho_c = (\pi/8)\,(|K_{cp}| / \sigma_o)^2 \tag{5}$$

where σ_o is the flow stress and is the average between the yield stress, σ_{ys}, and ultimate tensile strength, σ_u.

4.1.3.5 CPCK Testing.

Researchers at NASA LaRC have proposed using a CP method, which is basically a *K*-controlled test, as shown in figure 13. Using a notched specimen, a cyclic compressive loading would be applied to initiate a crack at the notch, after which the specimen would be subjected to a constant ΔK (above the apparent ΔK_{th} threshold) for a given *R* value. The compressive loading, which yields the notch root, induces a tensile residual stress in front of the notch. The objective in using this technique was to identify the extent of the influence of these residual stresses. However, this technique is also an LR procedure because the applied loading has to be decreased with larger crack lengths to maintain the constant ΔK value.

4.1.3.6 CPCA Testing.

The CPCA procedure, as shown in figure 14, was designed to generate FCG rates in the near-threshold regime under CA conditions with minimal load history effects. This type of loading has been demonstrated to produce fatigue cracks at machined notches with minimal load history effects on both C(T) and M(T) specimens [46-49]. Once a fatigue crack has been initiated at the notch root, then small tensile loading can be applied to grow the crack under steady-state CA loading from threshold to fracture conditions. Currently, trial and error procedures are required to select the initial tensile loading to start the test at the unknown threshold value. If a tensile load is selected that would produce a stress intensity factor range below the threshold, then the crack will not grow; however, if the load is high enough, the crack will grow. The applied loading is then held constant during the remainder of the test.

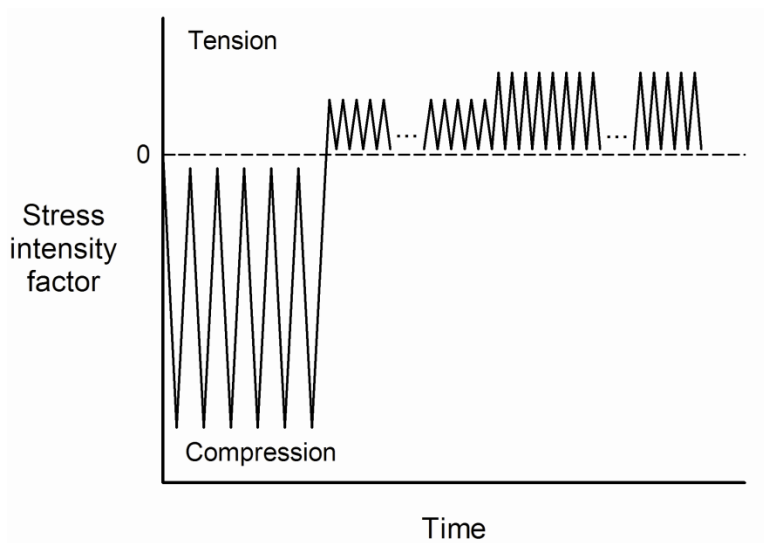

Figure 13. Definition of CPCK Loading

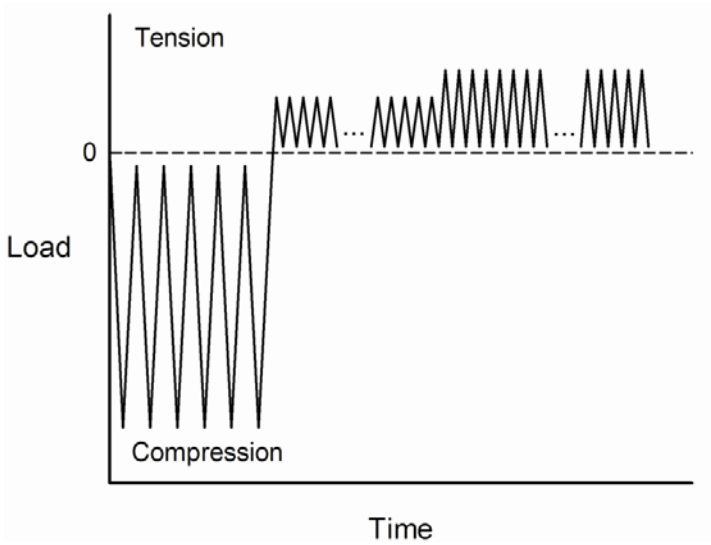

Figure 14. Definition of CPCA Loading

4.1.3.7 CPLR Testing.

The CPLR test procedure, as shown in figure 15, was designed to generate a fatigue crack under CP loading and start the LR procedure (like the current ASTM E-647 standard) at an FCG rate or initiate the stress intensity factor range much lower than allowed in the current standard. After CP loading, the crack is grown under CPCA loading until the crack extension criteria are met (equations 2 and 3). The LR procedure is then initiated, following the same guidelines as described in ASTM E-647. Once the threshold conditions (less than 1E-10 m/cycle) are met, a load-increasing test is conducted. Once the crack starts to grow, the applied loading is then held constant during the remainder of the test.

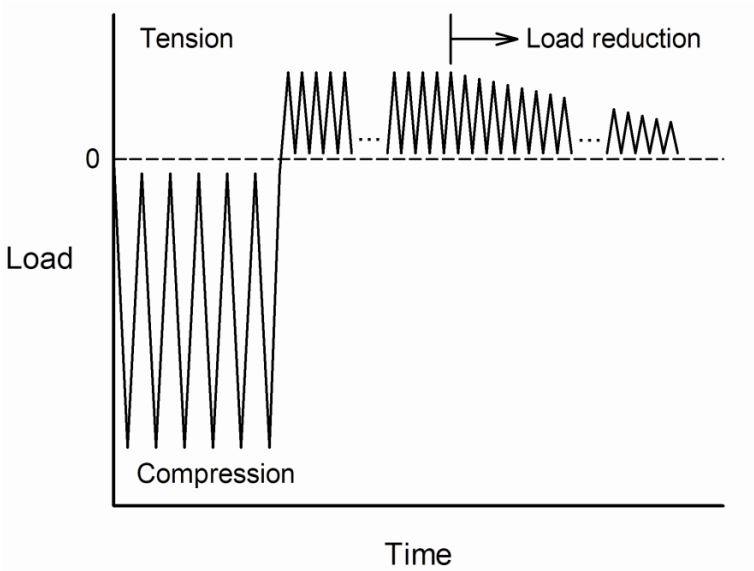

Figure 15. Definition of CPLR Loading

4.2 FATIGUE S-N TESTING.

4.2.1 Aluminum Alloy 7050-T7451.

Fatigue tests were conducted on SEN(B) specimens, as shown in figure 8. The 7050-T7451 aluminum alloy semicircular notches were mechanically polished as part of the process to minimize the residual stresses from machining. A residual stress distribution in an aluminum alloy SEN(B) specimen was determined by Michael Hill (University of California—Davis) using the slitting method. These results are represented by the square symbols in figure 16. The slitting method generated a through-thickness average of residual stresses along the anticipated crack path. The residual stress, σ_{rs}, has been normalized by the yield stress of the material. As expected, very few residual stresses were present in the aluminum alloy specimens.

For the 7050-T7451 alloy, fatigue tests were conducted over a wide range in loading conditions. They were: (1) CA loading at R = 0.1, (2) Mini-Falstaff+, and (3) Mini-TWIST+ (levels 1 and 3). Both of the spectrum load sequences were modifications of the Mini-Falstaff [58 and 59] and Mini-TWIST [60 and 61] European standard spectra, respectively, by adding a mean load to maintain a tension-tension loading sequence, such that the nominal R (minimum to maximum load in the modified spectra) was 0.1. This was necessary because the SEN(B) specimen can only be subjected to tensile loading. Cycles to failure for each test specimen and loading condition were plotted against maximum applied stress, $P_{max}/(WB)$, to develop a fatigue S-N curve.

Fatigue test data from the literature on 7050-T7451 aluminum alloy, open-hole specimens [62] subjected to various CA loading conditions (R = 0.2 and -0.4), are also shown for comparison.

Using large crack data generated in a previous FAA-sponsored program [19] and the effective stress intensity factor range-against-rate (ΔK_{eff}-rate) curve, the life prediction code, FASTRAN [16], was used with small crack theory and an EIFS to calculate the fatigue S-N behavior for both CA and spectrum loading conditions. The EIFS was based on microstructural studies on inclusion particle sizes [63] that caused high-stress concentration open-hole specimens to fail.

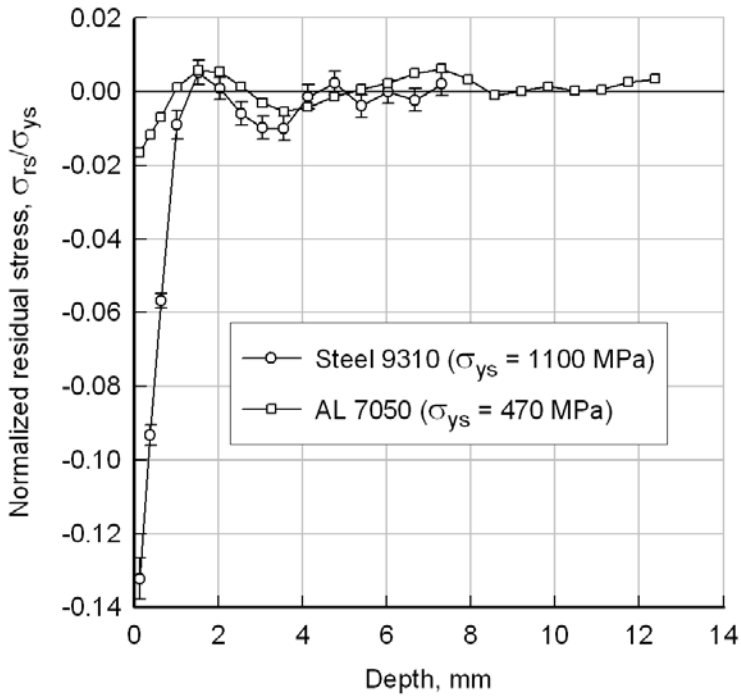

Figure 16. Normalized Residual Stresses in SEN(B) Specimens

4.2.2 9310 Steel.

Fatigue tests were performed on SEN(B) specimens, as shown in figure 8. The SEN(B) specimens had a larger overall length (L) than the one used for the 7050 specimens, but the notch size, width, and thickness were the same. Both specimens had the same elastic stress concentration factor and the same elastic stress distribution across the net section. The 9310 steel specimens and semicircular notches were chemically polished to remove residual stresses induced by machining. However, the electrochemical polishing process resulted in undesirable surface irregularities on some of the steel specimens, mostly away from the notch region. Again, a residual stress distribution in a SEN(B) specimen was determined by Michael Hill at UC, Davis using the slitting method. These results are represented by the circular symbols in figure 16. The residual stress, σ_{rs}, has been normalized by the yield stress of the material. The results for the steel seem fairly typical for a carburized coupon, and the near-surface stresses were about -150 MPa. These compressive residual stresses could have some influence on the fatigue behavior of the SEN(B) specimens.

For the 9310 steel, fatigue tests were conducted under CA loading at R = 0.1. During the fatigue tests, some small cracks were monitored along the bore of the notch with a high-power microscope to generate crack-length-against-cycles data.

Using large crack data generated by these tests and the effective stress intensity factor range-against-rate (ΔK_{eff}-rate) curve, the life prediction code, FASTRAN [16], was again used with small crack theory and an EIFS to calculate the fatigue S-N behavior for CA loading. Because the 9310 steel is a fairly clean alloy, the EIFS value could not be related to any metallurgical

features. In addition, comparisons were also made of crack-length-against-cycles behavior from test measurements (small to large cracks) and FASTRAN analyses.

5. MATERIALS TESTED AND ANALYZED.

Four materials were tested at MSU using the current ASTM LR test procedure and the two newly developed CP threshold testing methods (CPCA and CPLR). Three aluminum and one steel were tested over a wide range in load ratios, R, with FCG rates ranging from threshold to near-fracture. The BFS gage was used to monitor crack growth in the C(T) specimens. Crack opening loads were also measured using both local and remote strain gages. The crack closure model, FASTRAN, was used to correlate the large crack data over the wide range in load ratios and to develop the ΔK_{eff}-rate baseline curves for each material. Fatigue tests were also conducted on two of the materials (7050 aluminum alloy and 9310 steel) and small crack data were generated on the 9310 steel specimens. On most of the materials, small crack theory was used to predict the fatigue behavior of notched specimens from the literature or during this research.

5.1 ALUMINUM ALLOY 2024-T3.

The 2024-T3 aluminum alloy material was obtained from the NASA LaRC as 305 x 914 x 2.3-mm-thin sheets. This material was a special stock of aluminum alloy material that was purchased nearly 60 years ago to characterize the fatigue and fracture behavior. The 2024 alloy is a key material that has been widely used and has dominated the aircraft industry in the past century. Previous FCG tests on this alloy were primarily conducted on M(T) specimens, where 152-mm-wide C(T) specimens were machined from the supplied material blanks. Testing was conducted over a wide range in stress ratios ($0.1 \leq R \leq 0.9$) using the three threshold testing methods.

In addition, a local sideface strain gage was used to measure crack opening loads, especially during the development of threshold conditions. Elber [39] had used a local CTOD gage to measure crack opening loads on the 2024 alloy. It was also found that beveled (or counter-bored) pinholes in the C(T) specimens greatly improved the linearity of the local strain gage reading by preventing out-of-plane bending. These results are compared with the traditional method of using the BFS (or CMOD) gages, which are remote methods.

5.1.1 Large Crack Behavior.

The FCG tests were conducted over a wide range in load ratio conditions ($0.1 \leq R \leq 0.9$) and a constant K_{max} test. Figure 17 shows the test data, which generally ranged from threshold to near-fracture. All specimens were compression precracked before FCG testing. After CPCA loadings, the CPLR tests were conducted from a starting rate of 2 to 3E-9 m/cycle. Once the threshold regime was reached, CA loads were applied to generate the mid-region and near-fracture data. Because the 2024-T3 C(T) specimens have a thickness of 2.3 mm and a width of 152 mm, backface buckling may have occurred when the crack length was large or high loads were used for the high-load ratio tests, such as at $R = 0.9$. Thus, the tests were unable to generate near-fracture data for $R = 0.7$ and 0.9.

The current C(T) data were compared with the previous M(T) specimen data from the literature [29 and 30] and good agreement was found for the R = 0.7 data. The R = 0.1 data showed similar results with the R = 0 data from threshold to the mid-region, but showed faster crack growth near fracture. This was partly due to the slightly higher stress ratio (0.1 instead of 0). CPCA tests were performed on R = 0.9 and 0.1 only. The CPCA tests at R = 0.9 data agreed well with CPLR data, but the CPCA R = 0.1 results showed a slightly higher threshold of 3.2 MPa-m$^{1/2}$, while CPLR produced 3.0 MPa-m$^{1/2}$.

In the previous testing, it had been shown that constant K_{max} test results were affected by crack closure [25-27], just like constant R tests. In this report, a constant K_{max} test was chosen to have a much lower K_{max} value (7.3 MPa-m$^{1/2}$) than the reference test (22 MPa-m$^{1/2}$) from the literature [6]. Each constant K_{max} test produced different load ratio data; the K_{max} test of 22 MPa-m$^{1/2}$ had R from 0.72 to 0.94, whereas the K_{max} test of 7.3 MPa-m$^{1/2}$ had R from 0.1 to 0.8. The R=0.7 and 0.9 tests produced the thresholds of 1.8 and 1.45 MPa-m$^{1/2}$, whereas constant K_{max} tests (22 and 7.3 MPa-m$^{1/2}$) showed thresholds of 1.22 and 1.63 MPa-m$^{1/2}$, respectively. As expected, lower threshold values were obtained from the highest load ratio test.

In figure 17, the solid lines with open circles show the small and large crack data ΔK_{eff}-rate curve for the 2024-T3 alloy [64]. The lower portion of the curve that does not agree with the high-R large crack threshold data shows a fit for small crack data [22]. The upper portion agreed well with the high-R data.

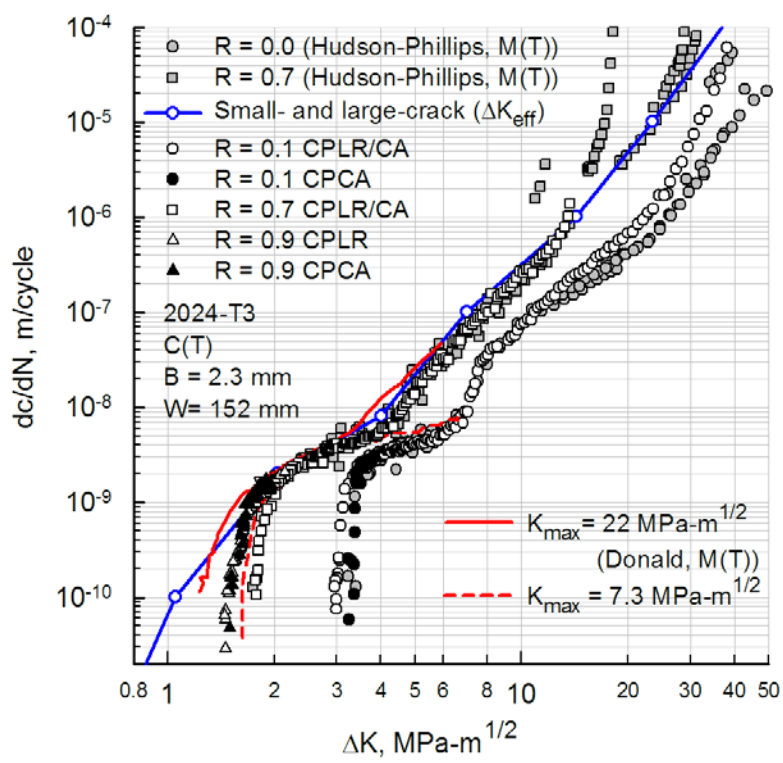

Figure 17. The FCG-Rate Data on 2024-T3 Aluminum Alloy

5.1.2 Crack Closure Behavior.

The crack closure concept has been a major development in the treatment of FCG. As mentioned, Elber [39] used a local CTOD gage to measure the load against CTOD during cyclic loading. From an analysis of the load displacement record, he was able to measure the crack opening load, as described in appendix A. However, during the past 40 years, remote methods, such as CMOD or BFS gages, have been used to measure crack opening loads because of convenience because these methods were also being used to measure crack extension. However, the general opinion based on these measurements was that the crack closure concept was not appropriate, so other methods were developed, such as Adjusted Compliance Ratio method [65].

During the past few years, researchers at MSU have returned to local measurements, as shown in figure 18, and have discovered high-R closure [24-27]. More importantly, these local measurements have been able to collapse low-R, high-R and K_{max} test data onto nearly unique ΔK_{eff}-rate curves in the threshold and near-threshold regimes for a variety of materials. The local measurements of crack opening loads were fairly close to those measured with remote methods for low-R, but under high-R conditions, the remote methods were found to be inadequate. However, local methods exhibited closure under high-R conditions, for which previous research had concluded that these high-R tests were crack closure-free. These local measurements have renewed the development of the crack closure concept.

To measure load strain records near the crack tip, strain gages were mounted close to the crack path for the specimen tested for all test conditions (R = 0.1, 0.7, 0.9, and constant K_{max} test). The locations of the strain gages were chosen to be slightly off the anticipated crack path by approximately the crack-starter notch height (≈2 mm) and approximately 5 mm away from the crack tip after CP (figure 18). A number of strain gages were mounted along the anticipated crack path to record load strain records as the crack approached these gages. The optimum signals were obtained when the crack tip was about 2 to 3 mm away from the strain gage during threshold testing. Approximately 20 load strain records were recorded when the target FCG rates were achieved. During measurements, the frequency of cyclic loadings was reduced to 0.5 Hz to minimize external noise. The BFS and crack-monitoring software recorded various compliance-offset values using Elber's reduced-strain approach [28]. In general, the results from the BFS showed the tail swing associated with crack closure and the compliance-offset values from 1% to 16%. The ASTM E-647 standard [3] recommends the 2% (OP2) value.

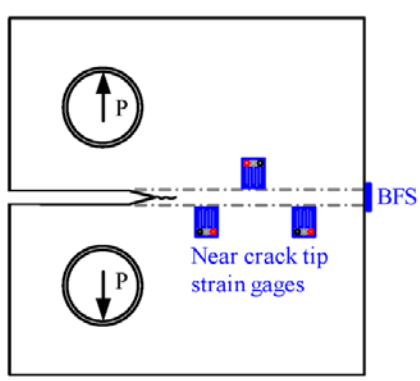

Figure 18. The C(T) Specimen With Local and Remote BFS Gages

During FCG testing, crack lengths were monitored using compliance data from a BFS gage. Compliance data, which is the inverse of stiffness, from the closure-free portion of the load cycle is used to determine crack length, enabling the tests to be automated and computer controlled. Load remote strain data can also be used to measure fatigue crack closure events. However, as previously mentioned, caution should be exercised in using these crack-opening loads.

The local strain gage was also used to determine load-against-local-strain records at specified intervals based on the placement of the local gages. A typical load-against-local strain record is presented in figure 19(a) for R = 0.1. For CA loadings, the compliance is constant at high loads (open crack), which appears as a linear section in the upper-right portion of the figure. As the load decreases, crack surfaces contact and produce a change in compliance. In cases where a large portion of the crack surface closes during unloading, this compliance change is very dramatic. When only a small portion of the crack closes very near the crack tip, this change in slope may be difficult or impossible to distinguish on a load-against-strain plot. The reduced displacement (or strain) method was developed to improve detection of these subtle compliance changes. The reduced strain, $\Delta\varepsilon$, is the deviation from closure-free compliance behavior, as shown in figure 19(b). Crack opening loads are more easily detected from load-against-reduced-strain plots. Closure-free behavior on these plots becomes a vertical line, making compliance deviations easier to detect. Using the reduced-strain method, the deviation from the fitted line due to closure is clearly seen; significant deviation at low loads (P/P_{max}< 0.5) is observed in figure 19(b). Fitting lines through closure-free data (P/P_{max} >0.5) allows closure to be defined as the load corresponding to the intersection of the fitted lines. However, this method does not provide information about the location of crack face contact since this method relies on changes in compliance to determine closure (or crack opening) levels. Note that the crack opening load ratio, P_o/P_{max} = 0.5, at R = 0.1 conditions, is very close to what Elber measured on the same alloy at R = 0 in 1968.

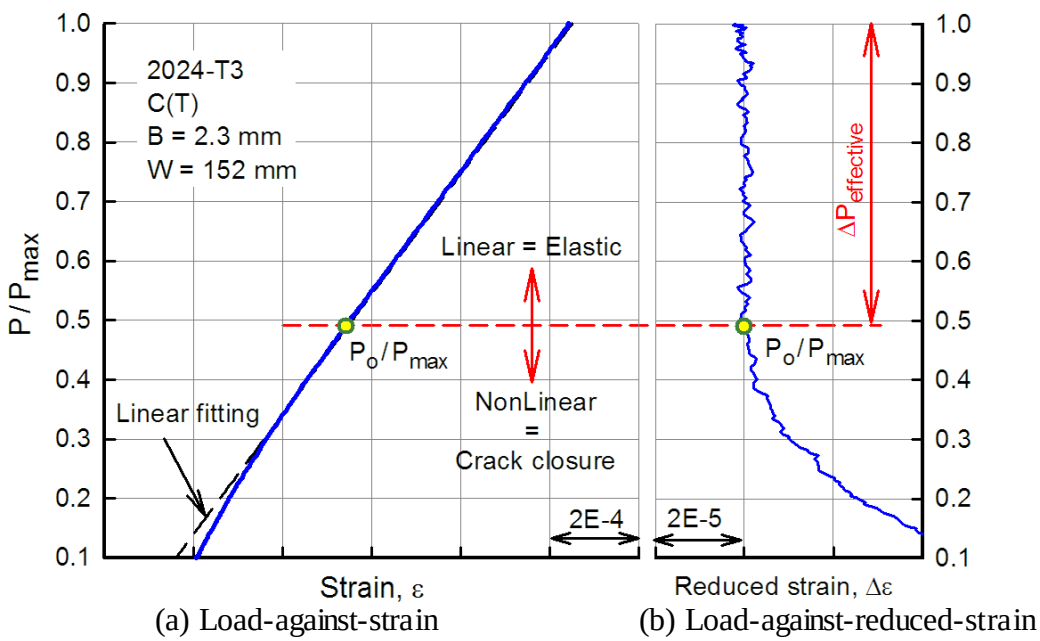

Figure 19. Load-Against-Local-Strain and Reduced-Strain Record on 2024-T3 Aluminim Alloy at R = 0.1

A comparison is shown in figure 20 between local and remote BFS gage readings on a C(T) specimen made of the 2024-T3 alloy for an FCG rate of 2.2E-09 m/cycle. This figure shows the load-reduced strain records measured on a test at R = 0.1. The results from the BFS show the tail swing associated with crack closure and the compliance offset values of 1% offset compliance (OP1) and 2% offset compliance (OP2). The compliance offset values gave progressively lower values of the crack opening load ratio for larger offset values. The circular symbol shows the crack opening load ratio determined by inspection (deviation from upper linear portion of the load-reduced-strain record) from the local gage. The near-crack tip gage showed a similar load-reduced-strain record to the BFS gage, but showed a slightly larger tail swing and indicated that the crack opening load would be about 5% higher than the 1% offset value. Based on the difference between 1% and 2% offset opening values (0.465 and 0.425) and linear extrapolation to 0% offset, the opening load would be about 0.5, which agreed very well with the crack opening load determined from the local reading. Also, by comparing remote and local gage readings, it indicated that the measurement location was not a problem as long as the load strain records were measured ahead of crack tip. The curvature below the crack opening load showed noticeable differences between local and remote gage readings. Local gage readings showed an aggressive change below the opening load, while the BFS gage showed a gradual change. Thus, local gages enhance the fidelity to determine crack opening loads.

The load strain records at R = 0.1 loading were measured during a CPCA threshold test and the corresponding load-against-reduced-strain results are shown in figure 21. Because of better sensitivity, crack opening loads from local gages were quite easy to determine. Crack opening loads from the local gages were determined by inspection, whereas OP1 values (represented by the square symbols) came from the BFS gage readings made with the crack monitoring system [66]. Consistently, the local gages showed significantly higher crack opening loads than the remote gages, but both records showed the same trend, in that the crack opening loads were rising as the FCG rate approached threshold conditions.

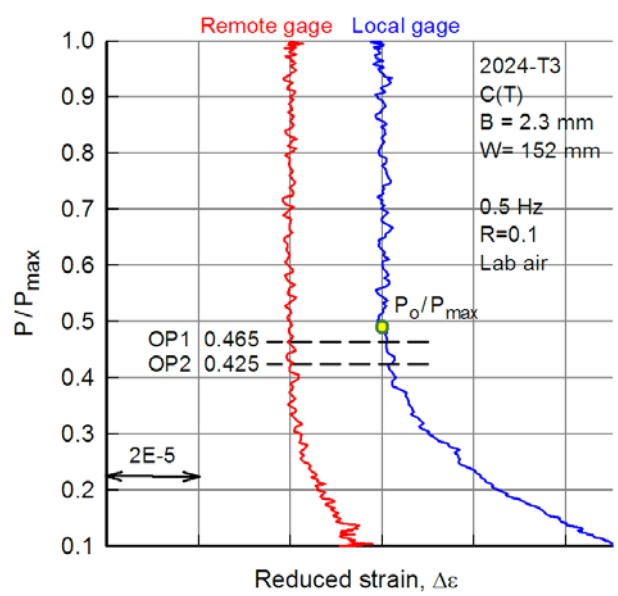

Figure 20. Comparison of Remote and Local Strain Gage Determination of Crack Opening Loads for R = 0.1

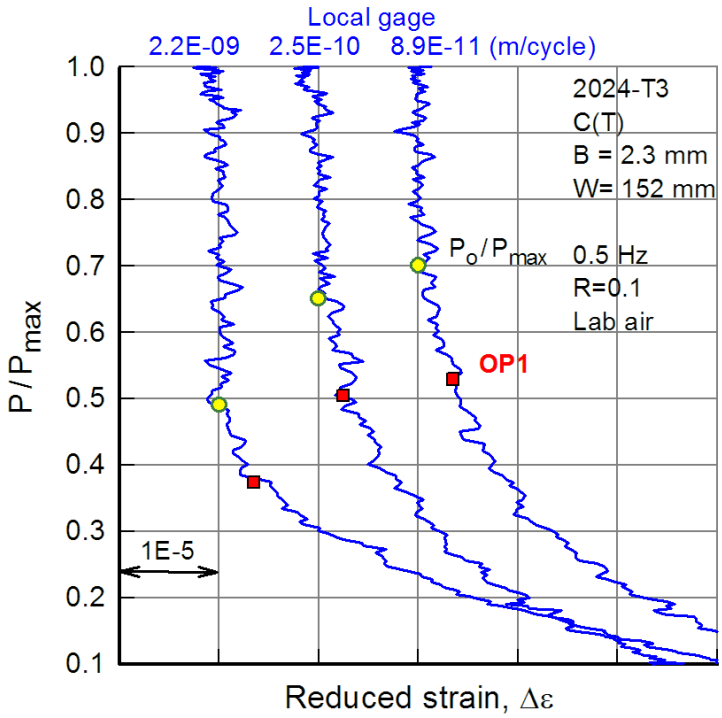

Figure 21. Determination of Crack Opening Loads for a CPLA Threshold Test at R = 0.1

Figure 22 shows load-against-reduced-strain records for a CPLR test at R = 0.7. Although the compliance changes in the load-reduced strain records were not significant, the tail swing due to crack closure was clearly shown. Again, the crack opening loads were increasing as the ΔK values were reduced and the threshold conditions were approached. A comparison of remote and local strain gage records is shown in figure 23, which clearly demonstrates why the remote gage is inadequate in determining crack opening loads for high-stress ratio conditions. Figure 24 shows some load-against-reduced strain records for a K_{max} test, which again shows evidence of high-R closure.

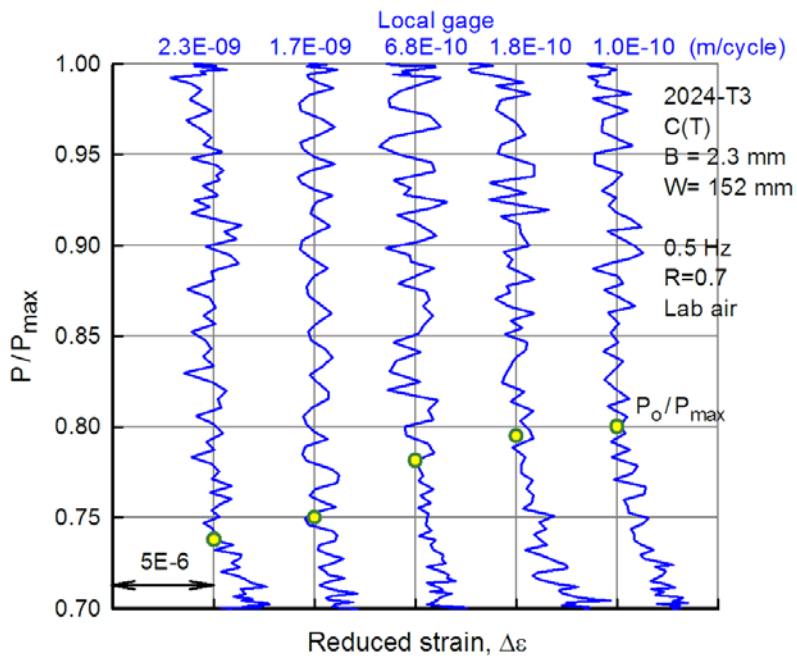

Figure 22. Determination of Crack Opening Loads for a CPLR Threshold Test at R = 0.7

Figure 25 shows the crack opening load ratios measured with the local strain gages over a wide range in R-values and the K_{max} test. The differences between the dashed lines and the measured values indicate the amount of crack closure for each R. At R = 0.1, the tests were either CPCA or CPLR and the results agreed very well. Thus, load history effects due to LR in the CPLR test are not likely due to the very low initial ΔK_i values used, especially at high-R. However, what has caused the rise in crack closure behavior in the near-threshold regime is unclear.

In the literature, plasticity effects have been dismissed because the plastic zone sizes are very small near-threshold conditions, but crack surface displacements are also very small. Plasticity-induced crack closure (PICC) is due to interference between the residual plastic deformations and crack surface displacements. Thus, in the threshold regime, PICC is still a very dominant shielding mechanism at all R values. The measurement of crack opening loads at the free surface may measure plane stress behavior instead of interior plane strain or average through-the-thickness behavior. It is still unclear how three-dimensional crack opening loads are used in a two-dimensional analysis [67]. Crack opening loads at the free surface should affect the near-crack front strain ranges in the interior, but, at the small ΔK values, plane strain behavior should be dominant and plane stress behavior would then be over a very small zone.

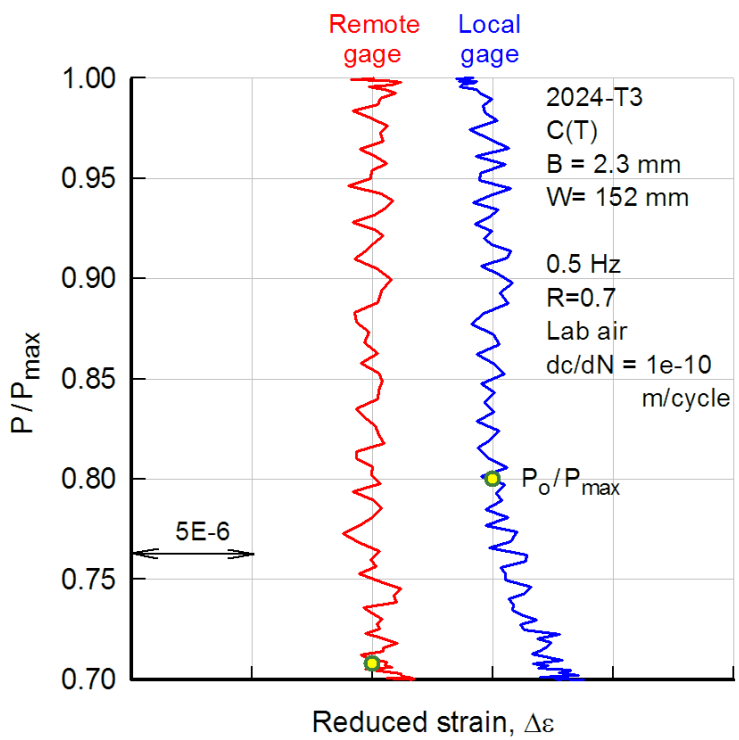

Figure 23. Comparison of Remote and Local Strain Gage Determination of Crack Opening Loads for R = 0.7

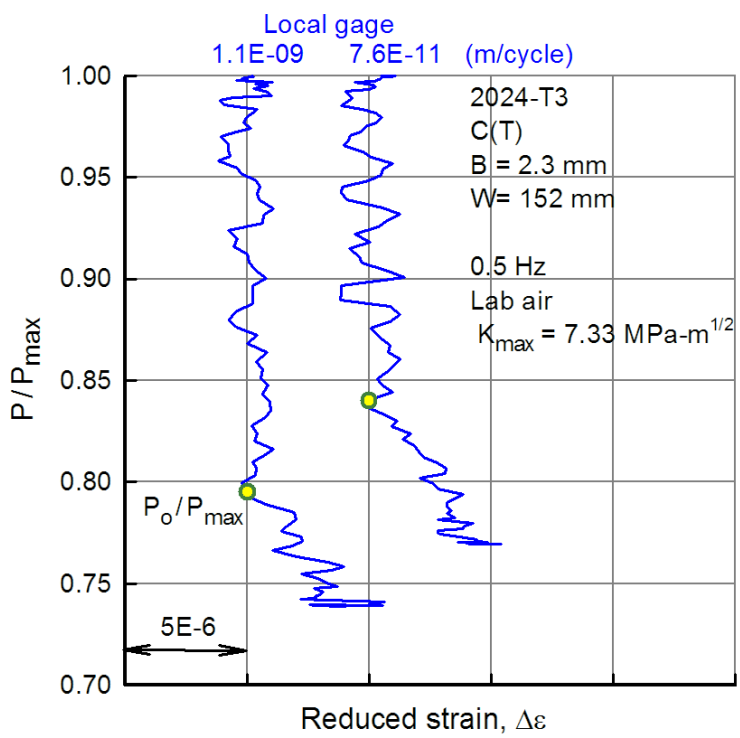

Figure 24. Determination of Crack Opening Loads for a K_{max} Threshold Test

PICC models [68] predict that, above $R \geq 0.7$, the cracks should be fully open under plane stress conditions. However, for high-R conditions, the crack opening load from PICC modeling is at the minimum load. Thus, a small amount of debris- or roughness-induced closure, in addition to that caused by PICC, could cause high-R closure. As shown in figure 25, if PICC did not happen at high-R, then the small amount of debris- or roughness-induced crack closure would not have caused high-R closure.

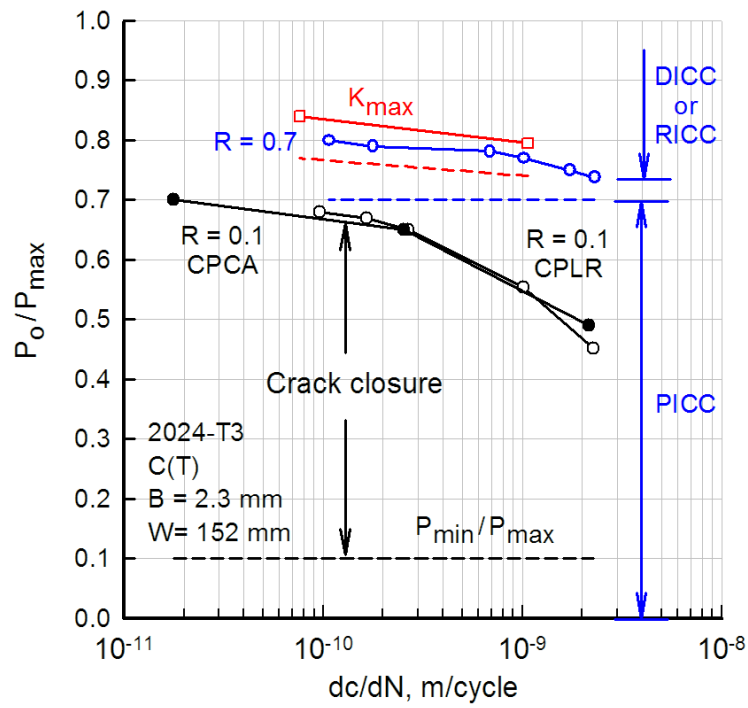

Figure 25. Crack Opening Load Ratios for Low R, High R, and K_{max} Test Results in Threshold Regime

Based on the crack opening loads determined from local gages, crack closure corrections were performed on the R = 0.1 and 0.7 test data and the low constant K_{max} test data. These results are shown in figure 26. All of the crack closure corrected (ΔK_{eff}) data have now collapsed together into a fairly tight band and the results are approaching a $(\Delta K_{eff})_{th}$ value at a threshold of approximately 1 to 1.15 MPa-m$^{1/2}$. These ΔK_{eff} results consistently fell lower than the high constant K_{max} test (22 MPa-m$^{1/2}$). At the ASTM-defined threshold (10^{-10} m/cycle), the $(\Delta K_{eff})_{th}$ ranged from 1.02 to 1.17 MPa-m$^{1/2}$, whereas ΔK_{th} from the high constant K_{max} test was 1.22 MPa-m$^{1/2}$. These results suggest that the ΔK_{eff}-against-rate relation may be a unique function over a wide range of R in the threshold regime of 2024-T3 if more appropriate crack opening load values were measured. It seems that a high constant K_{max} test may be able to generate ΔK_{eff} baseline data for near-threshold conditions. The 2024-T3 aluminum alloy had a fairly flat crack surface. Thus, PICC should dominate with some additional fretting debris-induced crack closure and very minor crack surface roughness-induced crack closure.

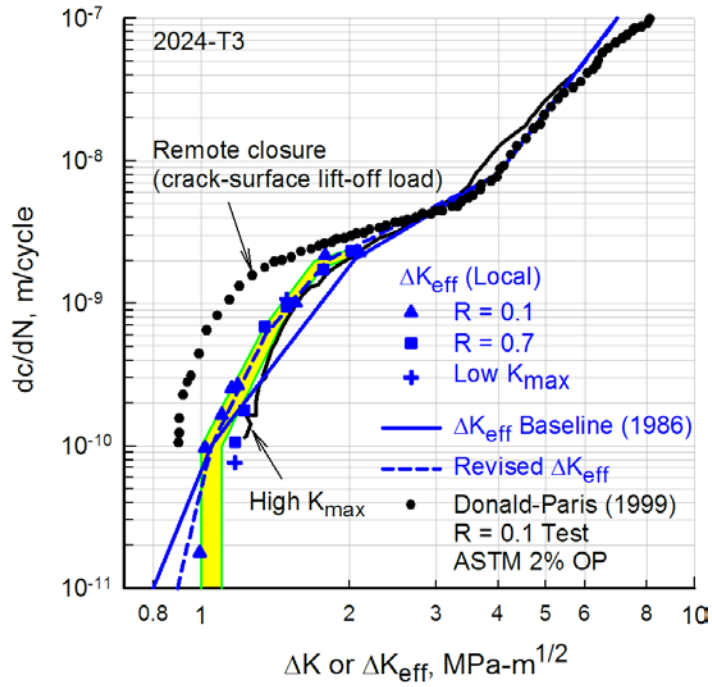

Figure 26. Effective Stress Intensity Factor Range-Against-Rates for 2024-T3 Aluminum Alloy in the Near-Threshold Regime

The solid lines in figure 26 show the ΔK_{eff}-rate baseline relation established in 1986 based on small crack test data in the low-rate regime [22 and 64]. The dashed lines show a slight modification to fit the large crack ΔK_{eff} experimental results. Thus, small and large crack test data have now agreed on a ΔK_{eff} basis. For comparison, results from Donald and Paris [6] on an R = 0.1 LR test for large cracks are shown as solid, circular symbols. They used the ASTM 2% offset method to calculate the ΔK_{eff} values and the method generated data at lower ΔK_{eff} values than local measurements. It is suspected that the LR test method causes remote crack closure along the crack surfaces [69] and that the 2% offset method measures the crack surface liftoff load, which is higher than the traditional crack opening load. Thus, the LR test and the 2% offset method overcorrected the ΔK-rate data in the near-threshold regime.

5.1.3 Crack Closure Analysis.

Test data from Hudson [29], Phillips [30], and Dubensky [31] correlated very well over nine orders of magnitude in rates [70]. In the mid-region, a constraint loss regime (plane-strain to plane-stress behavior) is modeled in the life prediction code. The solid curve shows the original ΔK_{eff}-rate relation and the solid curve with symbols shows the revised ΔK_{eff}-rate relation for the 2024-T3 alloy in the small and large crack regimes.

Figure 27 shows ΔK_{eff}-rate data on 2024-T3 alloy determined from the FASTRAN crack closure model [16], which is based only on PICC. The large crack data were obtained by Hudson [29], Phillips [30], and Dubensky [31] on M(T) specimens over a wide range in stress ratios and stress levels. In 1969, Hudson produced FCG-rate data for a 2024-T3 aluminum alloy sheet over a

wide range of stress ratios (R = -1 to 0.8) and stress intensity factor ranges. Later, Phillips generated FCG data in the near-threshold regime for the same alloy, and Dubensky conducted tests at extremely high remote stress levels (0.6 to 1.0 times the yield stress of the material). These tests produced FCG-rate data over nine orders of magnitude in rates. The solid curve for rates less than 1E-9 m/cycle was obtained from small crack data [16 and 22]. The curve with symbols in figure 26 shows the ΔK_{eff}-rate curve as determined from recent local crack closure measurements made on large cracks [71], which surprisingly agreed fairly well with the earlier results on small cracks.

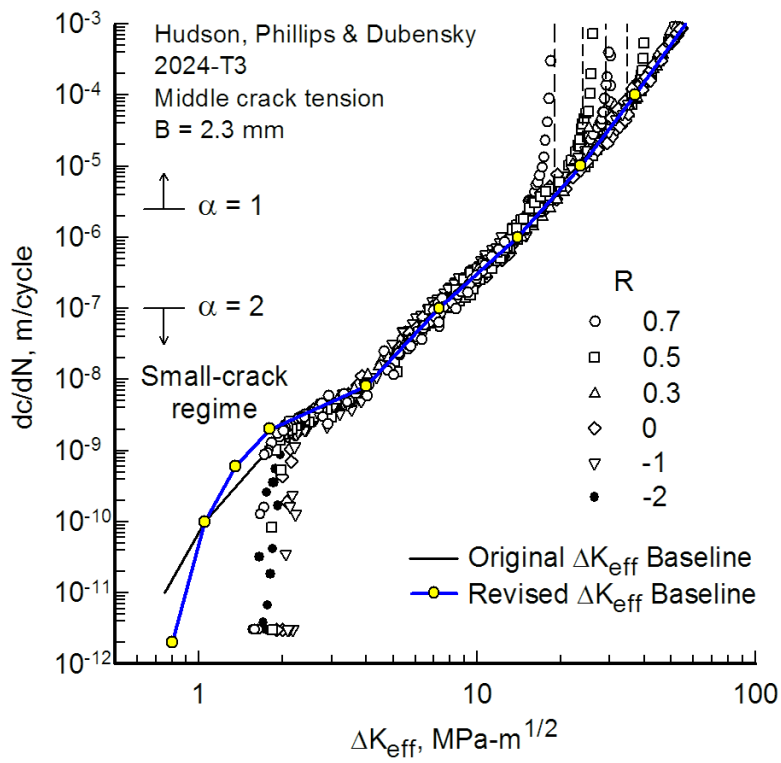

Figure 27. Effective Stress Intensity Factor Range-Against-Rates for 2024-T3 Aluminum Alloy

In the midrate regime, these results show the constraint loss regime (plane-strain to plane-stress behavior [72]) and the constraint factor varies from α = 2 to 1. In the fracture region, the vertical lines show where the respective specimens were predicted to go to failure.

The relationship between ΔK, or any other parameter like ΔK_{eff}, plotted against FCG rate, does not always fit the simple power or sigmoidal relations that have been proposed. Miller and Gallagher [73] found that more accurate life predictions could be made if a table lookup procedure was used. Many materials have sharp transitions in rate behavior that are well-suited to the table lookup method. A number of life prediction codes, such as NASGRO [1], AFGROW [2], and FASTRAN [16], have adopted this procedure.

$$dc/dN = C_{1i}\,(\Delta K_{eff})^{C_{2i}}\,[1 - (\Delta K_o/\Delta K_{eff})^p]/[1 - (K_{max}/C_5)^q], \qquad (6)$$

In general, the multilinear table lookup FCG-rate relation used in FASTRAN is where dc/dN is the fatigue crack growth rate, C_{1i} and C_{2i} are the coefficient and power for each linear segment, ΔK_{eff} is the effective stress intensity factor, ΔK_o is the effective threshold, $K_{\max}$ is the maximum stress intensity factor, C_5 is the elastic cyclic fracture toughness ($C_5 = K_{\mathrm{I}e}$, which is generally a function of crack length, specimen width, and specimen type), and p and q are constants selected to best fit test data in either the threshold or fracture regimes. Whenever the applied $K_{\max}$ value reached or exceeded C_5 (or $K_{\mathrm{I}e}$), then the specimen or component would fail. In the early 1970s, Newman [74 and 75] proposed the two-parameter fracture criterion (TPFC) to correlate fracture data and to predict failure loads on cracked metallic materials. The TPFC has been able to predict $K_{\mathrm{I}e}$ for different crack lengths, component sizes, and loading using the two fracture parameters, K_F and m. The fracture parameter m is zero for brittle materials, like the plane strain fracture toughness, K_{Ic}, and $m = 1$ for very ductile materials. For $m = 1$ and very large K_f values, the TPFC reduces to a plastic collapse failure criterion. Likewise, in the threshold regime, if the ΔK_{eff} is equal to ΔK_o, then the FCG rate goes to zero and the value of p controls the shape of the rate curve in the near-threshold regime.

For the 2024-T3 alloy, the threshold and fracture terms in equation 6 were not used. It had been found that the multilinear power relation fit the test data very well only in terms of ΔK_{eff} and rate fit. The threshold behavior for small cracks is modeled with the lower section of the table lookup values. The fracture behavior is predicted from the TPFC using K_f and m values determined for fracture tests [75] (see table 7).

Table 7. Effective Stress Intensity Factor Range-Against-Rate Relation for 2024-T3 Aluminum Alloy (B = 2.3 mm)

ΔK_{eff}, MPa√m	dc/dN, m/cycle
0.80	2.0e-12
1.05	1.0e-10
1.35	6.0e-10
1.80	2.0e-9
4.00	8.0e-9
7.30	1.0e-7
14.0	1.0e-6
23.5	1.0e-5
37.0	1.0e-4
85.0	0.01
$\alpha = 2$	1.0e-07
$\alpha = 1$	2.5e-06
$\Delta K_o = 0$ MPa√m	$p = 1$
$K_f = 267$ MPa√m	$m = 1$

Prior to Elber's discovery, Tomkins [76] was using the Bilby et al. dislocation model [77] to develop a cyclic CTOD parameter for FCG. It was thought that the cyclic CTOD was a more fundamental parameter to characterize crack tip damage than the stress intensity factor. After Rice [78] developed the J-integral, Dowling and Begley [79], among others, began to explore the use of the ΔJ_{eff} parameter for FCG, especially to characterize the growth of small cracks. Newman [80] also used a cyclic plastic zone corrected stress intensity factor range, similar to ΔJ_{eff}, to correlate and to predict FCG under low-cycle fatigue (LCF) conditions. In addition, Newman [81] compared the cyclic CTOD and ΔK_{eff} concepts for characterizing crack tip damage and found close agreement. Similarly, Ogura et al. [82] proposed using the local cyclic hysteresis energy (W_{eff}).

Recently, an application of the FASTRAN crack closure model based on the Dugdale strip-yield model [57] was again used to evaluate the effective stress intensity factor range (ΔK_{eff}) for characterizing crack tip damage. Figure 28 shows calculated CTODs for a crack in an infinite plate under remote uniform applied stress at R = 0 loading (the CTOD values are proportional to the cyclic plastic strains in the crack tip region).

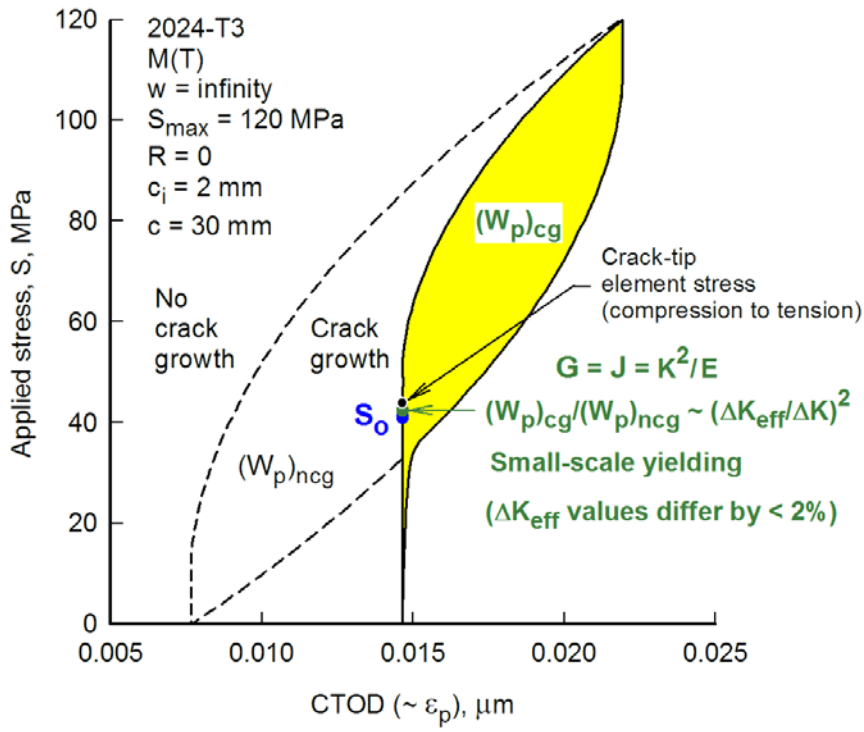

Figure 28. Cyclic CTODs With and Without Fatigue Crack Closure

The initial crack length was 2 mm and the crack was grown in the model until the length had reached 30 mm. Also, plasticity-induced crack closure behavior had developed and stabilized (constant crack opening stress, S_o). The solid curves show the loading and unloading records during one cycle of loading. The calculated crack opening stress is shown by the lower solid symbol along the loading trace. The smaller solid (upper) symbol shows the applied stress level when the crack tip element went from compression to tensile stress, and the beginning of element yielding. The enclosed area is the cyclic hysteresis energy for crack growth, $(W_p)_{cg}$. A second simulation was then made with an initial crack length of 30 mm and applying the same cyclic stress. The dashed curves show the loading and unloading traces with no crack growth, but with plastic yielding at the crack tip. Here, the cyclic hysteresis energy with no crack growth, $(W_p)_{ncg}$, is the area traced by the dashed curves. For small-scale yielding, the strain energy release rate, G, and the J-integral, are equal to K^2/E. Assuming that the ratio of the cyclic hysteresis energies is proportional to $(\Delta K_{\text{eff}}/\Delta K)^2$, the middle circular symbol shows the value of crack opening stress to satisfy the energy ratio. The ΔK_{eff} values calculated from the model using the contact stresses and the hysteresis energies were within 2%. The current method of calculating crack opening stress levels from contact stresses correctly partitions the hysteresis energies. Thus, the ΔK_{eff} crack tip damage parameter is equivalent to using cyclic CTOD, hysteresis energies, or a combination of both.

5.1.4 Small Crack Behavior.

In the 1980s, small crack data on the 2024-T3 alloy had been determined from NASA [64] and AGARD [5 and 22] studies over a wide range of loading conditions. These data will not be

repeated here. Figure 29 shows only a comparison between the more recent determination of the effective stress intensity factor range relation, especially in the low-rate regime, and the previous results.

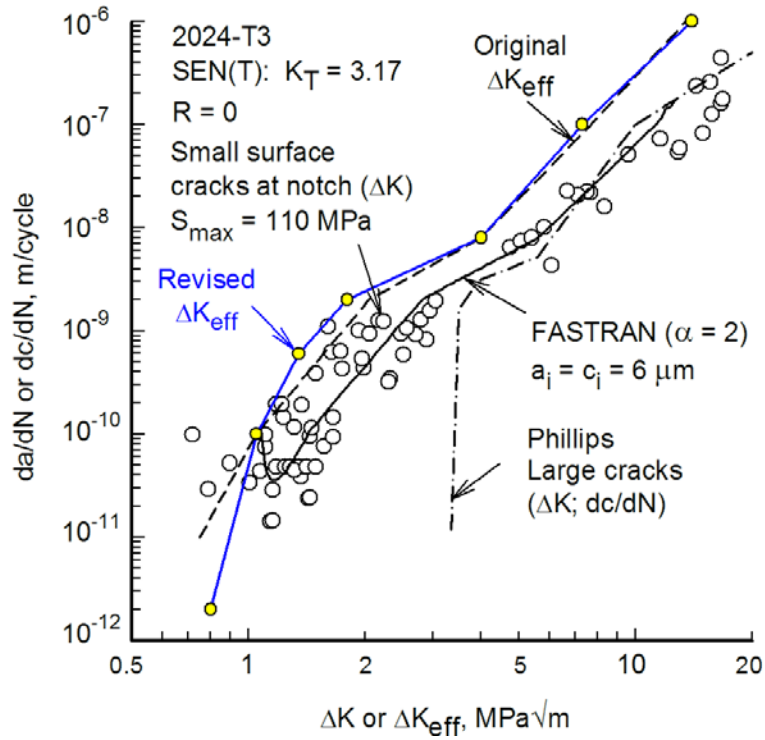

Figure 29. Small Crack Data and the Effective Stress Intensity Factor Range-Against-Rate Relation for 2024-T3 Aluminum Alloy

Figure 29 shows a comparison of small crack data on SEN(T) specimens [22 and 64] and large crack data on M(T) specimens [30] made of the 2024-T3 alloy. The small crack data (*da*/*dN*) shown by the symbols are only a small part of the overall database on this alloy. These results at R = 0 were taken from one laboratory and at an applied stress level of 110 MPa. This alloy showed a very large difference between the large crack threshold (about 3 MPa√m) and small crack growth behavior. Small cracks grew at ΔK values as low as 0.75 MPa√m. However, for ΔK values greater than 3 MPa√m, the small and large crack data agreed quite well. The solid curve represents the predicted rates from the FASTRAN closure model using the original baseline ΔK_{eff}-rate curve (dashed lines). The initial defect was selected as a 6-μm radius surface crack located at the center of the notch. For the R = 0 condition, the small crack effect (initial drop in rates at a ΔK value of about 1 MPa√m) is quite small. The crack opening stresses from the model had stabilized after a small amount of crack growth (as shown by the parallel lines). The solid lines with symbols show the revised ΔK_{eff}-rate baseline curve based on the local crack opening load measurements. This revised baseline curve is used with small crack theory to make fatigue calculations on a few examples to show that fatigue is crack propagation on the aluminum alloy.

5.1.5 Fatigue Behavior.

To make fatigue calculations on the 2024 alloy, the ΔK_{eff}-rate curve must be established and some information on the inclusion particle sizes that initiate cracks is needed. Laz and Hillberry [83] conducted an extensive study on the inclusion particle distributions on the 2024-T3 alloy. Inclusion particle diameters ranged from about 3 to 30 μm in the material microstructure. However, it is clear that the volume of material subjected to a particular stress level has an impact on the mean behavior of fatigue behavior [84 and 85]. To show how FCG can be used to predict or calculate fatigue S-N behavior, examples are presented on coupons with low- and high-stress concentration factors under either CA or spectrum loading.

5.1.5.1 The CA Loading.

Marines et al. [86] conducted a significant number of fatigue tests on dog bone (K_T = 1) specimens (B = 4 mm) made of the 2024-T3 aluminum alloy and tested at an R ratio of 0.1. The test frequency ranged from 10 to 30 Hz. These data are shown in figure 30 and have been partitioned into two groups (modes A and B). These two modes were suspected to have been caused by two competing crack initiation mechanisms. Mode A was an initiation from fractured inclusions and mode B was from persistent slip bands. For some reason, about 20 specimens were tested at each stress level of 240, 260, 280, and 300 MPa, respectively, but only five or fewer below 240 MPa and only three or fewer above 320 MPa. A large dispersion of lifetimes was observed from 240 to 300 MPa, but less at lower and higher applied stress levels. These results prompt the question as to what would have happened if 20 or more specimens were tested at each stress level below 240 MPa.

Using the revised ΔK_{eff}-rate curve in figure 29 and the assumed initial discontinuity sizes of 10 and 30 μm radius external surface cracks in the dog bone specimens, calculations of fatigue lives have been made from LCF to high-cycle fatigue (HCF). These results are shown as the solid curves in figure 30. The 30-μm flaw fit the lower-bound lives quite well, while the 10-μm flaw fit only part of the upperbound lives, especially at the higher applied stress levels. In previous fatigue analyses of the 2024 alloy, an effective stress intensity factor threshold was used to predict an infinite life. The horizontal, dashed lines at $\Delta K_{\text{eff}})_{th}$ = 0.9 MPa√m show the stress level that would not propagate a crack from the inclusion particle of the respective sizes; these lines bound the large scatter region quite well. The question is whether the ΔK_{eff}-rate curve for the aluminum alloy in the very low rate regime has a finite, but very steep, slope approaching threshold conditions. Using a linear extrapolation of the ΔK_{eff}-rate curve into the ultralow rate regime (rates less than 1.0e-10 m/cycle) would allow fatigue predictions to the very high cycle fatigue (VHCF) regime.

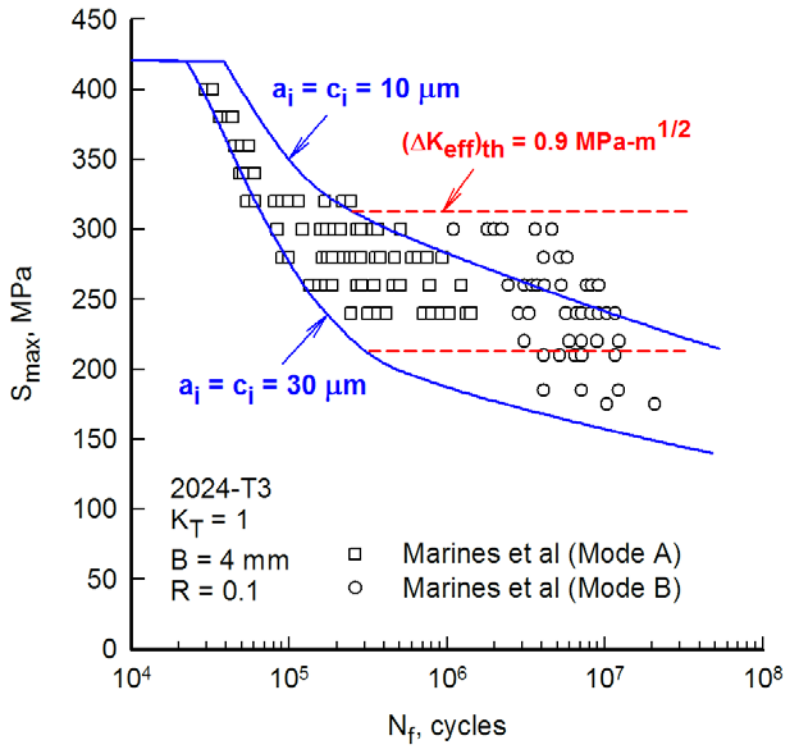

Figure 30. Measured and Calculated Fatigue S-N Behavior for 2024-T3 Aluminum Alloy at $R = 0.1$ on $K_t = 1$ Specimens

Figure 31 shows S-N data from the National Advisory Committee on Aviation TN-3631 [87] on the 2024-T3 alloy for open-hole specimens with two-hole diameters. The symbols show the test data on specimens that had been electropolished. The specimens were 51-mm wide and had hole diameter-to-width (D/W) ratios of 0.0625 and 0.125. The fatigue test data extend from extremely high applied stress levels (above the yield stress of the material) producing LCF conditions to the VHCF region (~10^8 cycles). Note that the aluminum alloy does not have a well-defined endurance limit, which may also suggest that the ΔK_{eff}-rate curve has a steep slope approaching threshold conditions in the ultralow rate regime.

FASTRAN was used to analyze the older fatigue data on the $K_t = 3$ specimens. In the analysis, a semicircular surface crack located along the hole bore was assumed to cause fatigue failure of the specimens. The radius of the surface crack was varied until a best fit of the data was found. A 6-µm (0.00024 in.) radius surface flaw was found to fit the mean of the test data very well. However, in the range of applied stress levels from 150 to 250 MPa, the calculated lives fell somewhat short of the test data (of about a factor of 2 or less). The reason for this behavior is not known, but it has been observed in other comparisons made on the 2024-T3 alloy. The upper and lower dashed curves show the effects of flaw size on fatigue lives and bound most of the test data quite well. From previous studies, these flaw sizes are related directly to inclusion particle clusters size distributions in the 2024 alloy for high K_t configurations.

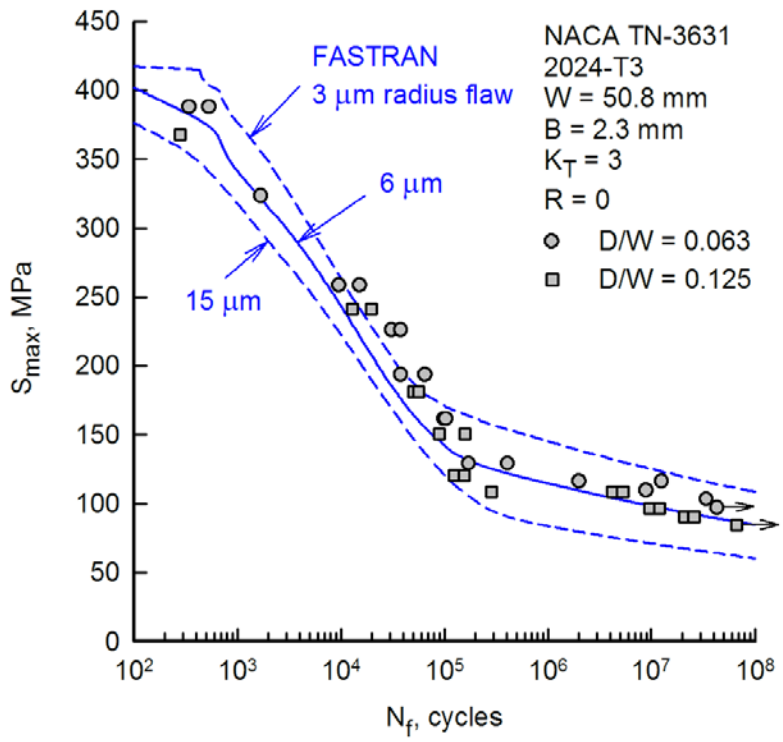

Figure 31. Fatigue Data on Circular Hole Specimens Made of 2024-T3 Aluminum Alloy Under R = 0 Loading

5.1.5.2 Spectrum Loading.

The AGARD Structures and Materials Panel conducted a number of studies in the mid- to late-1980s on small crack behavior on a wide variety of materials. One of the first materials selected was the 2024-T3 aluminum alloy. These studies led to two reports, AGARD R-732 [22] and *R*-767 [21]. Fatigue tests conducted by various laboratories [21 and 22] produced fatigue S-N test data on SEN(T) specimens under a wide variety of spectrum loading conditions (Gaussian—an R ~ -1 random spectrum [88]; FALSTAFF—a fighter aircraft spectrum [58], as shown in figure 32; TWIST—a transport aircraft spectrum [60]; and an original equipment manufacturer wing spectrum). Again, using the 6-μm initial surface flaw (a_i/c_i = 1) at the semicircular notch, the mean behavior could be predicted very accurately, as shown in figure 33; and the predicted results were also found to be independent of the spectrum loading sequence [85 and 89].

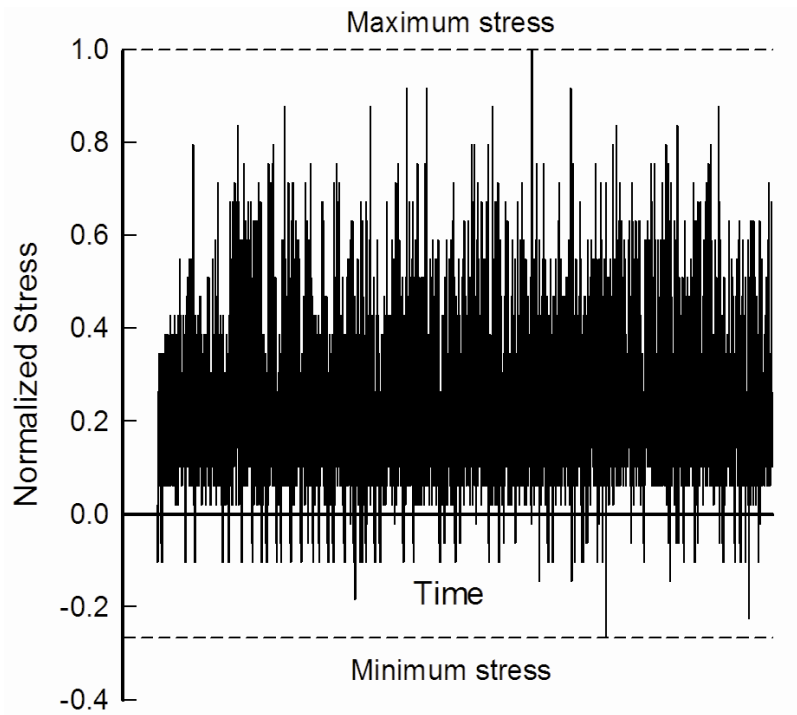

Figure 32. Part of the FALSTAFF Wing Spectrum [58]

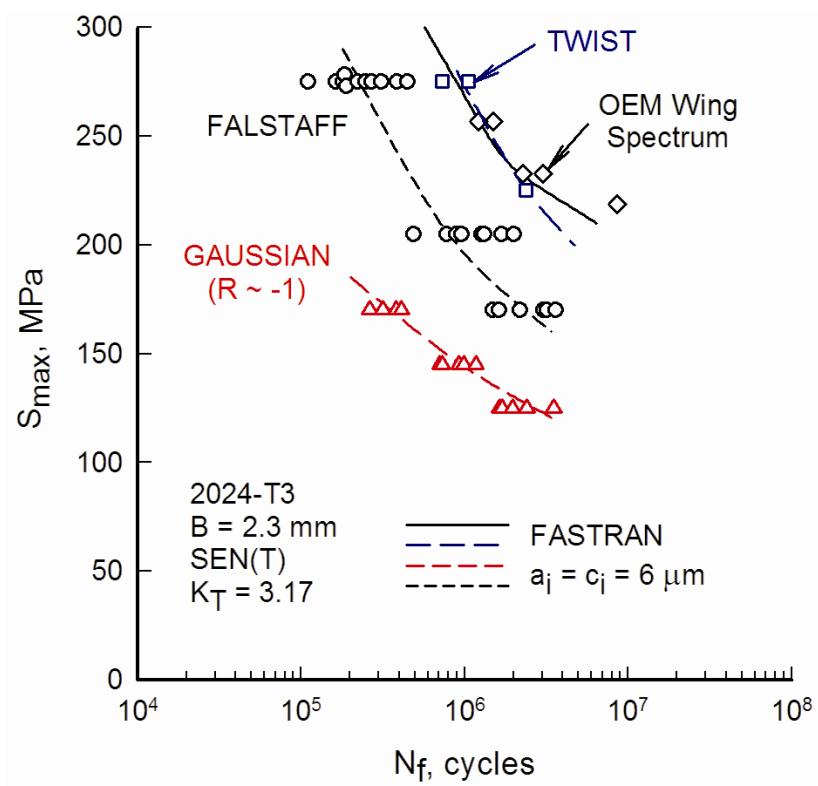

Figure 33. Fatigue Results on SEN(T) Specimens Made of 2024-T3 Aluminum Alloy Under Various Spectrum Loading

In figure 34, a more detailed fatigue life analysis was conducted on the FALSTAFF test data. The open symbol shows the test data generated at several laboratories in Europe and North America [21]. The solid symbol shows the average fatigue life at each maximum stress level, which fell extremely close to the predicted results using the 6-μm initial surface flaw. For the 2024-T3 alloy, a 30-μm inclusion particle cluster is near the maximum values recorded for this material [81] and predicted the lower-bound lives reasonably well. Predictions have also been made into the giga-cycle fatigue regime that shows the potential for a large amount of scatter in fatigue lives from the distribution of inclusion particle sizes. In a structural design, using the 30-μm EIFS may be a very reasonable approach and can cover for the weakest link in material behavior. However, larger EIFS may be required from possible manufacturing discontinuities.

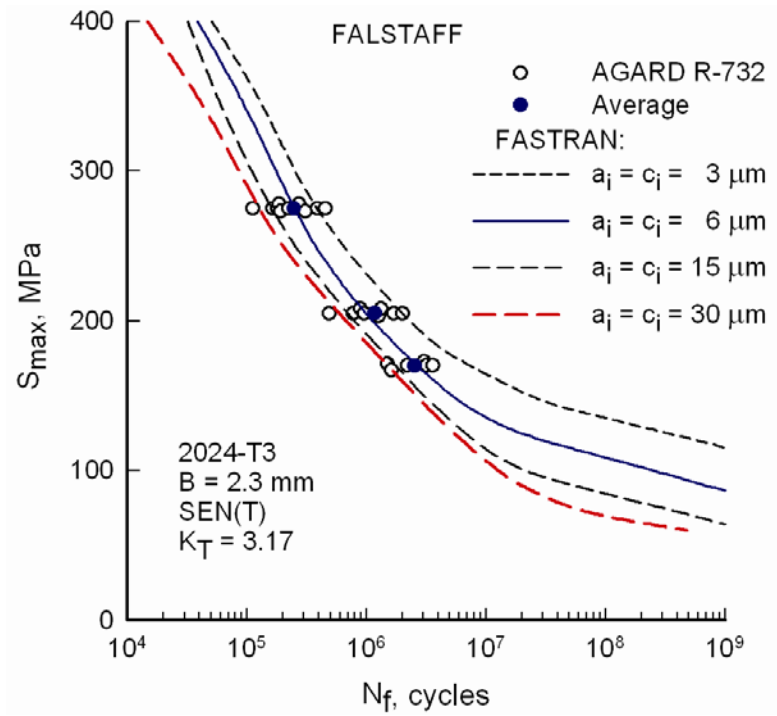

Figure 34. Fatigue Results on SEN(T) Specimens Made of 2024-T3 Aluminum Alloy Under FALSTAFF Loading

5.2 ALUMINUM ALLOY 2324-T39.

The C(T) specimens (B = 6.35 mm) were used to generate FCG-rate data on 2324-T39 aluminum alloy in the LT-orientation. The specimens were obtained from Alcoa, Inc. and some specimens had been previously tested to identify the load history effects during ASTM standard LR tests and to develop alternative test methods so that FCG-rate data could be generated without any significant load history effects [17]. The yield stress and the ultimate tensile strength was 408 and 519 MPa, respectively. Specimens had a width (W) of 76.2 mm and an initial notch length (measured from the pinhole centerline) of ≈30 mm, as shown in figure 5(b). In addition, the edges of the pinholes in the specimens were beveled to avoid or minimize unwanted out-of-plane bending movements (pins forced to contact near mid-thickness of specimen). All specimens were precracked under compression CA loading ($R \approx 12$; $P_{min} \approx$ -5.2 kN) to initiate a crack at the

machined crack starter V-notch with a 45°-included angle ($|K_{cp}|/E \approx 0.00032$ m$^{1/2}$). The FCG-rate tests were then conducted using constant K_{max} testing (shed rate of -0.4 mm^{-1} [3]), CPCA loading, or CPLR loading at constant R after a small amount of crack extension under CA loading. The LR tests were conducted when the FCG rate was 1E-9 to 3E-9 m/cycle, which is nearly an order of magnitude lower than the maximum rate allowed in the ASTM E-647 standard [3]. The FCG tests were performed under computer control on servohydraulic testing machines (25 kN capacity) in laboratory air at room temperature and humidity (≈ 30% RH). The loads were applied in sinusoidal waveform at 18 Hz in the low-rate regime and about 1 to 3 Hz in the high-rate regime. Crack lengths were monitored by using a BFS gage and occasionally calibrated with measurements made from a traveling optical microscope.

To measure load strain records near the crack tip, strain gages were mounted close to the crack path for the specimen tested for all test conditions (R = 0.1, 0.7, 0.9, and constant K_{max} test), except R = 0.95. The locations of the strain gages were chosen to be slightly off the anticipated crack path by approximately the crack-starter notch height (≈ 2 mm) and approximately 5 mm away from the crack tip after CP (figure 18). A number of strain gages were mounted along the anticipated crack path to record load strain records as the crack approached these gages. The optimum signals were obtained when the crack tip was about 2 to 3 mm away from the strain gage during threshold testing. Approximately 20 load strain records were recorded when the target FCG rates were achieved. During measurements, the frequency of cyclic loadings was reduced to 0.5 Hz to minimize external noise. The BFS and crack monitoring software recorded various compliance offset values using Elber's reduced strain approach [28]. In general, the results from the BFS showed the tail swing associated with crack-closure and the compliance offset values from 1% to 16%. The standard recommends the 2% (two percent offset compliance (OP2)) value, but the 1% (one percent offset compliance (OP1)) values were used.

5.2.1 Large Crack Behavior.

The FCG rate data on the 2324 alloy from a previous study [17] and the present results for R = 0.1 are shown in figure 35. The solid curves show CPCA tests at four different initial ΔP values and the loads were held constant throughout the tests. All CPCA tests showed the expected dip due to the decaying tensile residual stresses and stabilization of the crack opening loads under CA loading. The CPCA tests merged with each other after crack extensions of about three compressive plastic zone sizes. One test (lowest initial ΔP) had an inadvertent overload, but, before the overload, the rates were steadily increasing under CA loading. The open symbols show the results for the CPLR tests. After CP, the crack was grown to a particular ΔK value under CA loading. A standard LR test was then conducted at three different initial ΔK_i values. As shown, the lower initial ΔK_i values produced lower thresholds. The lowest ΔK_i values produced a threshold close to that estimated from the one CPCA test. An additional CPLR test was conducted in the present study, which agreed very well with the other test results in the threshold regime.

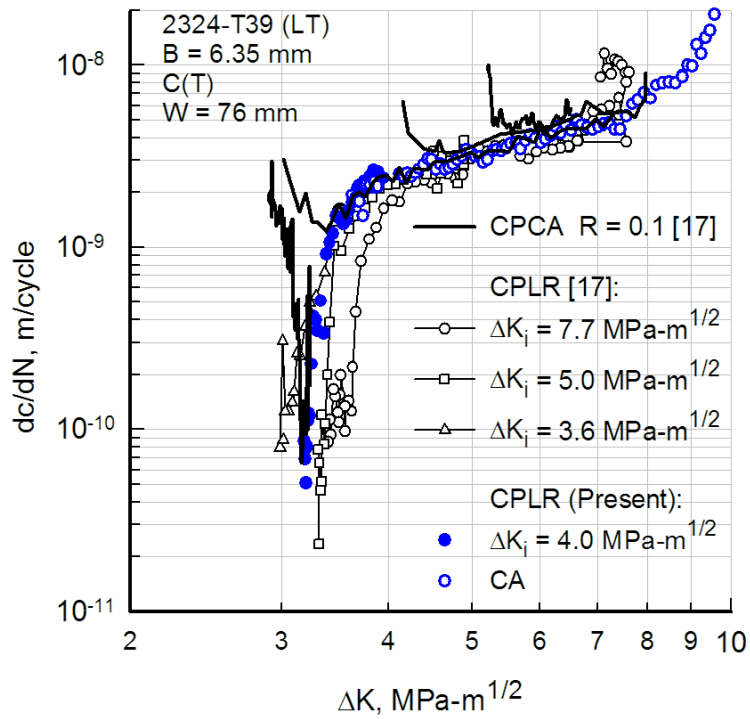

Figure 35. Comparison of FCG Data Generated From CPCA and CPLR Threshold Testing [17] and Present Results

The FCG tests were conducted over a wide range in load ratio conditions ($0.1 \leq R \leq 0.95$) and a constant K_{max} test. Figure 36 shows the test data, which generally ranged from threshold to near-fracture. All specimens were compression precracked before FCG testing. The solid symbol shows the CPLR test results and the open symbol shows the CA data. At high rates, the asymptote to fracture, as expected, was a function of the load ratio, R. In this regime, the critical stress intensity factor range at failure, ΔK_c, is given by K_{Ie} $(1 - R)$, where K_{Ie} is the elastic fracture toughness or maximum stress intensity factor at failure. Thus, at higher R-values, a crack will grow to failure at lower values of ΔK. In the near-threshold and mid-rate regimes, the R = 0.9 rates were higher than the R = 0.7 rates at the same ΔK value. The R = 0.9 test data agreed well with the constant K_{max} test data at low rates, which had R-values ranging from 0.1 at the start of the test to 0.88 near-threshold conditions. The constant K_{max} test and the other tests had the same characteristic shape of the FCG-rate curve in the threshold regime. The R = 0.1 test data showed a rapid acceleration from 5E-9 to 1E-7 m/cycle, whereas the R = 0.7 test data started accelerating at the same rate (5E-9 m/cycle), but showed a more gradual change in slope to higher rates. This acceleration zone at low-R is quite common in aluminum alloy C(T) specimens.

The results shown in figure 36 for the high-rate regime approaching fracture shows that the high-R tests grow to failure at lower ΔK values, as expected. However, the high-R test results demonstrate that there are significant differences between the R = 0.7 and 0.9 results in the threshold regime. In the literature, these differences have been attributed to the so-called K_{max} effects. For the 2024 alloy, section 5.22 investigates whether these differences could be explained by crack closure.

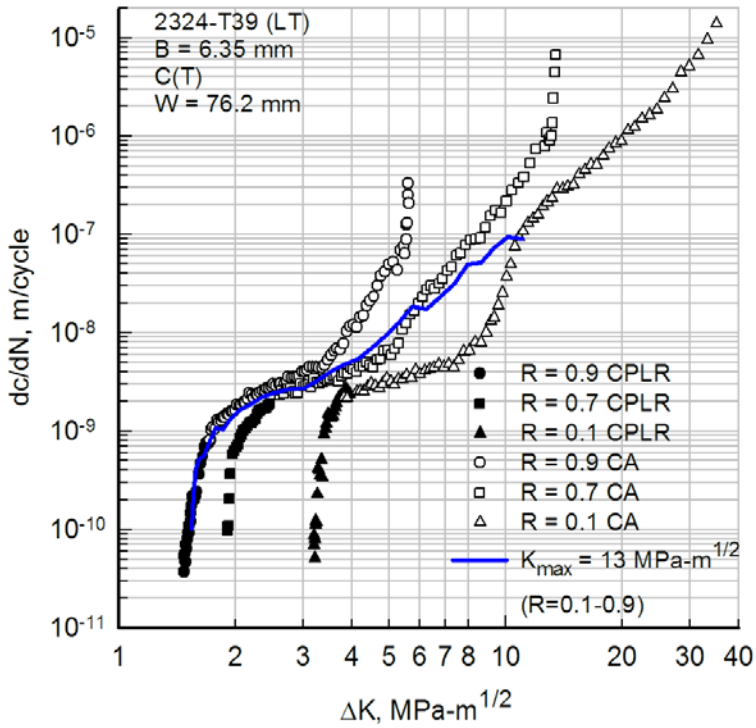

Figure 36. The FCG-Rate Data for Various Tests on 2324-T39 Aluminum Alloy

5.2.2 Crack Closure Behavior.

To improve the sensitivity and determination of crack opening loads, load strain records were measured from near-tip local strain gages and compared with remote strain gage readings during CPLR tests. Figure 37 shows results for an R = 0.1 test (the method used to generate load-reduced strain records is described in appendix A [28]). On the R = 0.1 test, the tail swings of load-reduced strain records from local gages were two to five times larger than the ones measured from the remote strain gage records. Because of better sensitivity, crack opening loads from local gages were easy to determine. Crack opening loads from the local gages were determined by inspection, whereas OP1 values came from the BFS gage readings made with the crack monitoring system [66]. Consistently, local gages showed higher crack opening loads than the remote gages, but both records showed the same trend in that the crack opening loads were rising as the FCG rate approached the threshold regime. The crack opening loads from the local gage gave slightly higher crack opening values than the results from using the OP1 values. These local gage measurements will be used later to develop crack closure corrected, ΔK_{eff}, results for the R = 0.1 test data.

Figure 38 shows some typical load-reduced strain records measured from a near-crack tip strain gage and the BFS gage at FCG rates approaching threshold conditions for R = 0.7. The ASTM E-647 [3] suggests using an OP2 change to determine crack opening loads from load-reduced strain (or displacement) records. However, because of the amplitude of noise and size of crack closure tail swing in the reduced-load strain records, the use of an offset value was not practical. Thus, the crack opening values from the remote gage were estimated.

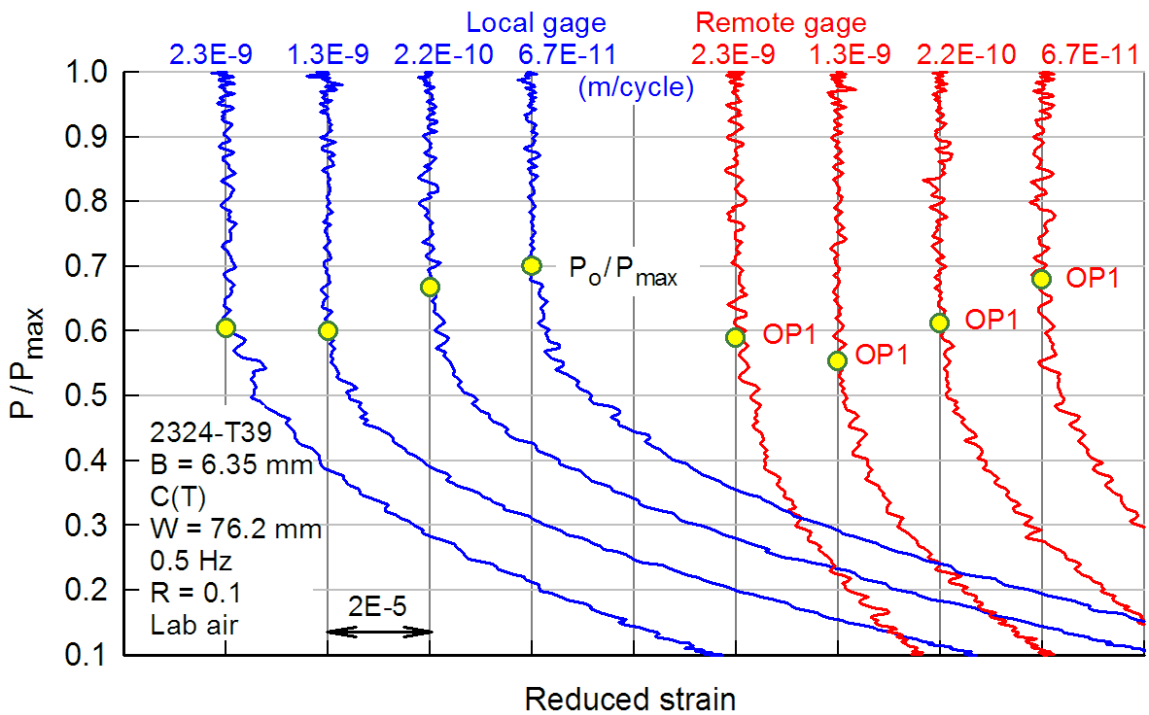

Figure 37. Comparison of Load-Reduced Strain Records Measured From Local and Remote Gages for $R = 0.1$ Loading

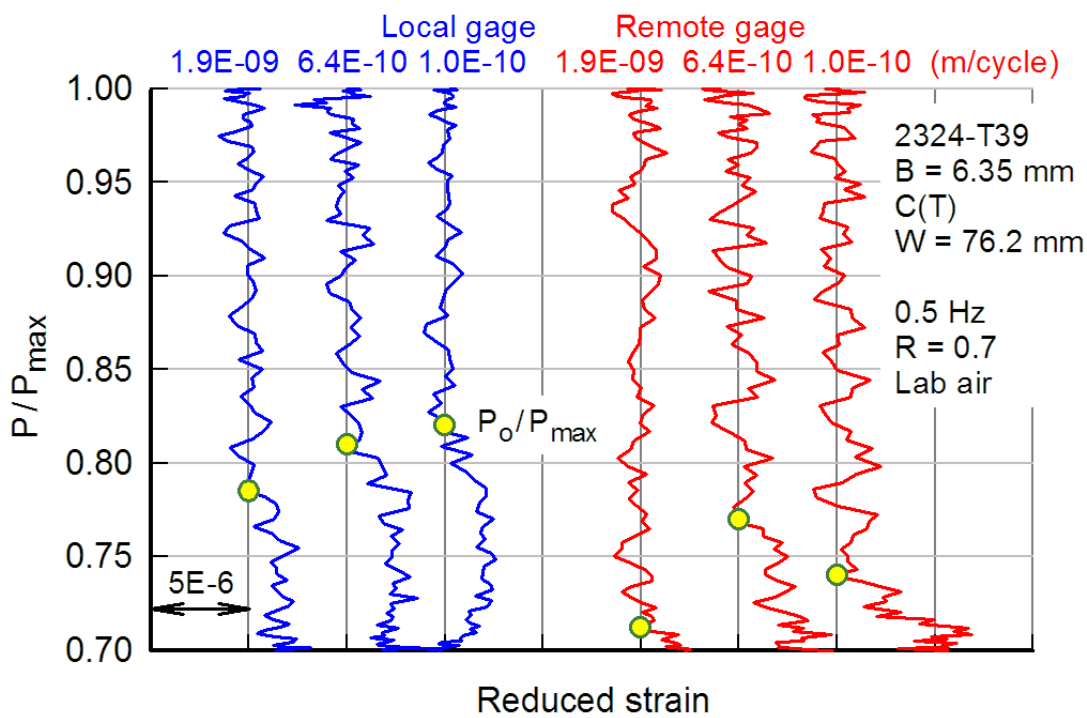

Figure 38. Reduced Load Strain Records for Several FCG Rates in Near-Threshold Conditions for $R = 0.7$ Loading

For high-R tests, all crack opening loads were determined by inspection for both local and remote gages because OP1 or OP2 readings from the crack-monitoring system were either not available or not reliable. Levels of noise were almost the same between the local and remote gages, but the shape of the load-reduced strain records were significantly different. Obviously, the local gage measured a clear indication of crack closure (a distinct transition from linear behavior) even at R = 0.7, which was surprising. The local gages almost always showed some amounts of crack closure in the near-threshold regime, whereas the remote gage consistently showed some indication of crack closure, but not as clear or consistent as with the local gages. In addition, the local gages always showed a rise in the crack opening load as the threshold was approached, but the remote gage results were inconsistent. This indicated that the remote gages are not sufficient to determine crack opening loads from remote measurements, especially at high R, and that local measurements have a great advantage in capturing the near-crack tip behavior.

Because crack closure behavior was observed on the R = 0.7 threshold test, measurements of load strain records from local gages for R = 0.9 and the constant K_{max} test were conducted to see if crack closure effects could be measured. Figure 39 shows a comparison of load-reduced strain records at a constant K_{max} (=13 MPa-m$^{1/2}$) test between local and remote gages. Here, the noise from the local gage was much less than with the remote gage. Also, the remote gage did not show a sign of crack closure, but the local gages showed a clear indication of crack closure behavior. At the load ratio of 0.79, 0.86, and 0.88, the local gage records indicated that the crack was fully opened at P_o/P_{max} of 0.84, 0.88, and 0.91, respectively. Another unexpected result is on the measurements made at R = 0.9, as shown in figure 40. Here, the measurements indicated a tail swing (or deviation from linear behavior) at an opening load ratio of 0.91 (U = 0.9).

The crack opening loads from all of the constant R and constant K_{max} tests were used to develop the ΔK_{eff}-rate data. These results are shown in figure 41(a). All of the crack closure corrected data have collapsed together into a tight band and the results are approaching a $(\Delta K_{eff})_{th}$ value at a threshold of about 1 MPa-m$^{1/2}$. These results suggest that the ΔK_{eff} against rate relation may be a unique function over a wide range of R in the threshold regime if the true crack opening load values were measured. Even the remote gage at R = 0.1 was showing ΔK_{eff} values (OP1) very close to the results from the local gages at high-R.

In an effort to generate crack-closure-free data in near-threshold conditions, a test at R = 0.95 was performed—though, unfortunately, without local strain gages. A CPLR test was conducted at an initial ΔK_i of 1.65 MPa-m$^{1/2}$ to generate near-threshold data, and these data are shown in figure 41(b). However, the data fell at higher ΔK values than the ΔK_{eff} regime at a given rate, but still was at lower ΔK values than the R = 0.9 and K_{max} tests. These results imply that there may be crack closure at R = 0.95. Since local gages were not used, there was no direct evidence from the load-reduced strain records. Instead, figure 42 shows photographs of a specimen at dc/dN = 1E-9 m/cycle at the maximum and minimum loads. These photographs show the growth of the crack under only CA loading and show that the near-crack tip region may be closed at minimum load. It appears that the crack surfaces are open beyond the contact region.

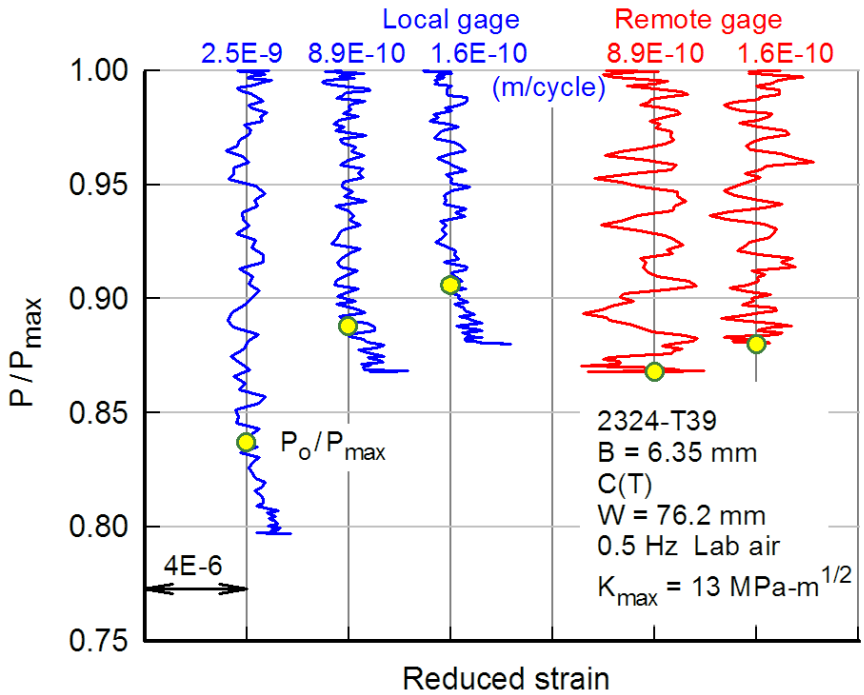

Figure 39. Comparison of Reduced Load Strain Records for Several FCG Rates in Near-Threshold Conditions During Constant K_{max} Test Loading

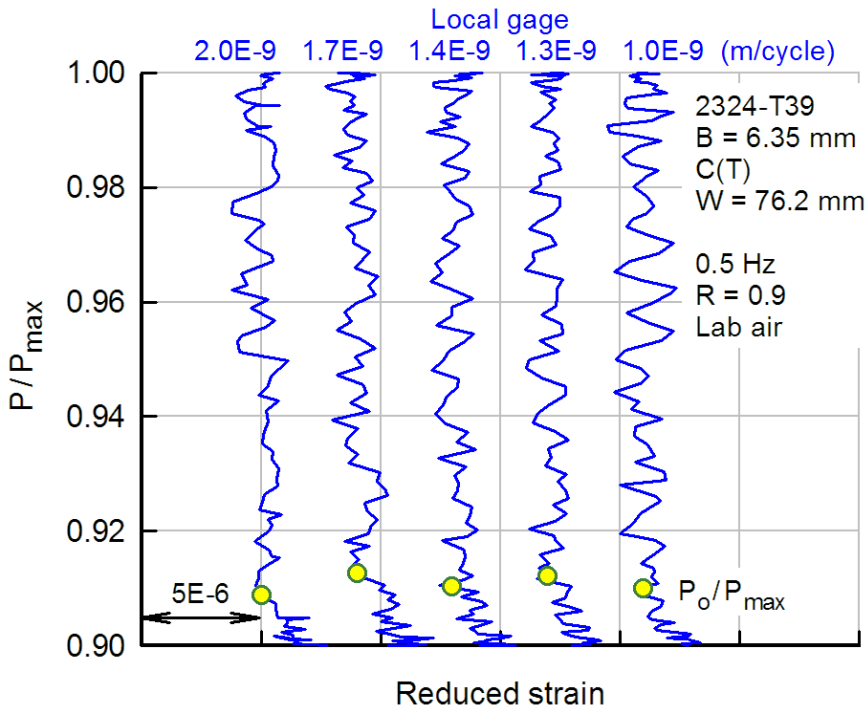

Figure 40. Reduced Load Strain Records for Several FCG Rates in Near-Threshold Conditions at R = 0.9 Loading

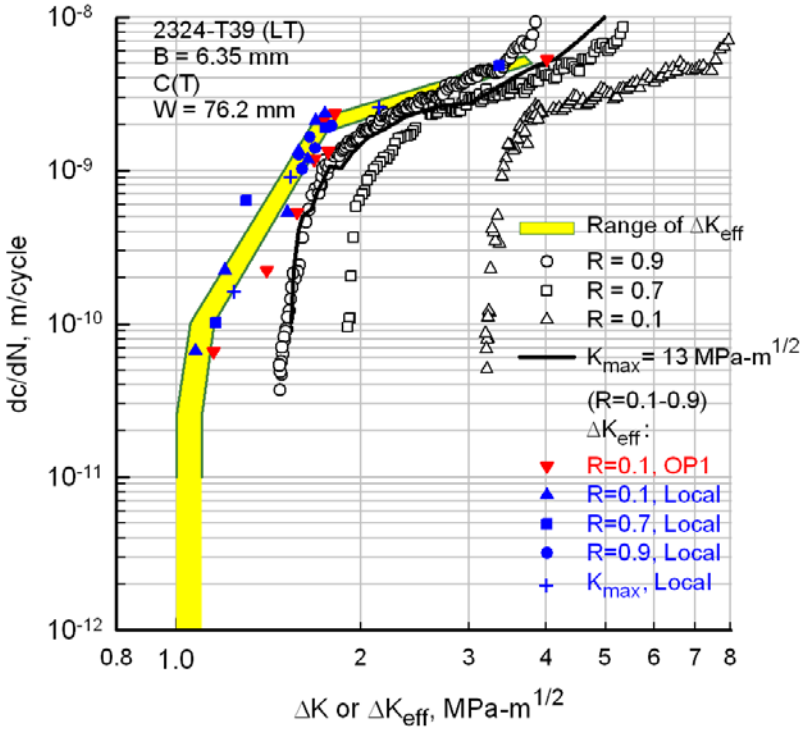

(a)

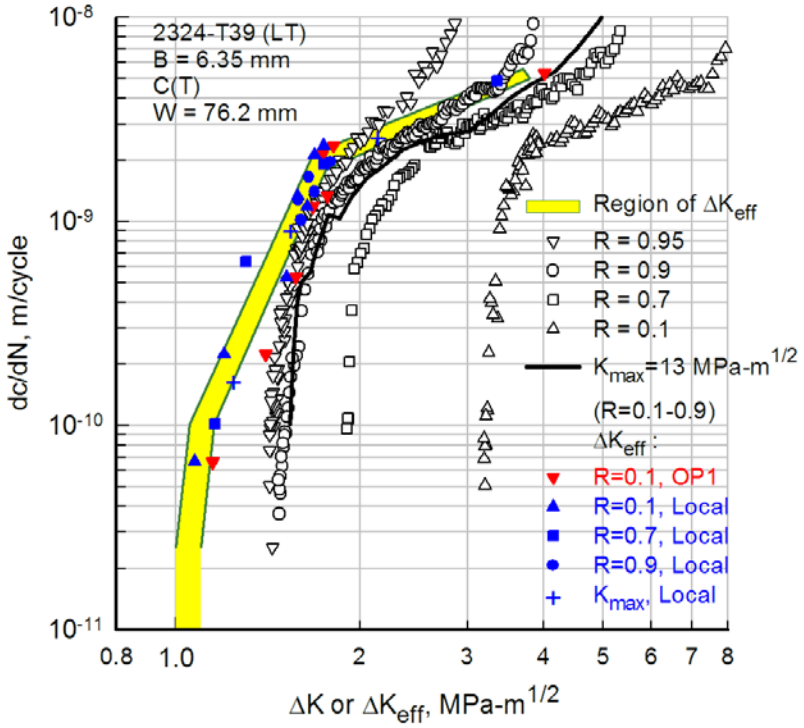

(b)

Figure 41. (a) Crack Closure Corrected Data Using Local Strain Gages for All Tests to Form a Unique ΔK_{eff} Region and (b) FCG Data at Extremely High R (0.95) Compared With All Other Test Data

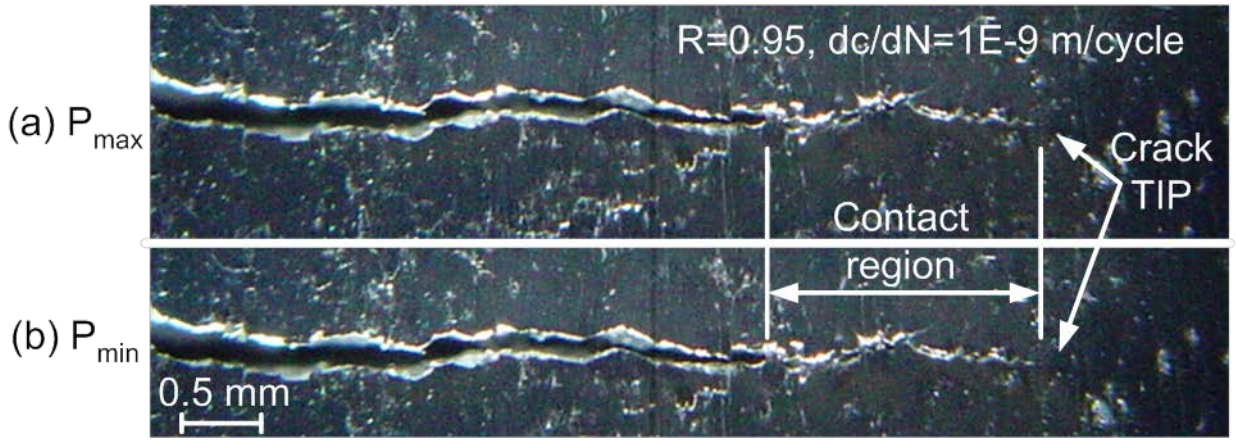

Figure 42. Photographs of FCG Showing Possible Near-Crack Tip Surface Contact at R = 0.95

Testing on 2324-T39 aluminum alloy has shown that near-threshold events, like threshold fanning with the R ratio and K_{max} effects, may be explained by the crack closure concept. Crack opening loads measured with the local strain gages consistently showed a rise in the P_o/P_{max} ratio as the threshold conditions were approached. Figure 43 shows the crack opening load ratios measured with the local strain gages over a wide range in R-values and the K_{max} test. The differences between the dashed lines and the measured values indicate the amount of crack closure for each R. Most of these tests were CPLR tests, but load history effects due to LR are not likely because of the very low initial ΔK_i values used, especially at high R. However, the question is what has caused the rise in crack closure behavior in the near-threshold regime.

In the literature, plasticity effects have been dismissed because the plastic zone sizes are very small near-threshold conditions, but crack surface displacements are also very small. The PICC is due to the interference between the residual plastic deformations and crack surface displacements. Thus, in the threshold regime, PICC is still a very dominant shielding mechanism at low R-values. Measurement of crack opening loads at the free surface may also record plane stress behavior instead of interior plane strain or average through-the-thickness behavior. How three-dimensional crack opening loads are used in a two-dimensional analysis is still unclear [67]. Crack opening loads at the free surface should affect the near-crack front strain ranges in the interior, but, at the small ΔK values, plane strain behavior should be dominant and plane stress behavior would be over a very small zone. In addition, PICC models [68] predict that, above $R \geq 0.7$, the cracks should be fully open under plane stress conditions, but the crack opening load is at the minimum load. Thus, any small contribution of roughness- and/or debris-induced crack closure could then cause the opening load to be higher than the minimum load, as measured on the 2324 alloy.

Since the near-crack tip strain gages are located 2 to 3 mm away from the crack front (B = 6.35 mm), the crack opening values measured at any R may be more of an average value through the thickness. The 2324-T39 alloy creates a very rough and tortuous crack surface, compared to 2024-T3 or 7075-T6. Thus, for high-R conditions, RICC is suspected to be a major contributor to the rise in the crack opening ratio level as the threshold is approached. Very rough crack

surfaces with contacting asperities may also create debris along the crack surfaces, so DICC is also suspected to be a major contributor to the rise in the crack opening ratio levels in the threshold regime for high-*R* [24].

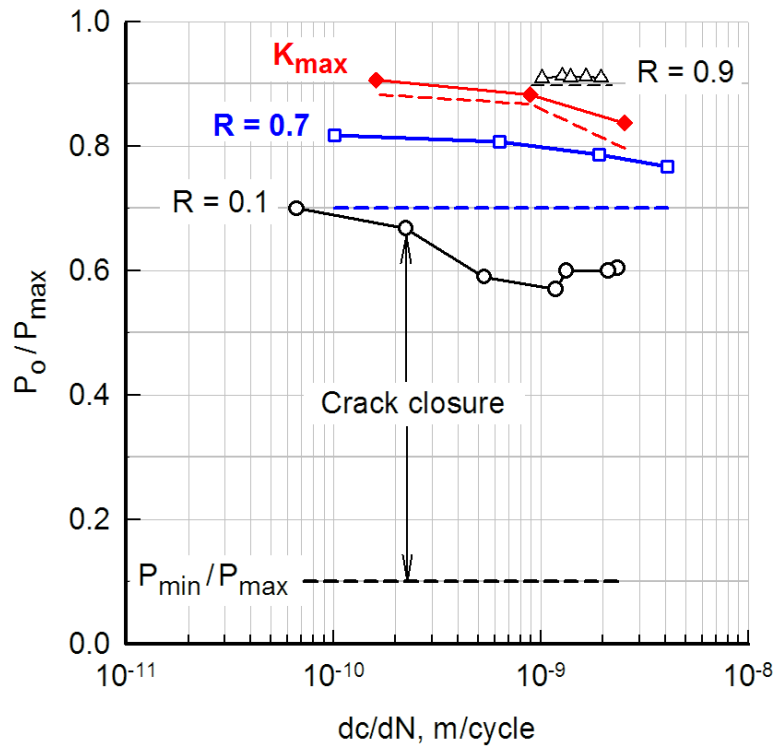

Figure 43. Crack Opening Load Ratios for Low *R*, High *R*, and K_{max} Test Results in Threshold Regime

5.2.3 Crack Closure Analysis.

A crack closure analysis of the FCG-rate data on the 2324-T39 aluminum alloy was made to correlate the test data into a narrow band over a wide range in stress ratios and rates from the threshold regime to near fracture. This effort requires finding a constraint factor (α) from the crack closure model [68-70] that would correlate the test data over a wide range in load ratios. Surprisingly, a very low constraint factor, α = 1.3, was found to correlate the test data reasonably well, as shown in figure 44. The fatigue crack surfaces of the 2324 alloy specimens were very rough and the crack paths were tortuous, which indicated that roughness-induced crack closure could have greatly affected the ΔK-rate data. Because the crack closure model was based only on plasticity, a low value of constraint was required to raise the crack opening loads, like those measured from the local strain gages (ideally, a combined model of plasticity-, roughness-, and debris-induced crack closure behavior is needed to more accurately model FCG in the 2324 alloy).

The solid curve with open symbols shows the ΔK_{eff}-rate baseline curve (see table 8) that was selected to fit the measured ΔK_{eff} data in the threshold regime and the low-*R* test data in the high rate regime. The selection of the baseline curve in the mid region is a best fit to the test data, but

trial and error procedures are used in both the threshold and fracture regions. The baseline curve below a rate of about 1E-09 m/cycle was obtained from the crack opening load measurements made on C(T) specimens at various stress ratios and K_{max} equal constant tests. Again, the ΔK_{eff}-rate data did not correlate very well in the threshold regime because the crack closure model was based only on plasticity, and roughness is expected to play a strong role in threshold behavior. These results also show the classic plateau that occurs on most aluminum alloys in the (1E-09 to 1E-08 m/cycle) rate regime.

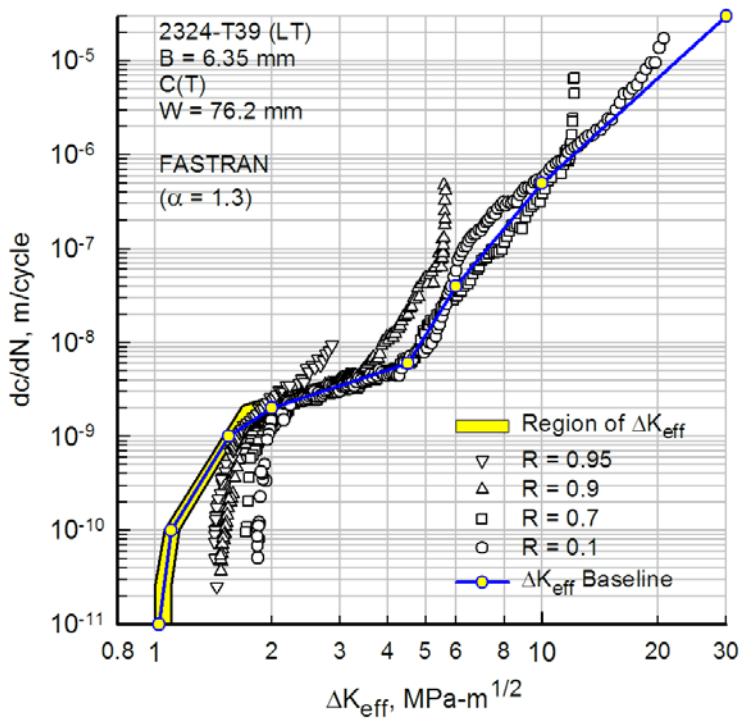

Figure 44. Effective Stress Intensity Factor Range-Against-Rate for the 2324-T39 Aluminum Alloy

Table 8. Effective Stress Intensity Factor Range-Against-Rate Relation for 2324-T39 Aluminum Alloy (B = 6.35 mm)

ΔK_{eff}, MPa√m	dc/dN, m/cycle	ΔK_{eff}, MPa√m	dc/dN, m/cycle
1.02	1.0e-11	10.0	5.0e-07
1.10	1.0e-10	30.0	3.0e-05
1.55	1.0e-09	α = 1.30	All rates
2.00	2.0e-09	C_3 = 1.85 MPa√m	C_4 = 0.1
4.50	6.0e-09	p = 6	---
6.00	4.0e-08	C_5 = 60 MPa√m	q = 2

The coefficients in the threshold term, $[1 - (\Delta K_o/\Delta K_{\text{eff}})^p]$, of equation 6 were evaluated by first determining the effective stress intensity factor range threshold, ΔK_o, as a function of R from the results shown in figure 44. The ΔK_o value for a given R is the limiting asymptotic value as the rate goes to zero and is not defined at a rate of 1E-10 m/cycle as specified in ASTM E-647. These results are shown in figure 45. The functional form selected is a power law equation, like that proposed by Klesnil and Lukas [90], except that the effective stress intensity factor range is used instead of linear elastic values. Fit to threshold data on the aluminum alloy is shown by the solid curve. The power term, $p = 6$ in equation 6, was selected to best match the shape of the ΔK-rate curves as threshold conditions were approached.

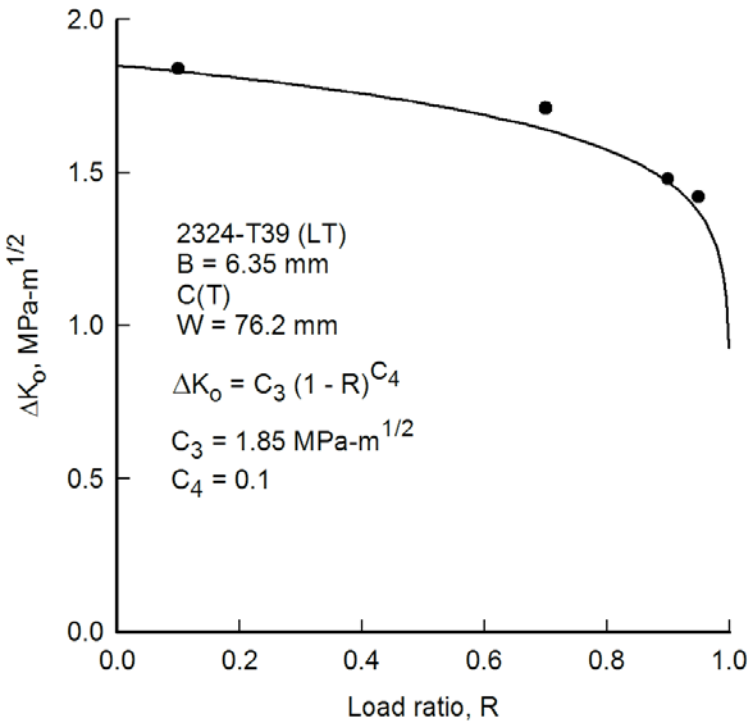

Figure 45. Effective Stress Intensity Factor Range Thresholds for 2324-T39 Aluminum Alloy

To evaluate the coefficients in the fracture term, $[1 - (K_{\max}/C_5)^q]$ in equation 6, the cyclic fracture toughness (C_5) must be determined. Normally, C_5 is equal to the elastic fracture toughness, K_{Ie}, which is usually a function of crack length, width, and crack configuration. The K_{Ie} is the elastic stress intensity factor at failure using the initial crack length and maximum failure load. But linear elastic fracture mechanics parameters, such as K, do not work very well for fracture. Nonlinear fracture mechanics concepts, such as J or CTOD, are required to correlate and predict the effects of crack length, width, and crack configuration on fracture. However, the TPFC [74 and 75] has been able to correlate and predict the effects of crack length, width, and, in some cases, crack configuration on fracture.

From the FCG results approaching fracture, the cyclic fracture toughness, C_5, was estimated at 60 MPa√m. It is suspected that the K_{Ie} values are not constant, but vary with crack length and specimen width. However, insufficient test data were available to conduct a proper TPFC analysis.

The power term q = 2 in equation 6 was selected to best match the shape of the ΔK-rate curves as fracture conditions were approached.

Figure 46 shows a comparison between measured and predicted FCG-rate behavior from the crack closure model at various load ratios (R). The solid lines with open symbols show the ΔK_{eff}-rate baseline results, which were used to predict the ΔK-rate curves for R, varying from 0.1 to 0.95 using equation 6 with the parameters given in table 8. The solid curves show the predicted curves for various R that fit the threshold and fracture regions quite well. In the midregion, the method slightly underpredicted the low-R test data, but overestimated the R = 0.7 data.

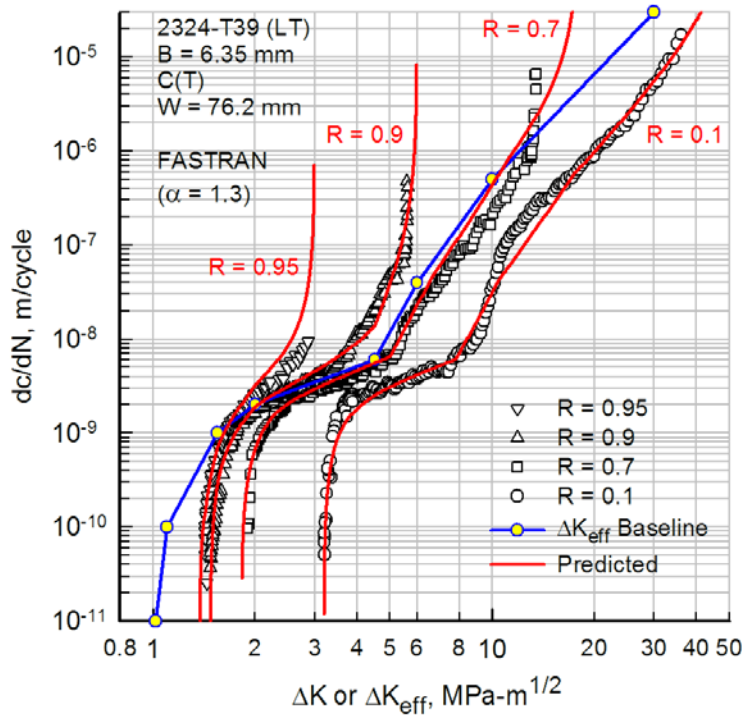

Figure 46. Linear Elastic Stress Intensity Factor Range-Against-Rate for the 2324-T39 Aluminum Alloy

5.3 ALUMINUM ALLOY 7050-T7451.

Previous studies on the 7050-T7451 aluminum alloy [41, 63, and 91] have identified that fatigue cracks develop very rough fatigue crack surface profiles. These profiles cause very high crack-closure levels due to a combination of plasticity, roughness, and, possibly, debris. Recently, tests [27] were conducted on C(T) specimens to generate FCG-rate data from threshold to near-fracture over a wide range in stress ratios (R). The near-threshold data were generated using the new threshold-testing methods, based on CP.

The plasticity-induced crack closure model, FASTRAN, was used to correlate the FCG data over a wide range of stress ratios and rates from threshold to near fracture to generate a ΔK_{eff}-rate curve. To account for the very high crack closure levels, a very low constraint factor, like plane stress (α = 1.3) conditions, had to be used in the model. In addition, the crack opening loads

were also measured during these tests using a local strain gage method to generate another ΔK_{eff}-rate curve. These two curves differed only in the threshold regime, presumably due to roughness.

The purpose of this work was to conduct crack growth and fatigue tests on the same batch of 7050-T7451 alloy, as tested in reference 27, and to predict crack growth and fatigue behavior under a wide range of loading conditions. The FCG tests were conducted on standard C(T) specimens under single-spike overloads and simulated aircraft spectrum loading. Also, fatigue tests on SEN(B) specimens were conducted over a wide range of loading conditions (CA and three aircraft spectra). All specimens were machined from a single forged block of 7050-T7451. However, no residual stresses were measured in the C(T) [27] and SEN(B) specimens (see figure 16). Three European standard spectra were used, but modified to have only tension-tension loading by adding a mean load and maintaining the same load amplitudes and sequences. They were Mini-Falstaff [58 and 59] and Mini-TWIST (levels 1 and 3) [60 and 61] spectra. One of the objectives of this work was to evaluate the two different effective stress intensity factor curves on making crack growth and fatigue life predictions. Small crack theory was used to make fatigue life predictions on the SEN(B) specimens using inclusion particle sizes from the literature [63]. For the C(T) specimens, comparisons were made on a single-spike overload test and tests under the Mini-Falstaff+ spectrum loading.

Two specimen types were tested and analyzed in the current study on the 7050-T7451 aluminum alloy (LT-orientation). Figure 5 shows the C(T) specimen (B = 6.35 mm) that was used to generate FCG-rate data [27] over a wide range in the stress ratios (R). Some of these data are repeated here for completeness. In the current study, the effects of a single-spike overload on crack growth delay and crack growth under an aircraft spectrum loading (Mini-Falstaff+ [92]) were determined. The C(T) specimens were obtained from the NASA LaRC. Some had also previously been tested at LaRC under ASTM standard LR and CPCA loading procedures [27]. The yield strength was 470 MPa, the ultimate tensile strength was 525 MPa, and the modulus of elasticity was 76 GPa. Specimens had a width (W) of 50.8 mm. The specimens did not have the standard V-notch, but had an electrical discharge machining (EDM) rectangular notch 10-mm long, measured from the pinhole centerline, with a total notch height of 0.25-mm. In addition, the edges of the pinholes in the specimens were beveled to avoid or minimize unwanted out-of-plane bending movements (pins forced to contact near midthickness of specimen) [27].

5.3.1 Large Crack Behavior.

Standard C(T) specimens were tested to generate the ΔK-against-rate data over a wide range in stress ratios (R) from threshold to near fracture. These data were used to generate the crack closure based ΔK_{eff}-rate curve that will be used to make FCG predictions on C(T) specimens and fatigue life predictions on SEN(B) specimens subjected to a wide range in loading conditions.

Figure 47 shows the ΔK-rate data generated on a range of stress ratios using the CPLR test method in the low-rate regime and CA loading at higher rates. In addition, two K_{max} tests were conducted to generate data at very high-R [27].

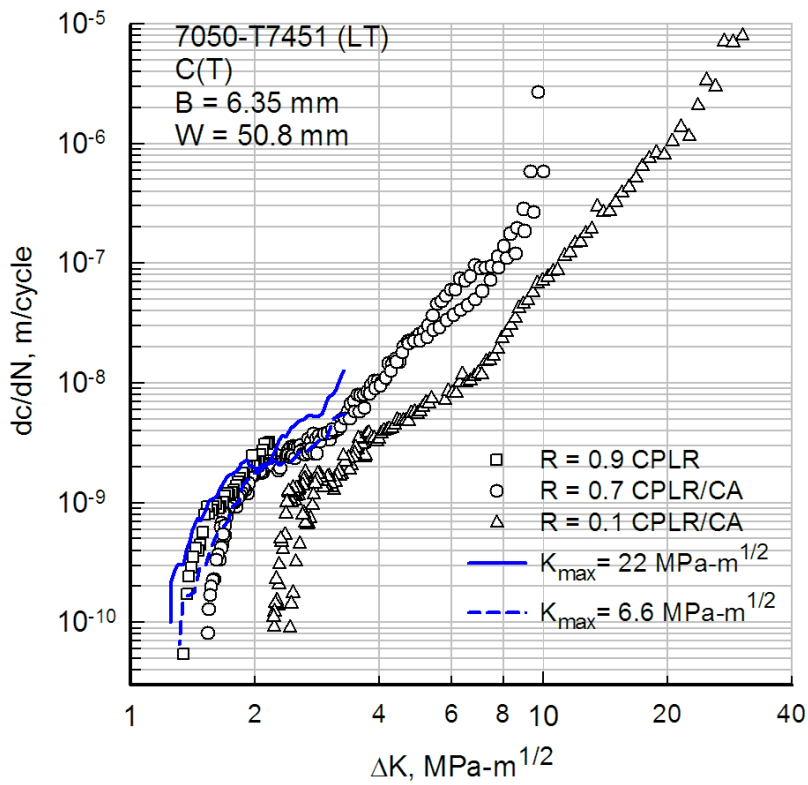

Figure 47. FCG-Rate Data on the 7050-T7451 Aluminum Alloy

5.3.2 Crack Closure Behavior.

During testing of the C(T) specimens, crack lengths were monitored using compliance data from BFS gages. Compliance data from the closure-free portion of the load cycle are used to determine crack length, enabling the tests to be automated and computer controlled. Load-against-strain data can also be used to measure crack closure events. A typical load-against-BFS record during a CPLR (threshold) test is presented in figure 48(a) for R = 0.1. The compliance is constant at high loads (open crack), which appears as a linear section in the upper portion of figure 48(b). As the load decreases, crack surfaces contact and produce a change in compliance. The reduced strain (or displacement) technique was developed to improve detection of these subtle compliance changes [28], as described in appendix A. The reduced strain, $\Delta\varepsilon$, is the deviation from closure-free compliance behavior. Closure-free behavior on these plots becomes a vertical line, making compliance deviations easier to detect from load-against-reduced-strain records. Using the reduced strain method, significant deviation is observed at low loads (P/P_{max} < 0.7) in figure 48(b). The very high crack opening load was suspected to be caused by plasticity- and roughness-induced crack surface contact. However, this method does not provide information about the location of crack face contact because it relies on changes in compliance to determine closure (or crack opening) levels.

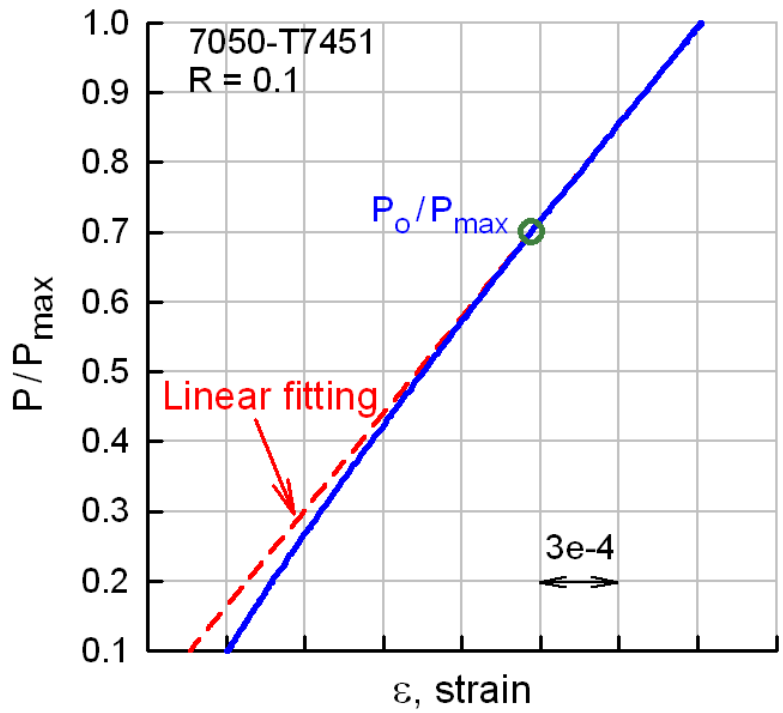

(a)

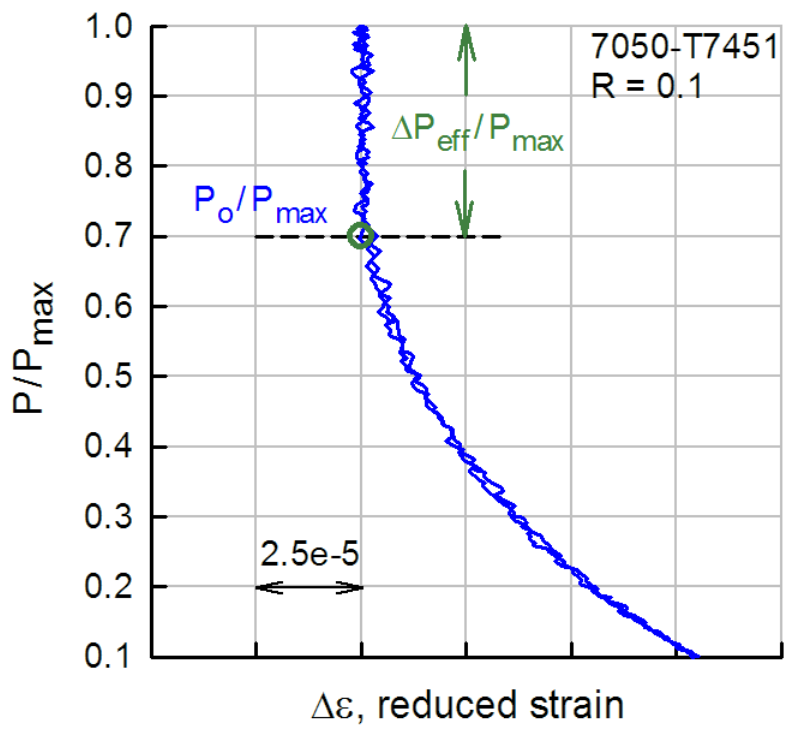

(b)

Figure 48. (a) Load-Against-BFS on a C(T) Specimen Tested at Low-*R* on the 7050-T7451 Aluminum Alloy and (b) Elber's Method of Determining Crack Opening Loads

Recently, Yamada and Newman [24 and 25] used local strain gages mounted on one side of C(T) specimens to measure crack opening loads. In measuring load-strain records, either from BFS or local strain gages, it is very important that nonlinearities, such as those due to out-of-plane bending or other causes, are not present in the measured data (beveling the pinholes in the C(T) specimens also reduced any out-of-plane bending, which helped in maintaining linearity). Thus, a notched C(T) specimen was tested without a fatigue crack to verify the linearity of the local load strain records. Figure 49 shows load-against-reduced-strain records for a notched and cracked specimen at low- and high-R ratios. The records with only a notch were very linear, while the records with a fatigue crack showed the typical crack closure behavior. Where the nonlinear curve meets the upper linear portion is assumed to be the crack opening load [28]. These results show that even the R = 0.7 near-threshold test developed crack closure, which was not expected. The literature has suggested that high-R tests are crack-closure-free, but Yamada and Newman [24 and 25] showed that high-R and K_{max} tests on a variety of materials develop significant crack closure behavior in the threshold regime because of plasticity, roughness, and debris.

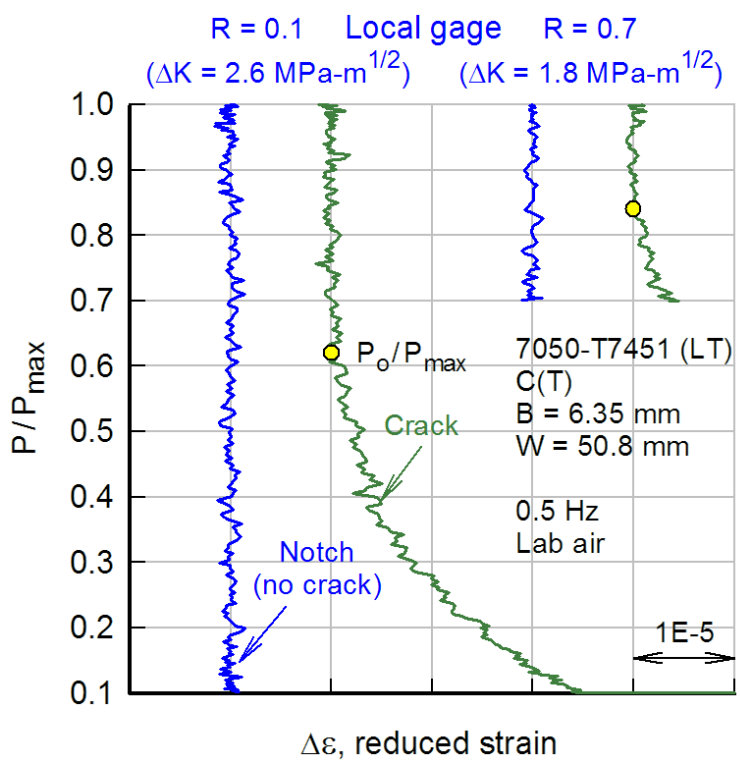

Figure 49. Crack Opening Loads on Typical Low-R and High-R Test Cases

Another issue is crack opening loads in the interior (near-plane-strain behavior) versus those measured at the free surface (plane stress). How three-dimensional crack opening loads are used in a two-dimensional FCG analysis is still unclear [67]. Crack opening loads at the free surface should affect the near-crack front strain ranges in the interior, but, at the small ΔK values near threshold, plane strain behavior should be dominant and plane stress behavior would be over a very small zone. In addition, PICC models [68] predict that, above $R \geq 0.7$, the cracks should be fully open under plane stress conditions. However, for high-R conditions, the crack opening load

from PICC modeling is at the minimum load. Thus, a small amount of debris- or roughness-induced closure, in addition to that caused by PICC, could cause high-R closure. As shown in figure 49 at R = 0.7, if PICC did not happen at high-R, then the small amount of debris- or roughness-induced crack closure would not have caused high-R closure.

Initially, Elber [28, 39, and 93] used a local displacement gage to measure crack opening loads. However, this method was more complicated than using a remote CMOD or BFS gage. Thus, the remote method was standardized in ASTM E-647, even though recent local crack opening load measurements indicate that the remote method may not be sensitive or reliable enough for high-R test conditions. Some local crack opening load measurements are shown in figure 50 for R = 0.1 loading, which shows very high crack opening loads as threshold conditions are approached. Although this is not shown, the BFS remote method also produced results similar to those shown in figure 50 [27]. Both methods produced very high crack opening load (P_o/P_{max}) ratios. The OP1 and OP2 values from the remote gage were extremely high as the threshold conditions were approached. The P_o/P_{max} values from the local gage were only slightly lower than the remote gage at threshold conditions, but were still very high.

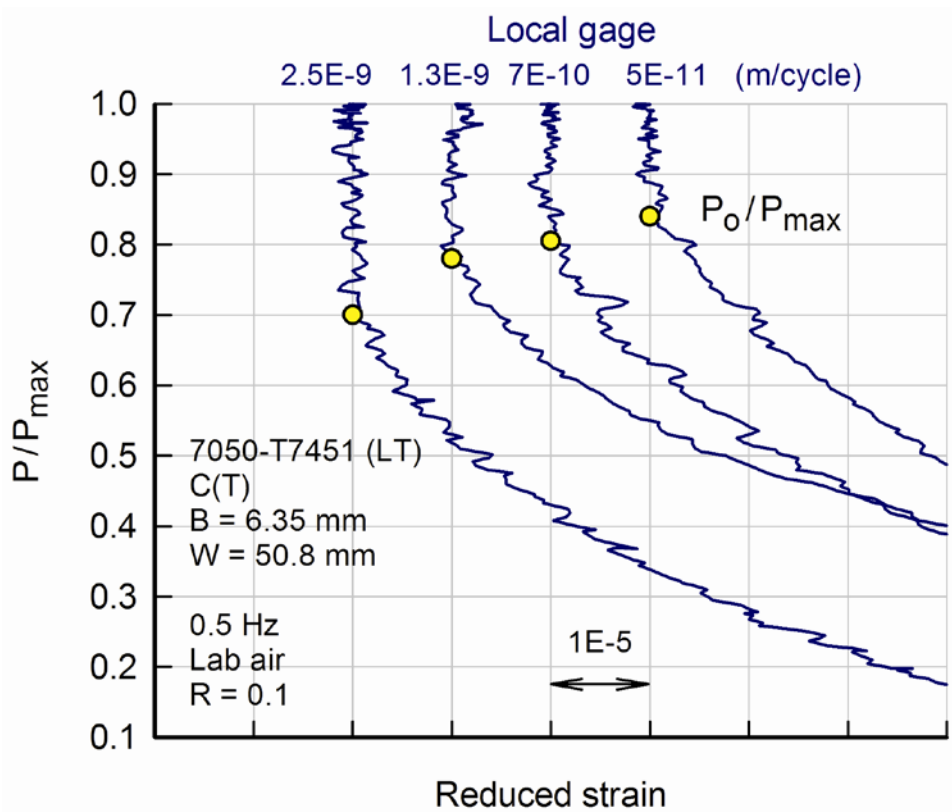

Figure 50. Crack Opening Measurements From Local Strain Gages for R = 0.1 Loading

For R = 0.7 (figure 51) and K_{max} (figure 52) test conditions, on the other hand, the local gage produced slightly higher opening load ratios than the remote gage. Crack closure behavior was even observed on a K_{max} test at very high load ratios (as high as 0.94) as threshold conditions were approached.

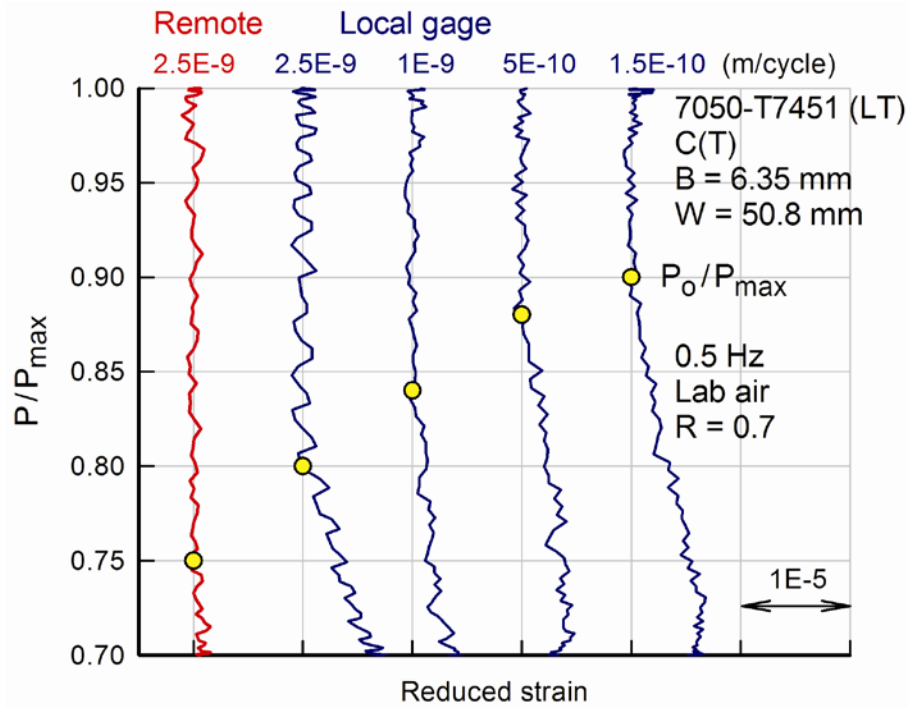

Figure 51. Crack Opening Measurements From Local Strain Gages for $R = 0.7$ Loading

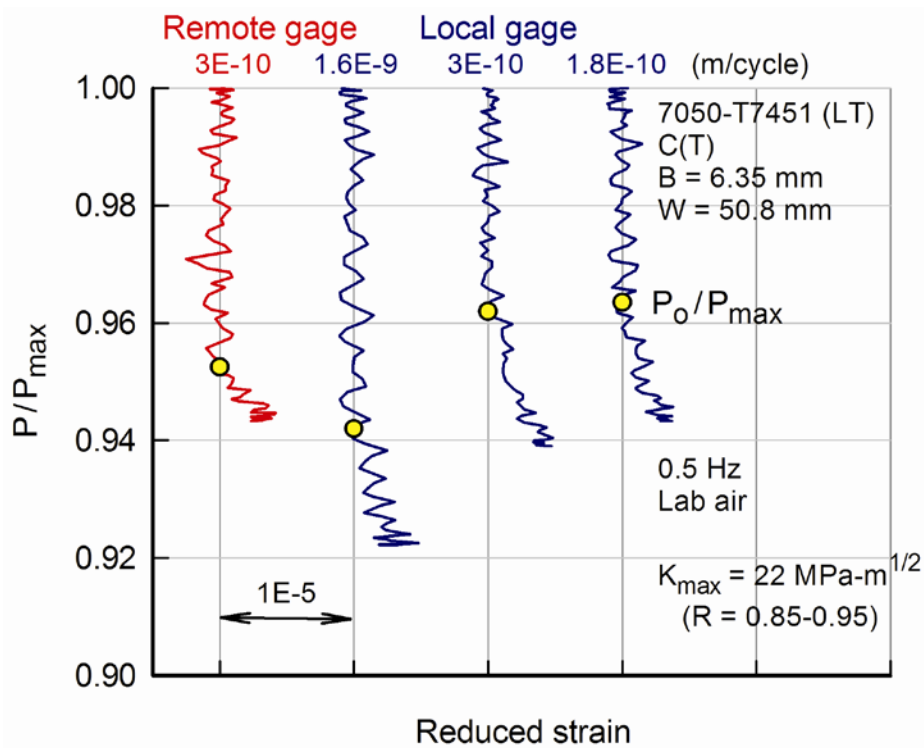

Figure 52. Crack Opening Measurements From Remote and Local Strain Gages for Constant K_{max} Test

5.3.3 Crack Closure Analysis.

Using the measured crack opening load, P_o/P_{max}, ratios from the local strain gages, the ΔK_{eff} values were determined as:

$$\Delta K_{eff} = (1 - P_o/P_{max}) / (1 - R)\, \Delta K \tag{7}$$

These results were compared with the ΔK-rate data generated at constant R and two K_{max} tests in figure 53. Because of the very high crack opening load ratios, the ΔK_{eff} data fell at very low-stress intensity values in the near-threshold regime, but fell slightly to the upper bound of the R = 0.7 results in the mid- and upper-rate regions. This implies that, in the mid- to upper-rate regions, only a slight amount of crack closure is occurring at R = 0.7, as was expected considering previous research. The open-diamond symbols show the results from an R = 0.1 test using OP1 values measured from a BFS gage over a wide range in rates. From previous research [24-27], OP1 values from remote gages were only slightly lower than crack opening values measured with local strain gages for the low-load ratio conditions, like R = 0.1. For high-R values, the remote gages were found to be inadequate.

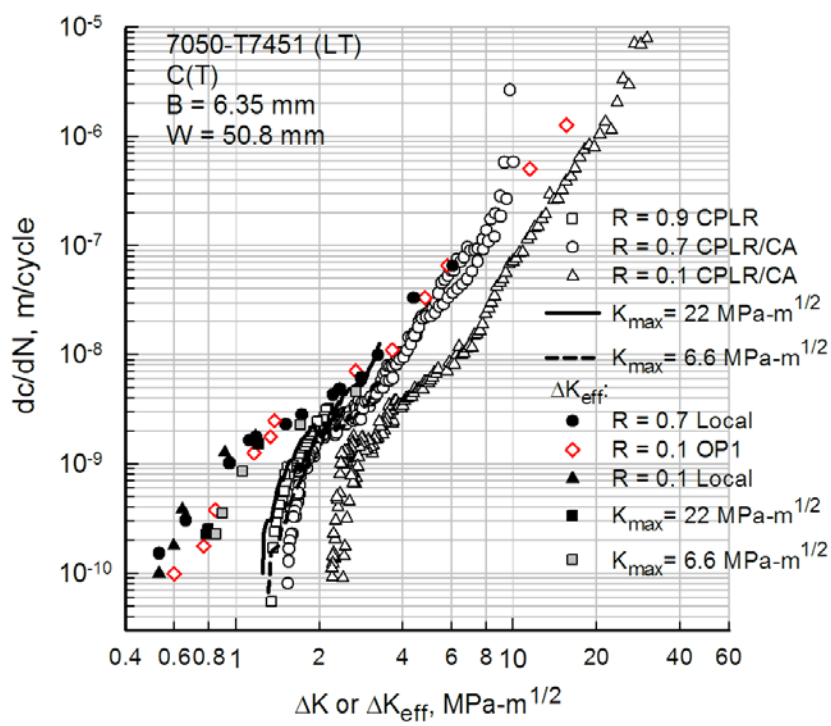

Figure 53. The FCG-Rate Data Using Measured Crack Opening Loads on CA Tests

The crack closure model FASTRAN [16 and 94] was then used to find a constraint factor (α) that would correlate the ΔK-rate data into a tight band on a ΔK_{eff} plot, as shown in figure 54. Surprisingly, a very low constraint factor (α = 1.3) was required. The data correlated very well and even collapsed onto a unique curve in the near-threshold regime, but the data were very different from the measured ΔK_{eff} values. The discrepancy is because FASTRAN is a PICC

model and roughness/fretting debris play a dominant role in the threshold regime. At the high rates, the results show the usual *R* dependency on the approach to fracture. The crack closure model was able to collapse the CA FCG data into a fairly tight band over a wide range in *R* and rates, but caution should be exercised for variable amplitude and spectrum loading. Having a plasticity parameter, such as α, correct for roughness/debris effects could lead to inaccurate life predictions. However, these effects are beyond the scope of the present report. Combined plasticity-, roughness-, and/or debris-induced crack closure modeling, such as that by Newman et al. [95 and 96] and Kim and Lee [97], may be required to produce accurate life predictions.

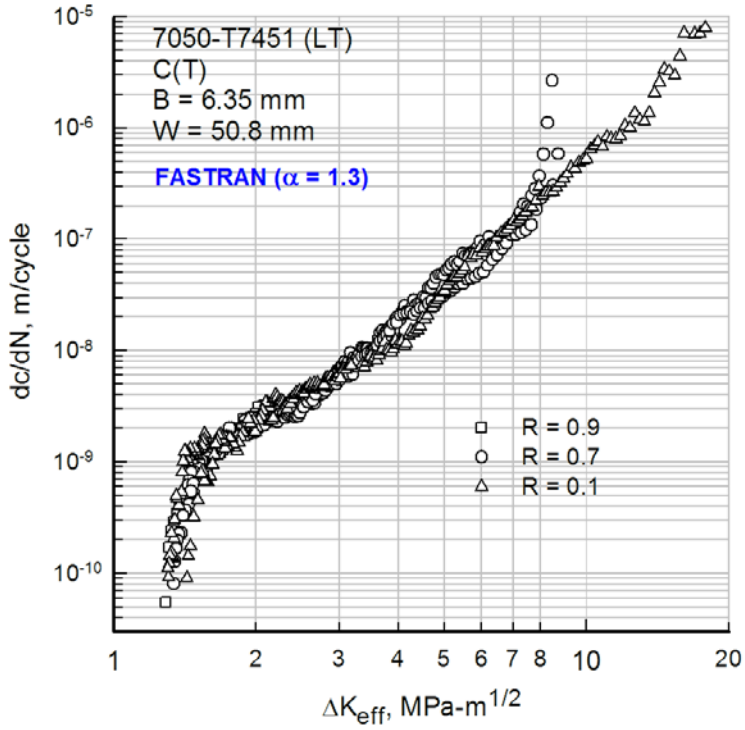

Figure 54. The FCG-Rate Data Using Calculated Crack Opening Loads on CA Tests

Figure 55 shows a comparison of the two different ΔK_{eff}-rate data sets for the 7050 alloy. The solid lines with circles show the selected ΔK_{eff}-rate (upper-bound) curve, whereas the solid lines with squares show the selected lower-bound curve. These ΔK_{eff}-rate curves are listed in table 9. The lower sections of the two ΔK_{eff}-rate curves have been estimated since no data were generated at extremely low rates. Further study is required to develop methods to generate ultra-low FCG-rate data. However, since fatigue damage is caused by plasticity, microplasticity in the microstructure (around inclusion particle clusters) of the aluminum alloy could cause microcracks to grow at these extremely low rates.

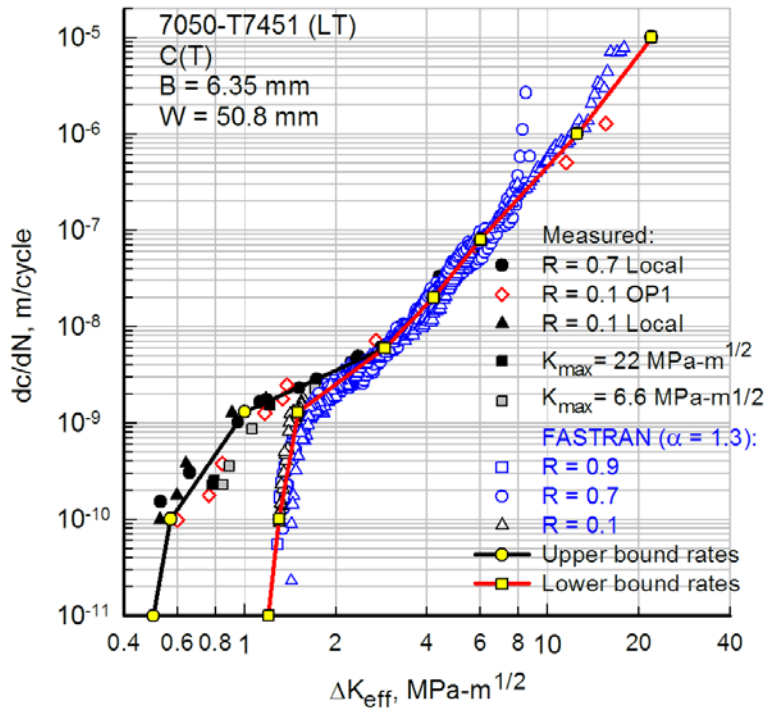

Figure 55. Comparison of FCG-Rate Data Using Measured and Calculated Crack Opening Loads

Table 9. Effective Stress Intensity Factor Range-Against-Rate Relations for 7050-T7451 Aluminum Alloy (B = 6.35 mm)

ΔK_{eff}, MPa√m		Rate
Upper-bound	Lower-bound	dc/dN, m/cycle
0.50	1.20	1.0e-11
0.57	1.30	1.0e-10
1.00	1.50	1.3e-10
2.90	2.90	6.0e-09
4.20	4.20	2.0e-08
6.00	6.00	8.0e-08
12.5	12.5	1.0e-06
22.0	22.0	1.0e-05
α = 1.3	α = 1.3	All rates
C_5 = 40 MPa√m	C_5 = 40 MPa√m	σ_o = 498 MPa

5.3.4 Small Crack Behavior.

Small crack data were not generated on the 7050-T7451 alloy tests conducted at MSU. However, Barter et al. [63 and 98] and Liao et al. [99] generated small crack data for the 7050 alloy in the T7451 and T7452 tempers, respectively. Walker and Barter [100] compared small crack data for the 7050-T7451 alloy with the ΔK_{eff}-rate (upper) curve in figure 55. Their results compared fairly well with the large crack data, but their data were not corrected for any crack closure effects that may have occurred in the small crack tests.

Barter et al. [63] did an extensive study on the growth of small cracks from initiating inclusion particle sizes for the 7050 alloy. Figure 56 shows the cumulative distribution function for inclusion particle depths on high stress concentration (K_t = 3) coupons. The median particle depth was about 12 μm, whereas the 10 and 90 percentile depths were 4 and 30 μm, respectively. These inclusion particle distributions were used with small crack theory to make fatigue S-N predictions on SEN(B) fatigue specimens subjected to either CA or spectrum loading.

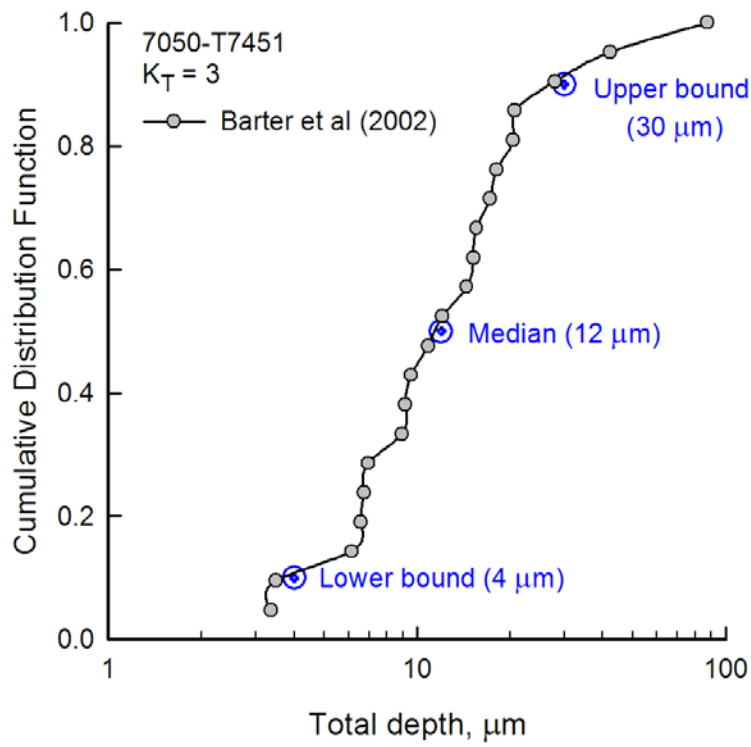

Figure 56. Cumulative Distribution Function for Inclusion Particle Depths on 7050-T7451 Aluminum Alloy

5.3.5 Fatigue Behavior.

The SEN(B) specimen was designed to be a small crack and fatigue specimen that could be loaded by pin clevis fixtures. For the 7050 alloy, fatigue tests were conducted on SEN(B) specimens under four loading sequences: (1) CA loading at a stress ratio of 0.1, (2) Mini-Falstaff+ loading, (3) Mini-TWIST+ (Level 1) loading, and (4) Mini-TWIST+ (Level 3) loading.

Fatigue life predictions were made with the crack closure model, FASTRAN [16], for all four load sequences applied to be SEN(B) specimens using the median inclusion particle depth with the upper- and lower-bound ΔK_{eff}-rate curves. The initial discontinuity was assumed to be a semicircular surface crack or void (a_i = c_i = 12 μm; h_n = void height = 6 μm) located at the center of the edge notch, based on the microstructural studies of Barter et al. [63]. The crack depth, a, is measured in the thickness direction and the crack length, c, is measured in the width direction. Two- and three-dimensional stress intensity factor solutions were developed for the SEN(B) specimen and incorporated into the FASTRAN code [101].

5.3.5.1 The CA Loading.

Figure 57 shows the fatigue S-N data on the SEN(B) specimens tested at R = 0.1 loading (symbols). The nominal stress, $P_{max}/(WB)$, was plotted against the fatigue life, N_f. The solid and dashed curves show the predicted fatigue lives using the lower- and upper-bound curves, respectively. For LCF, both curves predicted essentially the same fatigue lives that agreed well with the test data. However, at the lower applied stress levels, the lower-bound curve slightly overpredicted the fatigue lives, while the upper-bound curve was highly conservative.

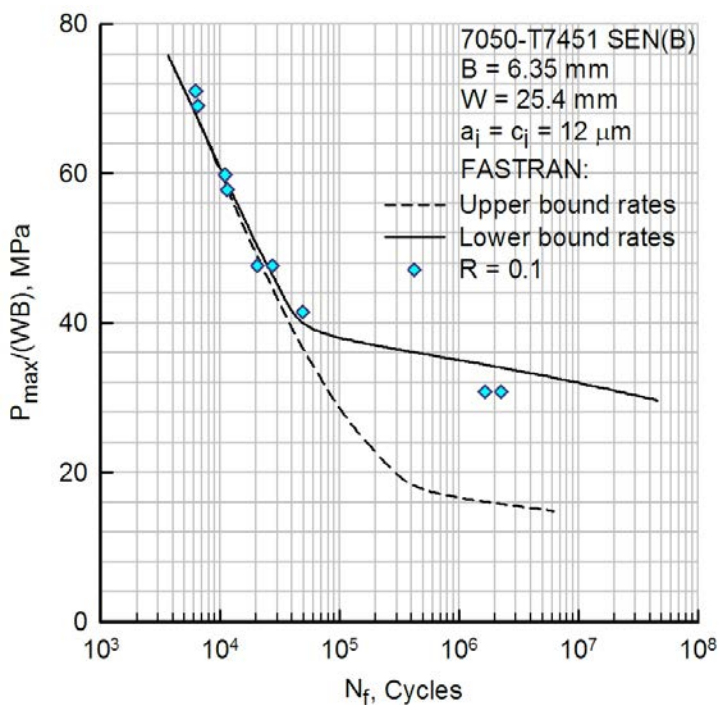

Figure 57. Fatigue Behavior Under CA Loading for the Two ΔK_{eff}-Rate Curves

Figure 58 shows how the initial discontinuity size influenced the predicted fatigue lives. For LCF conditions, the EIFS had some influence on the fatigue lives, but, at HCF conditions, the EIFS had a very large influence on the fatigue lives, as expected. Since the results using the median flaw size agreed well with the CA test data, the median flaw size was used for all spectrum load cases.

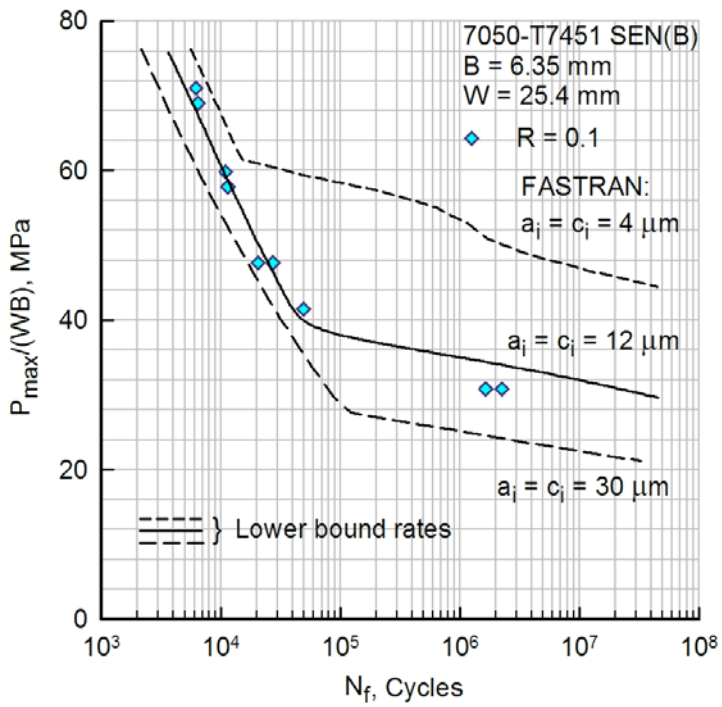

Figure 58. Fatigue Behavior Under CA Loading for Various Initial Discontinuity Sizes Using the Lower-Bound ΔK_{eff}-Rate Curve

5.3.5.2 Spectrum Loading.

A large number of SEN(B) specimens were tested under the Mini-Falstaff+ load sequence (as shown in figure 59). Again, a nominal stress based on the maximum load applied in the spectrum was plotted against the fatigue life, N_f. One test was terminated at 10^7 cycles. Again, the lower-bound curve agreed well with the test data over the complete range of maximum loads tested, whereas the predicted lives from the upper-bound curve were very conservative for all maximum loads tested.

The fatigue tests and life predictions concerning specimens subjected to the Mini-TWIST+ spectrum loading are shown in figures 60 and 61. Results using the full Mini-TWIST+ (level 1) spectrum are shown in figure 60 and show that the lower-bound curve overpredicted the fatigue lives by a factor of 3 using the 12-µm initial flaw. The test data fell between the predicted lives from the lower- and upper-bound curves, whereas the predicted results on Mini-TWIST+ (level 3) spectrum agreed well with the test data. It is suspected that the high loading in the severe flight (level 1) are causing more crack growth delay in the model than level 3 loading. In addition, the rough crack surfaces may promote more crack front meandering around overload plastic zones, while the FASTRAN model was forcing the crack to grow straight through the overload plastic zones (see figure 62). Again, further study is needed to help resolve these issues with severe overloading during variable amplitude loading.

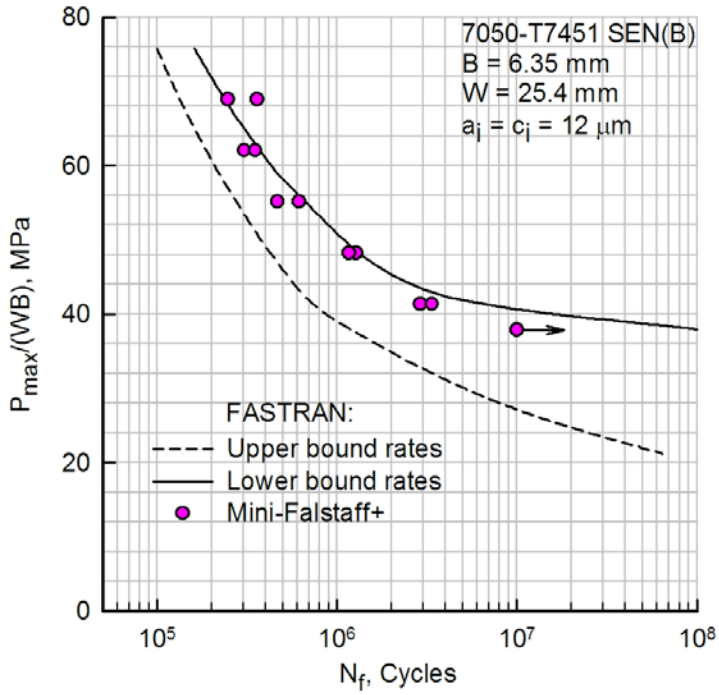

Figure 59. Fatigue Behavior Under Mini-Falstaff+ Loading for the Two ΔK_{eff}-Rate Curves

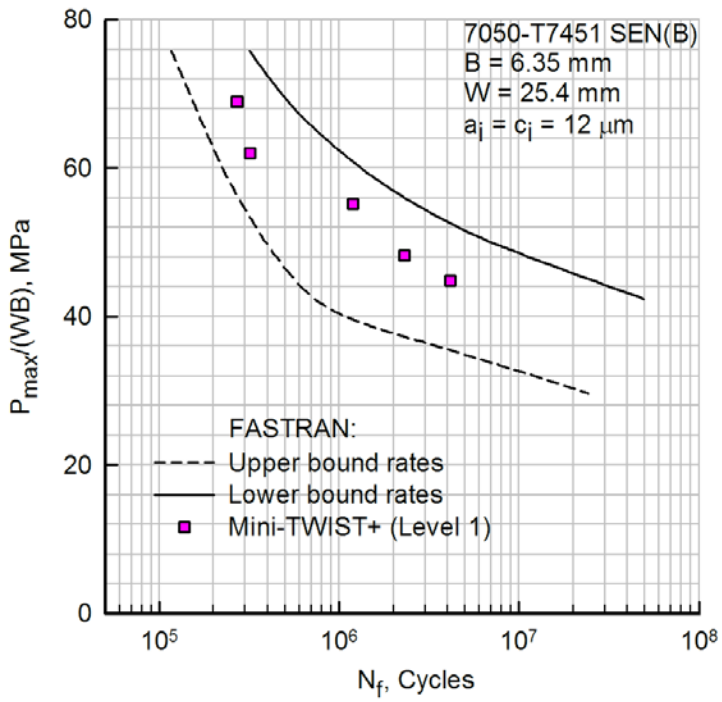

Figure 60. Fatigue Behavior Under Mini-TWIST+ (level 1) Loading for the Two ΔK_{eff}-Rate Curves

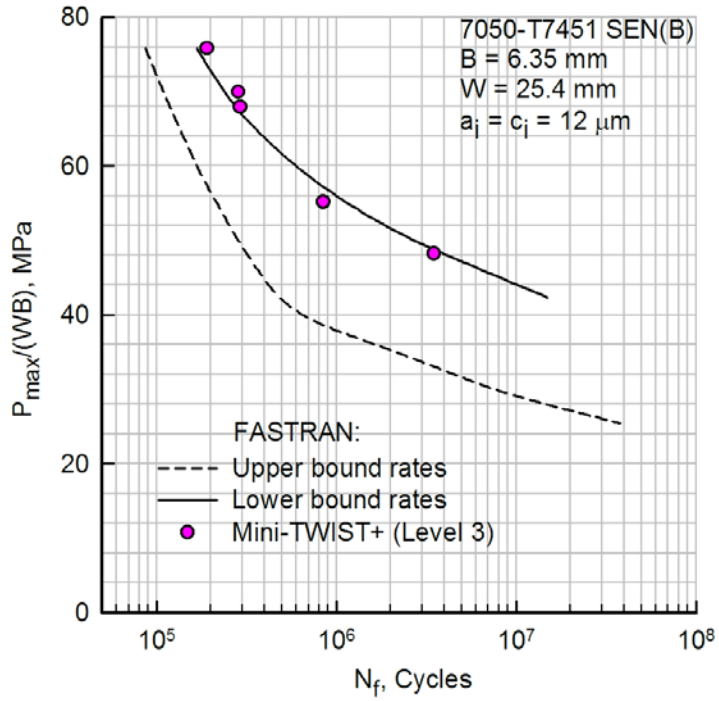

Figure 61. Fatigue Behavior Under Mini-TWIST+ (level 3) Loading for the Two ΔK_{eff}-Rate Curves

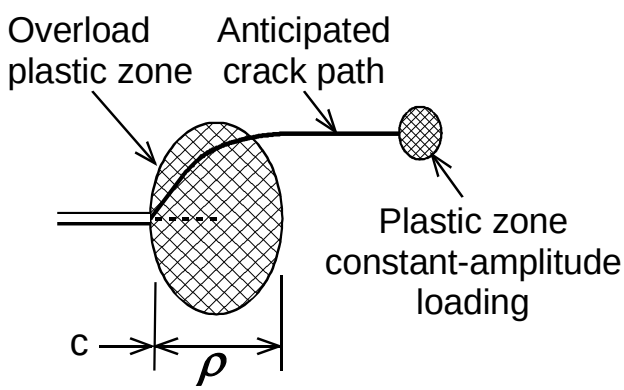

Figure 62. Suspected Crack Path After an Overload During Severe Flight Loading

The crack closure model was designed to grow a crack straight through the overload plastic zone, as shown by the dashed line in figure 62. However, because of the very rough fatigue crack surfaces and slip band formation at the crack front during the overload, the crack may grow around the overload plastic zone (figure 62). Crack path changes were observed by White et al. [102] on the 7050-T7451 alloy for periodic underloads, and Hudson and Hardrath [103] on 2024-T3 after a two-level (2:1 applied stress level) block loading test.

5.4 STEEL 9310.

The Boeing Company provided a large 9310 steel rod to MSU. From the rod, C(T), SEN(B), and tensile specimens were machined in the longitudinal direction of maximum grain flow and heat-treated by procedures described in appendix C.

Large crack tests were conducted on the C(T) specimens to obtain FCG-rate data over a wide range in rates from threshold to near-fracture over a wide range in the load ratios, R. During some of these tests, local strain gages were mounted to one side of the C(T) specimens to measure crack opening loads during high-R and K_{max} tests. The BFS gage, used to monitor crack growth, was also used to determine the crack opening load ratios on low-R (0.1) tests. Here, the OP1 values were used because previous tests at MSU [24-27] had shown fairly good agreement between remote and local gages during low-R tests. These crack opening load ratios were used to establish the effective stress intensity factor range-against-rate relation in the threshold and near-threshold regimes. The FASTRAN model was then used to develop the full range ΔK_{eff}-rate equation of the 9310 steel.

Small crack and fatigue tests were conducted on the SEN(B) specimens under CA loading (R = 0.1) at various maximum applied stress levels. Surface crack depths in the thickness direction were monitored on the notch root surface using a high-magnification traveling microscope. In general, surface cracks were monitored from approximately 150 μm to the plate thickness. FASTRAN was used with small crack theory and the ΔK_{eff}-rate relation to calculate the fatigue behavior on these specimens using an EIFS. Comparisons were made between measured and predicted crack growth along the notch surface and the total fatigue lives under CA loading.

5.4.1 Large Crack Behavior.

FCG tests were conducted on C(T) specimens over a wide range of load ratios (0.1 to 0.95) and constant K_{max} (7.7 to 55 MPa-m$^{1/2}$) test conditions to determine the ΔK-rate data in the threshold and near-threshold regimes. Figure 63 shows the constant R test data and figure 64 shows the constant K_{max} test data. The constant R tests show the normal load ratio shift in the test data with the high-R tests giving a lower ΔK at the same rate and approaching fracture at lower ΔK values. In figure 64, the K_{max} test data also show a shift to lower ΔK values at a given rate at higher magnitudes of K_{max}. Each K_{max} test started at an R value of 0.1, except for the test with the highest K_{max} value, which was at R = 0.8. The test with the lowest K_{max} value resulted in a final R value of 0.68 in the threshold regime and produced test data that agreed well with the R = 0.7 results. Likewise, the highest K_{max} test results agree well with the R = 0.95 test data. In the past, this shift with K_{max} has been attributed to a so-called K_{max} effect. Again, it was of interest to measure the crack opening loads during these tests to see if the K_{max} effects could be explained by crack closure behavior.

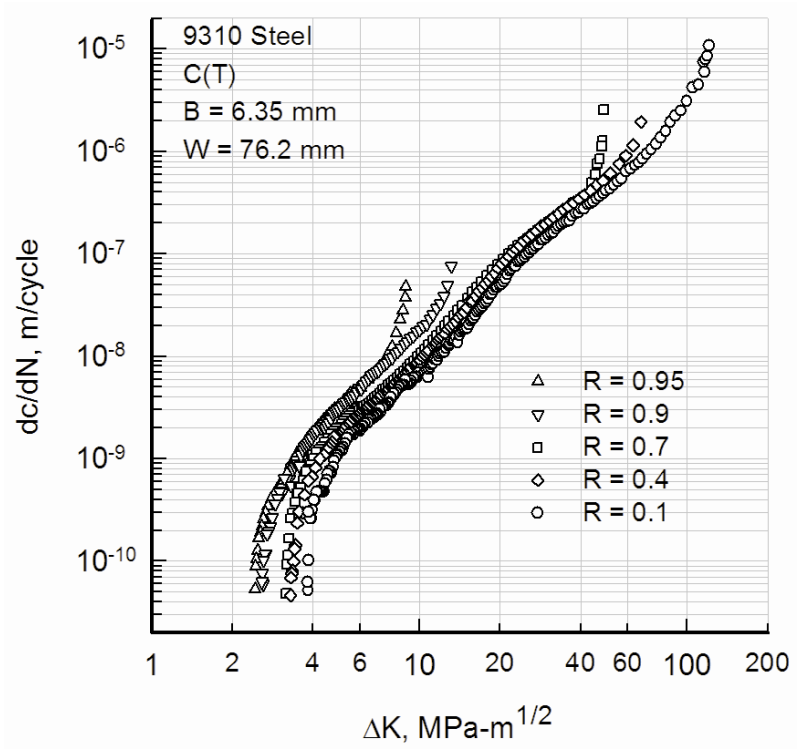

Figure 63. FCG-Rate Data for Constant *R* Tests on 9310 Steel

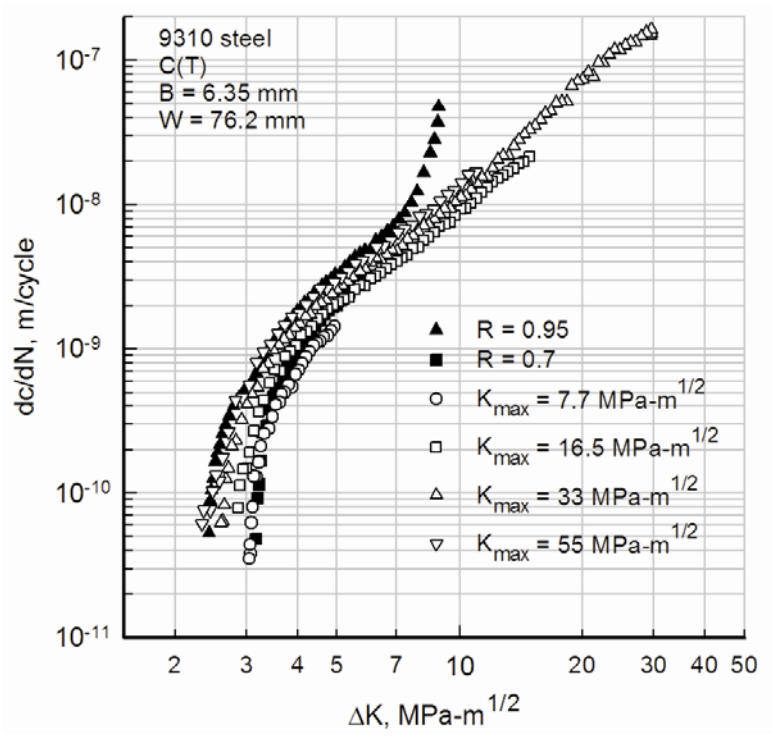

Figure 64. The FCG-Rate Data for Constant K_{max} and High *R* Tests on 9310 Steel

Figure 65 shows a comparison of the present ΔK-rate data with test data from Liu et al. [104] at low- and high-R. Their test specimens were 3.2 mm thick in comparison to 6.35 mm in the present study. The high-R test data agreed fairly well, but the present test data for R = 0.1 loading produced slightly lower ΔK values for a given rate from threshold to the mid-rate regime. They also found no K_{max} effect in tests that covered K_{max} values from 13 to 50 MPa-m$^{1/2}$, whereas the tests in the present study showed a consistent shift to lower ΔK values with higher K_{max} values.

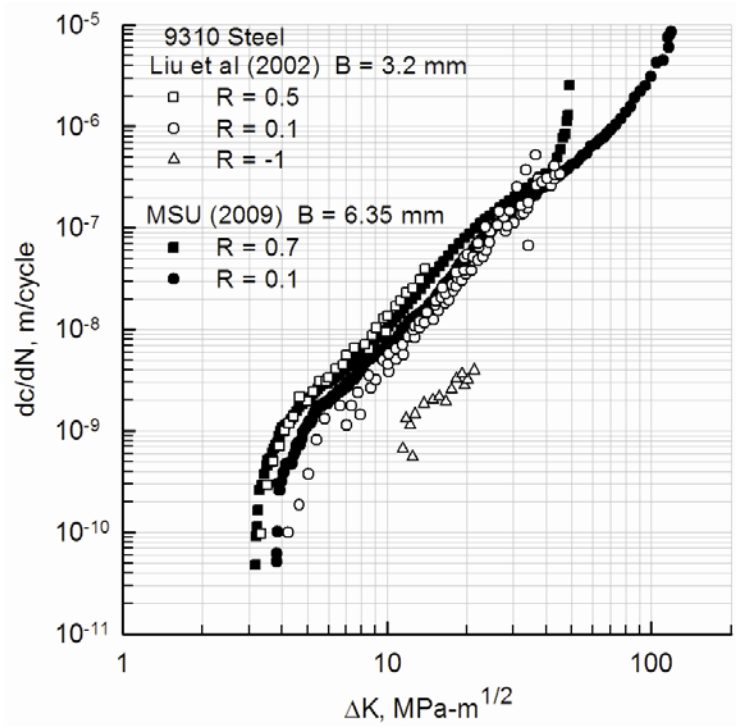

Figure 65. Comparison of Present FCG-Rate Data With Results From the Literature on 9310 Steel

5.4.2 Crack Closure Behavior.

Recently, Yamada and Newman [24-27] measured crack opening loads using local strain gages. The BFS gage was also used as a remote method. The BFS gage had been found to be fairly good for low-R (using OP1 values), but it was inadequate for high-R. To measure load strain records near the crack tip, strain gages were mounted close to the crack path for the specimens tested at a load ratio of 0.7 and K_{max} tests only. The locations of the strain gages were chosen to be slightly off the anticipated crack path by approximately the crack-starter notch height (~2 mm) and approximately 5 mm away from the crack tip after CP (see figure 18). A number of strain gages were mounted along the anticipated crack path to record load strain records as the crack approached each gage. The optimum signals were obtained when the crack tip was about 2 to 3 mm away from the strain gage during threshold testing. Approximately 20 load strain records were recorded when the target FCG rates were achieved. During measurements, the frequency of cyclic loadings was reduced to 0.5 Hz to minimize external noise. Some typical load-reduced strain records during an R = 0.7 and a K_{max} threshold test are shown in figures 66 and 67, respectively.

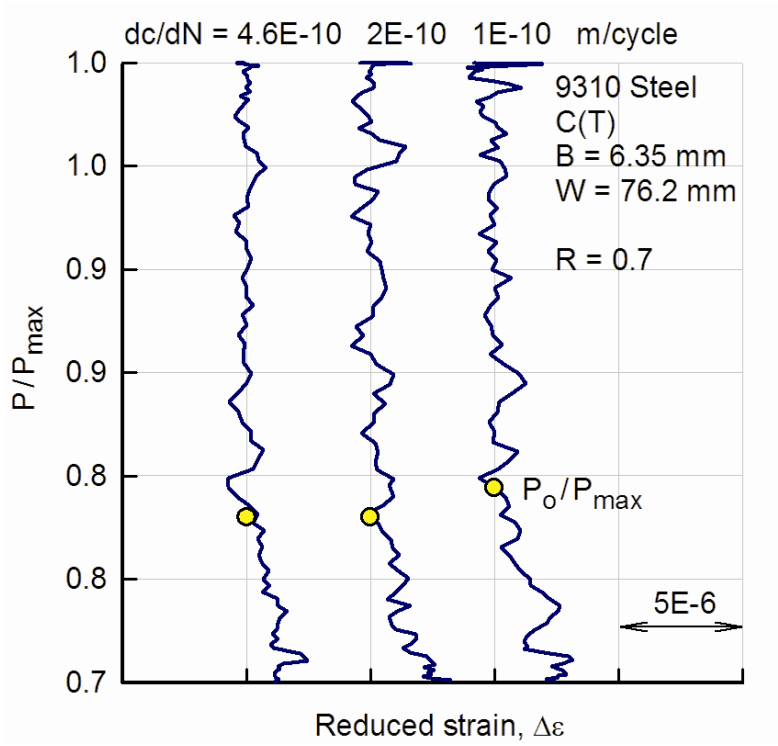

Figure 66. Determination of Crack Opening Load Ratios for R = 0.7 CPLR Threshold Test

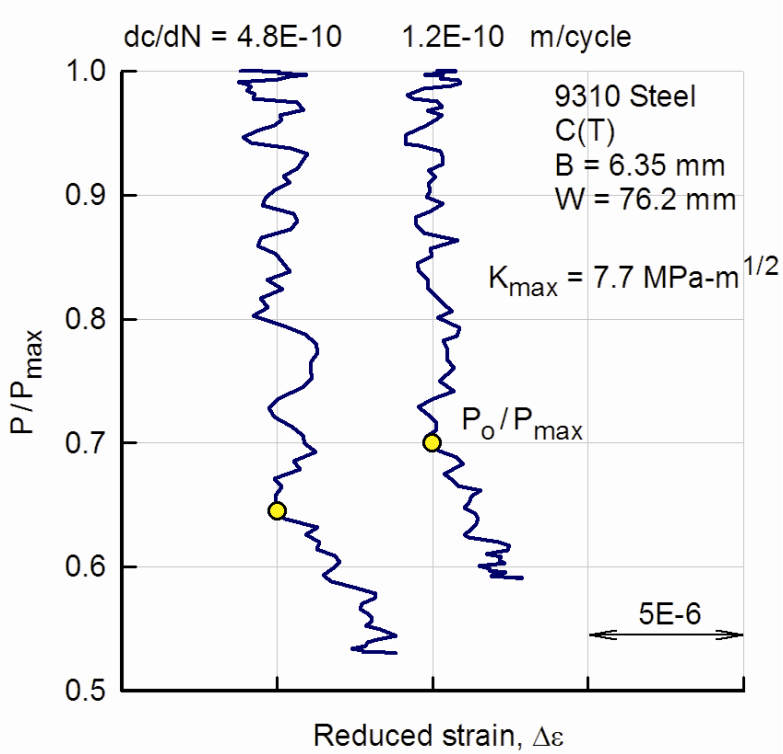

Figure 67. Determination of Crack Opening Load Ratios for Constant K_{max} Threshold Test

Figures 66 and 67 show the normalized load (P/Pmax) plotted against reduced strain ($\Delta\varepsilon$). The method used to generate the load-against-reduced-strain results from a load strain record is described in appendix A. In measuring load-against-local-strain records during cyclic loading, it is important to minimize electronic noise, vibrations, and any other nonlinearities not associated with crack closure, such as out-of-plane bending. Beveling the pinholes in the C(T) specimens was found to eliminate out-of-plane bending associated with the clevis pin contacting the outer edges of the pinholes. This procedure was initially used to produce straight crack fronts during threshold tests. The results shown in figures 66 and 67 have more noise than normal, but the plots clearly show an indication of crack closure. However, further study is needed to improve the quality of the load strain signals on the 9310 steel. In general, the steel specimens show a smaller crack closure tail swing near the minimum load than the aluminum alloys.

5.4.3 Crack Closure Analysis.

Figure 68 shows a crack closure analysis of the FCG-rate data to determine the effective stress intensity factor range-against-rate data. This figure shows the lowest and highest K_{max} test results and the low- and high-R test data in the threshold and near-threshold regimes. The BFS gage was used to determine the OP1 crack-opening load ratios for the R = 0.1 ASTM LR test. The ΔK_{eff} results for the R = 0.1 test are shown as the solid curve that falls within or near the ΔK_{eff} scatter band. The crack opening load ratios for the lowest K_{max} test (figure 67) resulted in ΔK_{eff} values (dashed curve in figure 68) that also fell within the scatter band. The ΔK-rate data for the highest K_{max} test fell very near to the scatter band, indicating that the crack surfaces may have been fully open. In addition, the crack opening load ratios for the R = 0.7 test produced ΔK_{eff} results (solid square symbols) that also fell within the scatter band.

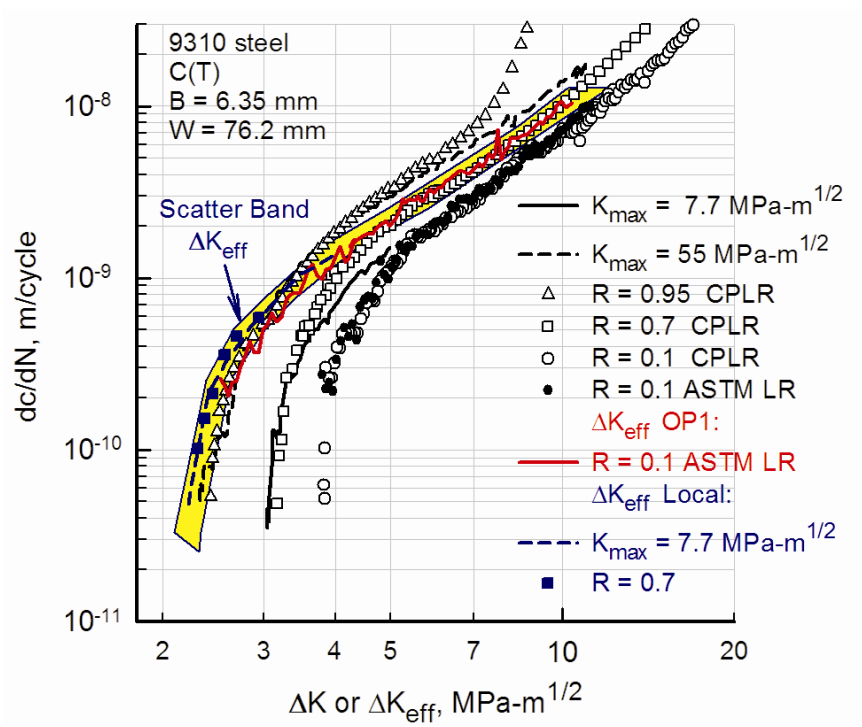

Figure 68. Effective Stress Intensity Factor Range-Against-Rate for Various Threshold Tests

In the threshold regime, a unique ΔK_{eff}-rate relation was found for low-R, high-R, and the K_{max} tests. Therefore, the so-called K_{max} effects were due to crack-closure behavior. The reason for crack closure at high-load ratios was unclear, but may have been due to a debris-induced shielding mechanism because the fatigue crack surfaces were very flat. Plasticity effects alone are not expected to cause high-R closure, but the crack opening load at high-R is the minimum load from models like FASTRAN, so a small amount of debris (or roughness) may cause high-R closure.

In the mid-rate regime, the R = 0.7 test data appears to form the ΔK_{eff}-rate curve, as expected. The very high-R (0.95) test results show a K_{max} effect as the crack grows to failure. The asymptotic stress intensity factor range at fracture (ΔK_c) was estimated to be about 9 MPa-m$^{1/2}$, which would suggest an elastic fracture toughness of 180 MPa-m$^{1/2}$. Fracture toughness calculations on the 9310 steel will be discussed later in this report.

The plasticity-induced crack closure model, FASTRAN [16 and 94], was used to correlate the FCG data over a wide range in stress ratios and rates from threshold to near-fracture to generate the full range ΔK_{eff}-rate curve (see figure 69). From previous studies on 4340 steel [19], a high-constraint factor (α) was used for FCG rates less than 1e-07 m/cycle and a low-constraint factor was used for rates greater than 1e-05 m/cycle. The constraint loss regime has been associated with the transition from flat to slant crack growth [72]. The vertical, dashed line shows the results of an equation, $(\Delta K_{eff})_T = 0.5\ \sigma_o\ \sqrt{B}$, to predict the transition from flat to slant crack growth. The solid lines with open symbols in figure 69 show the selected ΔK_{eff}-rate curve for the 9310 steel (referenced in table 10). In the low-rate regime, the ΔK_{eff} curve was selected to fit the results from the local crack opening load measurements (figure 68), while the upper region was selected to match the low-R results. Beyond a ΔK_{eff} value of 50 MPa-m$^{1/2}$, the ΔK_{eff}-rate relation was estimated as a linear extrapolation. Note that larger width FCG specimens would have generated more appropriate results at the higher ΔK_{eff} values. These larger width specimens would have fractured at a large value of ΔK.

In the low-rate regime, the crack closure model was unable to correlate the near-threshold data for various load ratios into a narrow band. The FCG data exhibited fanning with the load ratio, presumably due to a debris-induced shielding mechanism. Thus, the threshold term in equation 6 was used to fit these data. The coefficients in the threshold term, $[1 - (\Delta K_o/\Delta K_{eff})^p]$, were evaluated by first determining the effective stress intensity factor range threshold, ΔK_o, as a function of R from the results shown in figure 69. The ΔK_o value for a given R is the limiting asymptotic value as the rate goes to zero and is not defined at a rate of 1E-10 m/cycle as specified in ASTM E-647 (see figure 70). The functional form selected is a power law equation, like that proposed by Klesnil and Lukas [90], except that the effective stress intensity factor range is used instead of linear elastic values. The fit-to-threshold data are shown by the solid curve. The power term, p = 5 in equation 6, was selected to best match the shape of the ΔK-rate curves as threshold conditions were approached.

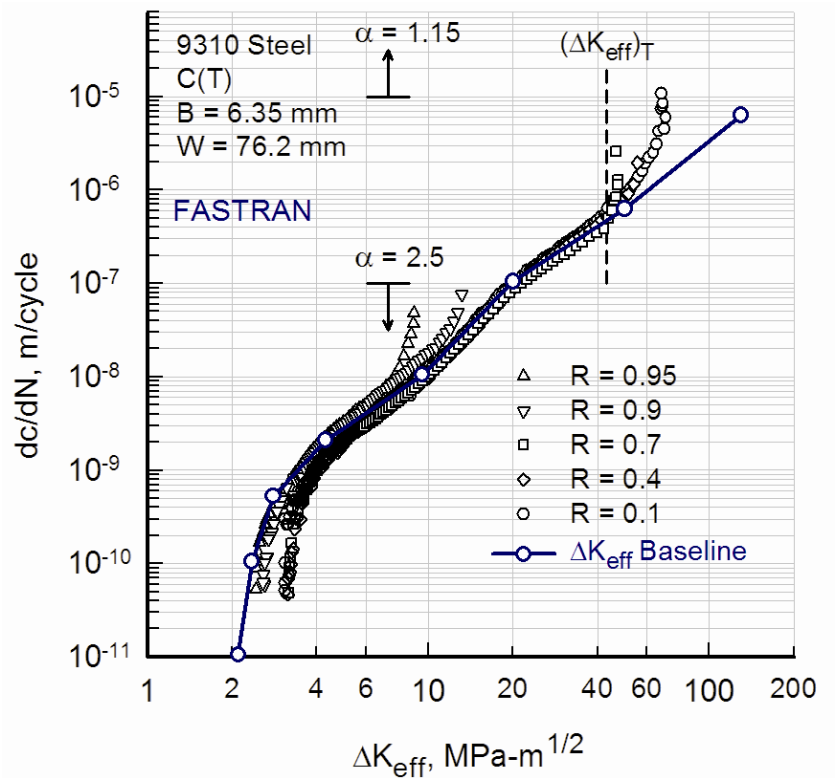

Figure 69. Effective Stress Intensity Factor Range-Against-Rate for 9310 Steel

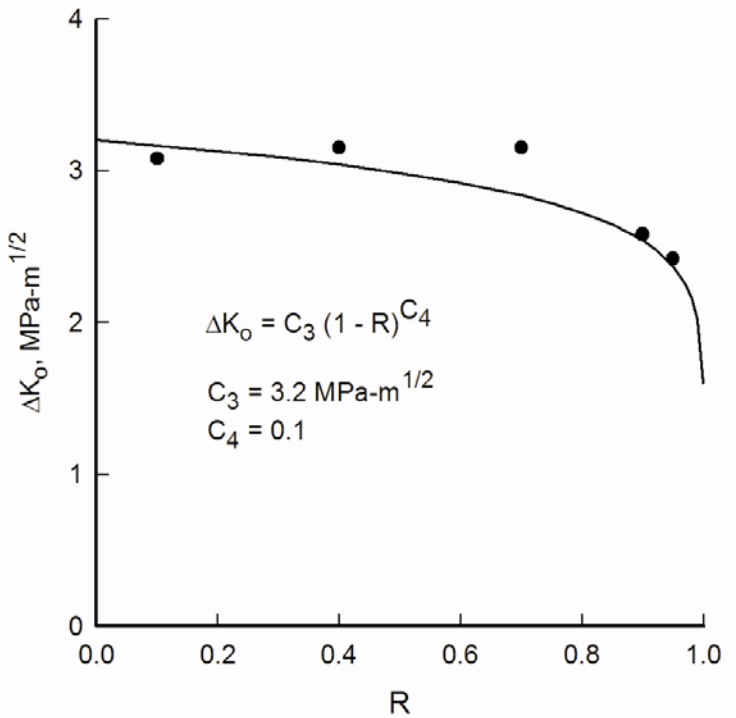

Figure 70. Effective Stress Intensity Factor Range at Threshold as a Function of Load Ratio

Table 10. Effective Stress Intensity Factor Range-Against-Rate Relation for 9310 Steel (B = 6.35 mm)

ΔK_{eff}, MPa√m	dc/dN, m/cycle
1.5	1.0e-11
2.0	1.0e-10
2.7	5.0e-10
4.3	2.0e-09
9.5	1.0e-08
20.0	1.0e-07
50.0	6.0e-07
130.0	6.0e-06
α = 2.5	$\leq$ 1.0e-07
α = 1.15	$\geq$ 1.0e-05
C_3 = 3.2 MPa-m$^{1/2}$	C_4 = 0.1 and p = 5
C_5 = 150 MPa-m$^{1/2}$	q = 8

To evaluate the coefficients in the fracture term, $[1 - (K_{max}/C_5)^q]$, in equation 6, the cyclic fracture toughness (C_5) must be determined. Normally, C_5 is equal to the elastic fracture toughness, K_{Ie}, which is usually a function of crack length, width, and crack configuration. The elastic stress intensity factor at failure using the initial crack length and maximum failure load is K_{Ie}. However, linear elastic fracture mechanics parameters, such as K, do not work very well for fracture. Nonlinear fracture mechanics concepts, such as J-integral or CTOD, are required to correlate and predict the effects of crack length, width, and crack configuration on fracture. However, the TPFC [74 and 75] has been able to correlate and predict the effects of crack length, width, and, in some cases, crack configuration on fracture.

The fracture toughness, K_{Ie}, was estimated from the FCG results approaching fracture in figure 63 and these results are shown as solid circular symbols in figure 71. For comparison, some previous results on 4340 steel are also shown. The 4340 steel C(T) specimens were 51-mm wide, while the 9310 C(T) specimens were 76.2-mm wide. Some estimates for the two-fracture parameter, K_f and m, were made. The solid curves show calculated K_{Ie} against initial crack length-to-width (c_i/W) ratio for the 9310 steel. These results show that smaller width C(T) specimens would fail at lower values of K_{Ie}, whereas larger width specimens would fail at higher K_{Ie} values for the same crack length-to-width ratio. The results for the very deep cracks (c_i/W>0.85) may be experiencing a rise in constraint under fully plastic conditions, which may be the reason for the elevated K_{Ie} values.

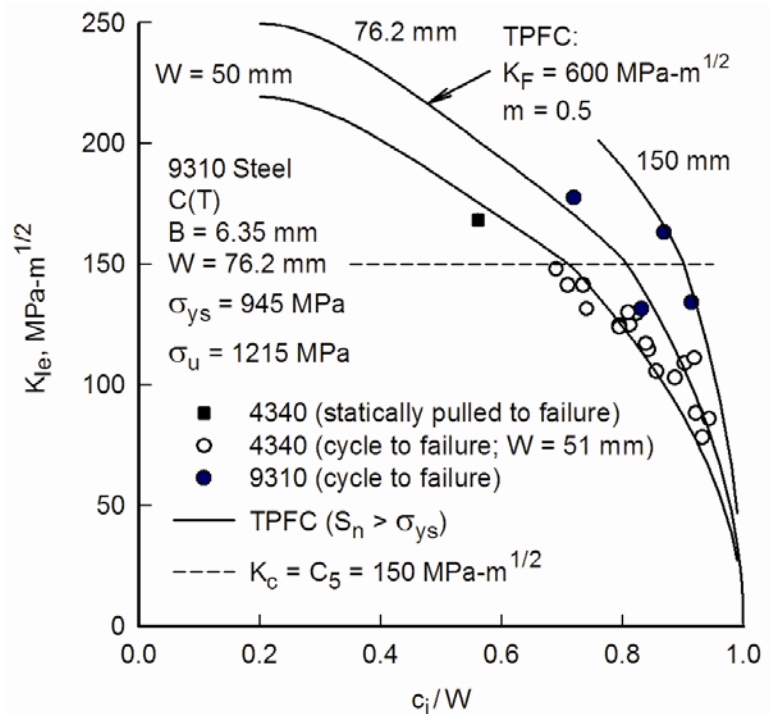

Figure 71. Elastic Fracture Toughness on C(T) Specimens as a Function of Crack Length-to-Width Ratio

Because insufficient test data were available to conduct a proper TPFC analysis, the cyclic fracture toughness, C_5, was estimated at 150 MPa√m, as shown by the dashed line in figure 71. The power term, q = 8 in equation 6, was selected to best match the shape of the ΔK-rate curves as fracture conditions were approached (see section 5.4.4).

A comparison between measured and predicted FCG-rate behavior from the crack-closure model at various load ratios (R) is shown in figure 72. The ΔK_{eff}-rate baseline curve shown in figure 69 was used to predict the ΔK-rate curves for R varying from 0.1 to 0.95, using equation 6 with the parameters given in table 10. The solid curves show the predicted curves for various R values that fit the threshold and fracture regions quite well.

5.4.4 Small Crack Behavior.

Small crack tests were performed on the SEN(B) specimens and servohydraulic test frames. The pin holes in all of the steel specimens were manually beveled as a way to reduce out-of-plane bending. Specimens had been electrochemically polished in an attempt to relieve residual stresses introduced during the machining process (see figure 16). Unfortunately, as a result of the electrochemical polishing, some specimens became discolored and streaked; however, the notches themselves showed no marks or streaks as a result of the polishing. The tests were monitored optically and were stopped at regular intervals for inspection. All small crack tests were CA tests performed at a load ratio of R = 0.1. The test ended when the specimen fractured into two separate pieces. Tests were performed at a frequency, ranging between 10 and 18 Hz (higher stress level tests were performed at a lower frequency).

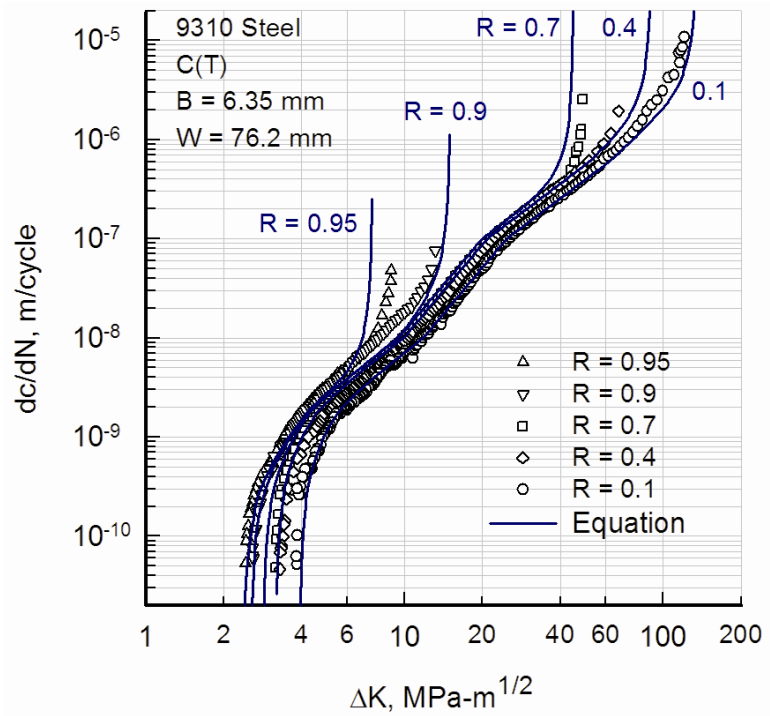

Figure 72. Comparison of FCG-Rate Equation and Test Data on 9310 Steel

The definition of small crack is often a topic of discussion among fatigue professionals. However, most agree that small cracks are about the size of inclusion particle clusters or grains for a given material. These cracks are very small and are often measured using a replica method; the test is stopped at regular intervals and a replica is made of the notch surface. These replicas can then be inspected through a scanning electron microscope and the imprints of cracks can be measured. The replica compounds that are available for this type of data gathering are expensive, difficult to use, and time-consuming; also, the compounds typically have a shelf life of only a few weeks. For this work, however, it was decided that the replica method would not be used because of time constraints and cost. Instead, the tests were stopped at regular intervals and the notch surface was inspected using a traveling microscope. As a result, the data collected during these tests did not include measured crack sizes that could be called small. However, because the cracks were naturally initiated, the test results do reflect the overall fatigue behavior of the notched specimens.

Some of the SEN(B) tests were stopped at regular intervals and the notch was inspected under mean load for any cracks that may have initiated along the notch surface. When found, these cracks were monitored and their surface crack depths (2a) were measured. These results are shown in figure 73 for five different applied stress levels, $S_{max} = P_{max}/(WB)$. The total crack depth was normalized by the plate thickness (B).

In the past, the FASTRAN strip-yield model has been able to predict or calculate the fatigue life of notched and unnotched specimens using EIFS that were sometimes related to the material microstructure, such as inclusion particle sizes. However, it was of interest to know if the FASTRAN model could accurately simulate crack depth-against-cycles for small cracks.

FASTRAN was then used to model the growth of a crack starting from a 6-μm semicircular surface crack at the center of the notch root under CA loading for the five applied stress levels (curves). The FASTRAN simulation most accurately modeled the crack growth behavior for the highest applied stress (S_{max} = 124 MPa). For other applied stress levels, the simulation modeled crack growth behavior well, with the lowest stress test (S_{max} = 83 MPa) having the greatest error (about 40%) in life.

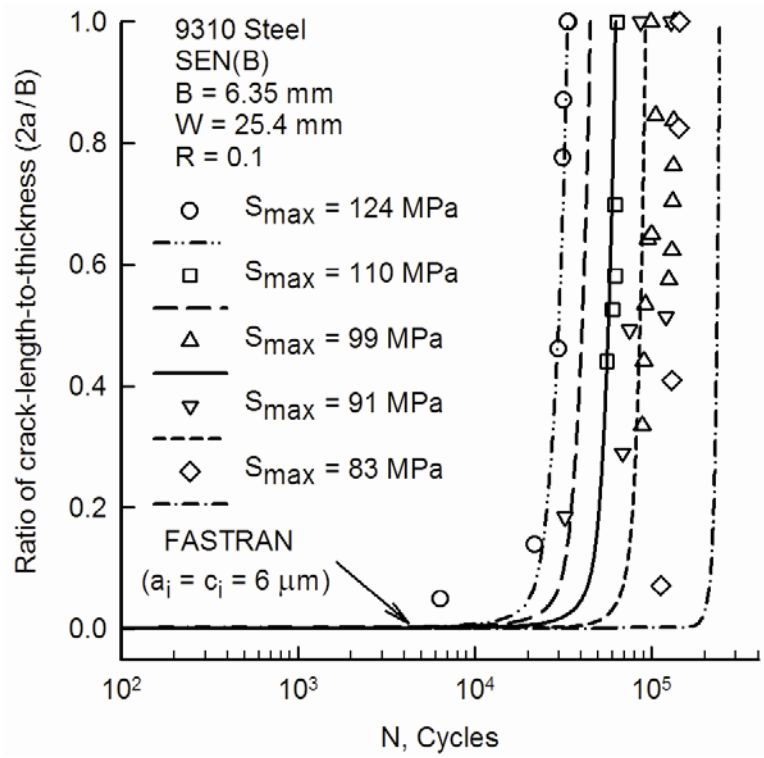

Figure 73. Comparison of Measured and Calculated Crack Length-Against-Cycles During Fatigue Tests on SEN(B) Specimens

5.4.5 Fatigue Behavior.

The SEN(B) specimen was designed to be a small crack and fatigue specimen that could be loaded with pin clevis fixtures. For the 9310 steel, fatigue tests were conducted on SEN(B) specimens under CA loading at a load ratio of 0.1. The results (solid circular symbols) are shown in figure 74 as the maximum notch root stress, σ_{max}, plotted against cycles-to-failure, N_f. The stress concentration factor (K_t) based on a nominal stress, $P_{max}/(WB)$, was 11.8.

Liu et al. [104] conducted fatigue tests on a similar 9310 steel with the AGARD small crack test specimen [21-23] that is a SEN(T) specimen. These tests were conducted at R = 0.1 loading at a frequency of 15 Hz, as shown by the open square symbols in figure 74. The SEN(T) specimens had an elastic stress concentration factor (K_t) of 3.19. The SEN(T) and SEN(B) fatigue lives compared very well at the low applied stress levels, but some differences were observed at the higher applied stress levels.

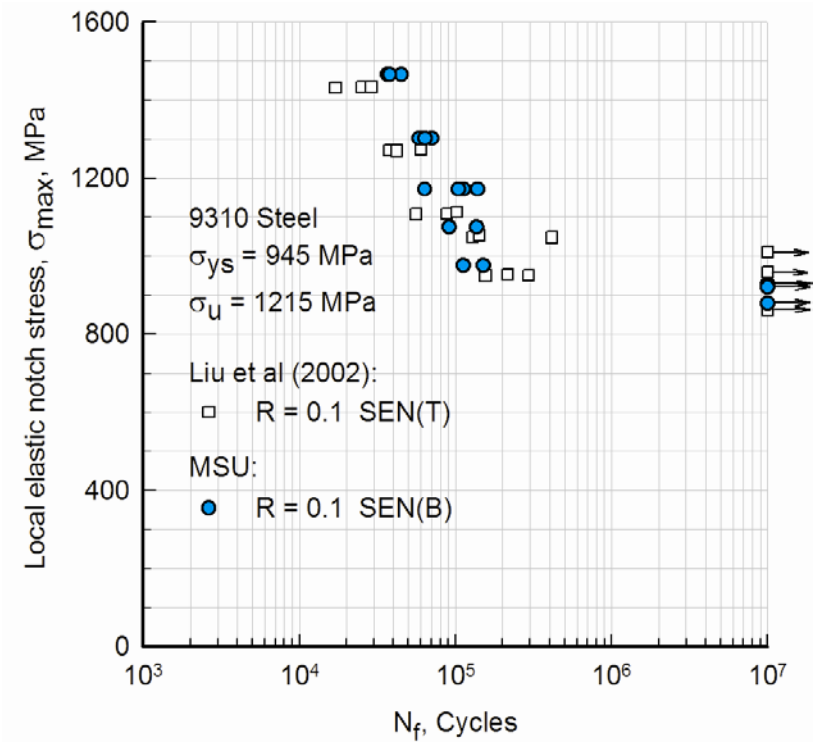

Figure 74. Comparison of Fatigue Data From Current Testing on SEN(B) Specimens and SEN(T) Specimens From the Literature

Fatigue life predictions were made with the crack closure model, FASTRAN [16], for the CA fatigue tests using small crack theory and the baseline ΔK_{eff}-rate curve. By trial and error, the initial discontinuity was found to be a semicircular surface crack or void ($a_i = c_i = 6$ μm; h_n = void height = 3 μm) located at the center of the edge notch. This was the same EIFS used in reference 104. The crack depth, *a*, is measured in the thickness direction and the crack length, *c*, is measured in the width direction. Two- and three-dimensional stress intensity factor solutions were developed for the SEN(B) specimen and incorporated into the FASTRAN code [101]. The calculated fatigue lives agree very well with most of the test results, but they did not fit the endurance limit very well. The 9310 steel is a very clean alloy and no metallurgical features could be identified with the 6-μm flaw.

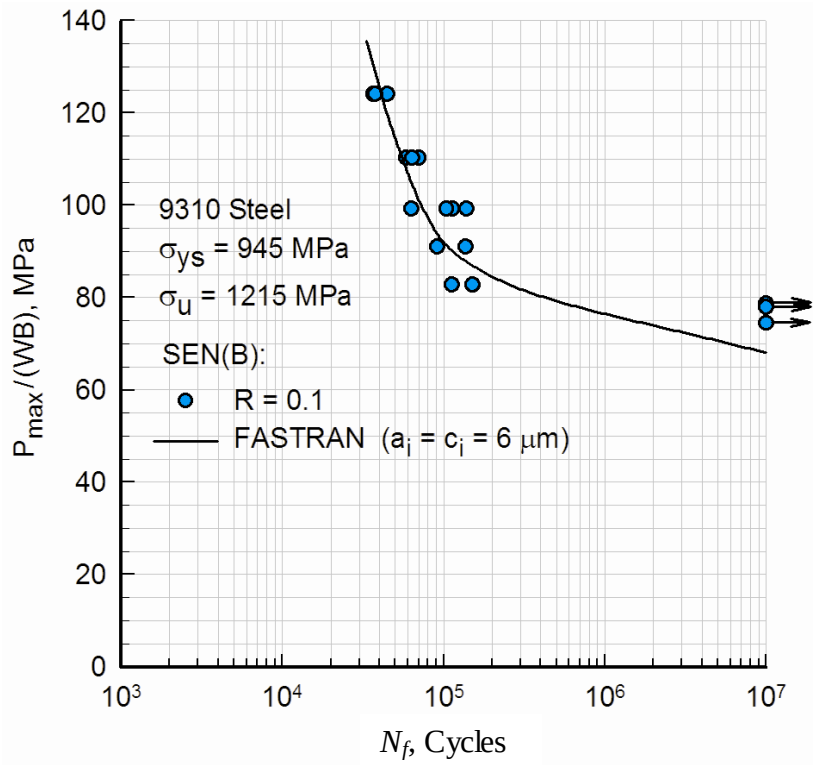

Figure 75. Comparison of Measured and Calculated Fatigue Lives on SEN(B) Specimens

6. ROTORCRAFT STRUCTURAL COMPONENT.

A decade ago, the helicopter community [105 and 106] developed a round robin challenge problem to benchmark the ability of the industry to predict FCG life in a simulated helicopter component under spectrum loading to support the use of the damage-tolerance approach. The component was made of a 7000-series aluminum alloy and is shown in figure 76(a). The three-dimensional crack configuration (corner crack at a reinforced lightening hole) and the initial corner crack size (2-mm radius) are shown in figure 76(b). The FCG-rate data on the aluminum alloy and the stress intensity factor solution were provided to a number of participants. Although the crack configuration was three-dimensional, all analyses in the round robin (required) and in the present research were treated as two-dimensional crack problems using the average stress intensity factor around the crack front. The round robin test results were unknown to most of the participants. Approximately 60% of the predicted lives were within a factor of two of the test life. However, there were two issues that merited further study [107]: first, the predicted shape of the crack length-against-cycles curves did not correctly match that of the test data in any of the predictions; and second, there was a large spread of predicted lives with a difference of up to a factor of 50 between the shortest and longest predicted lives. Some calculated inspection intervals were longer than the entire experimental life. All of the predictions were unconservative in the early stages of crack growth, which could have serious ramifications for the selection of inspection intervals.

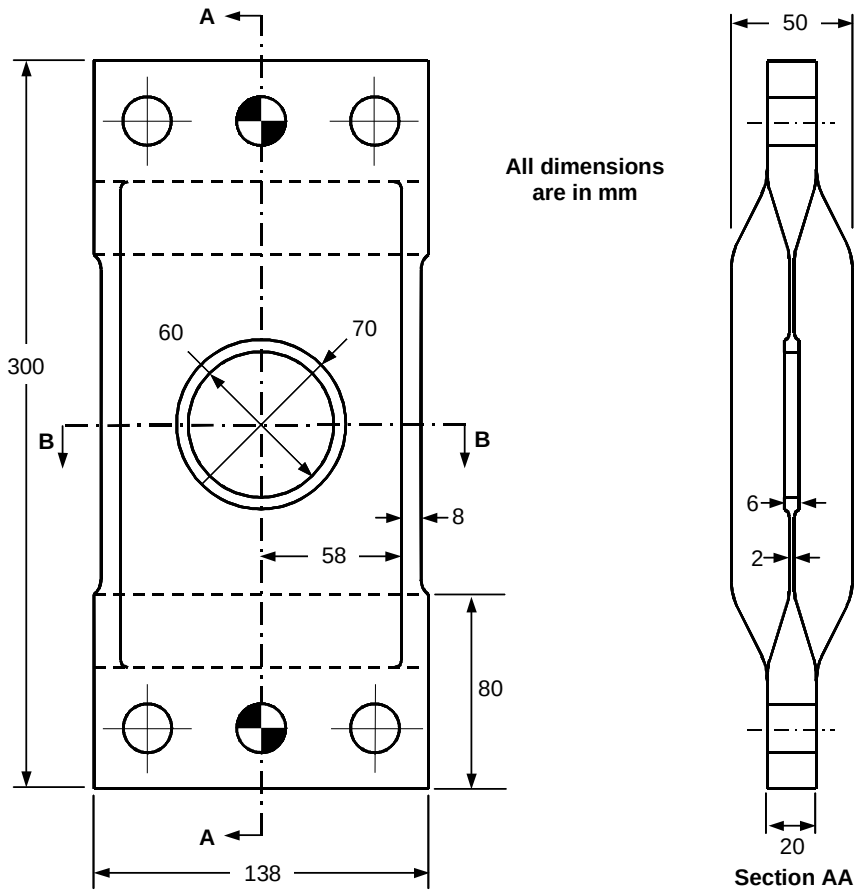

(a)

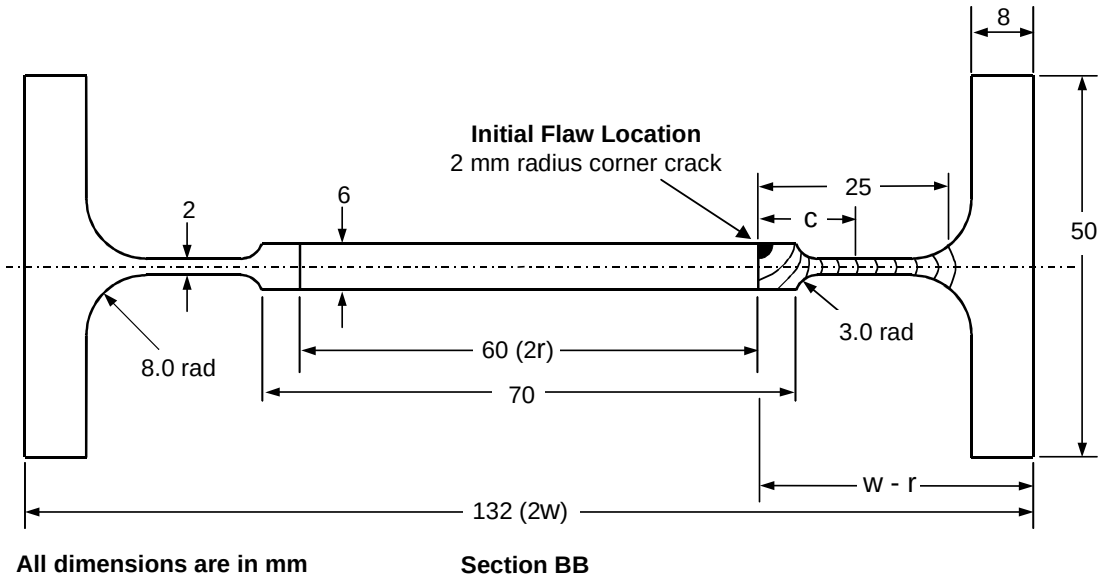

(b)

Figure 76. (a) Complex Rotorcraft Component Used in the Round Robin Challenge Problem and (b) Crack Configuration in the Complex Rotorcraft Component

Recently, Gregory Glinka (University of Waterloo, Canada, unpublished) developed another stress intensity factor (*K*) solution for three-dimensional cracks in the complex rotorcraft component. It was of interest to evaluate the new *K*-solution and its influence on FCG predictions because this was one of the major issues on the round-robin challenge problem.

As in the original analyses of the round-robin problem [107], the plasticity-induced crack closure model, FASTRAN [16], was used to predict FCG in the simulated rotorcraft component using the various stress intensity factor solutions. The model was based on a strip-yield model concept, but modified to leave plastically deformed material in the wake of the advancing crack. The model includes the influence of constraint (plane stress or plane strain behavior) on the development of plasticity and crack closure. The model was used to correlate FCG-rate data from C(T) specimens under CA loading over a wide range in load ratios and FCG rates. However, FCG-rate data in the low-rate regime generated using the ASTM LR test method [3] for low-load ratios were not used because the test method has been shown to produce improper data in the low-rate regime [14, 17, 19, 24-27, and 46-50]. In addition, another unresolved issue is the thickness of the material used in the FCG tests (B = 17.5-mm) and the component (corner crack in 6-mm-thick material at the edge of the hole to a through crack in 2-mm-thick material in the reduced section). Test results under CA loading and past experience with a wide variety of materials and thicknesses were used to help establish the constraint factor used in the model. The model was then used to predict crack growth under the standard Asterix [108] spectra applied to the complex crack configuration. Comparisons can be made between measured and predicted crack length-against-cycles results using the various stress intensity factor solutions.

6.1 MATERIAL.

The material was 7010-T73651 aluminum alloy, which is extensively characterized in reference 109. The yield stress and ultimate tensile strength for the aluminum alloy were 434 and 510 MPa, respectively. The FCG-rate data on the aluminum alloy were determined from C(T) specimens using the electrical potential technique under CA loading. These data were obtained on specimens 17.5-mm thick (B) and 70 mm wide (W). Tests were conducted at four stress ratios (R = 0.1, 0.4, 0.7, and 0.9) over a wide range in FCG rates.

6.2 THE CA LOADING.

C(T) specimens made from the aluminum alloy [109] were subjected to fatigue cycling at various stress ratios and these data, ΔK against dc/dN, are shown in figure 77. Because these data were for a thicker material than the round robin crack configuration, additional data from NASGRO [1] for 5-mm-thick material are also shown. Results from the two thicknesses overlay quite well. However, test results for the thinner 2-mm-thick material were not available.

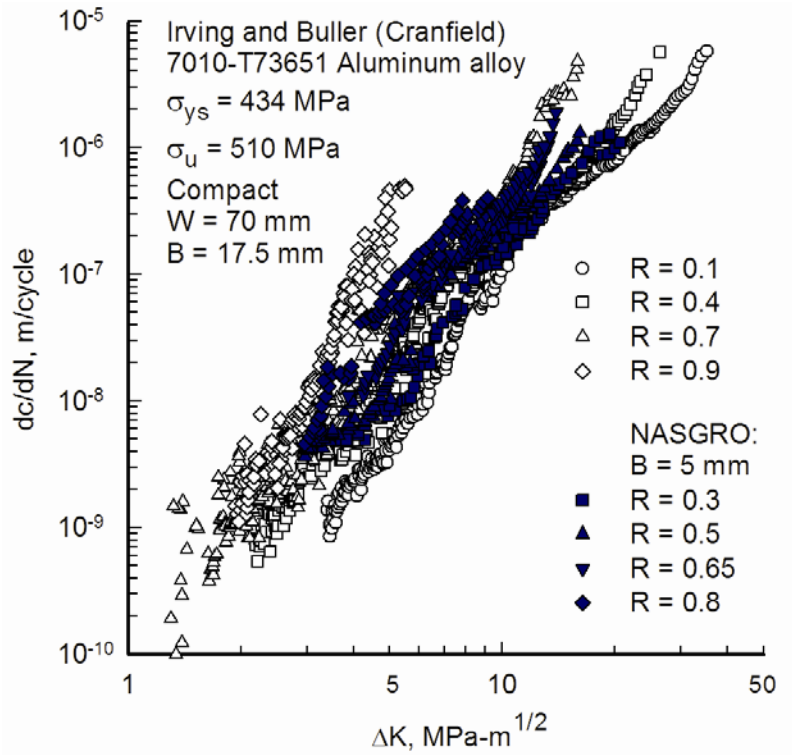

Figure 77. Stress Intensity Factor Range-Against-Rate for 7010-T73651 Aluminum Alloy

6.3 EFFECTIVE STRESS INTENSITY FACTOR-AGAINST-RATE RELATION.

The FCG-rate data from Irving and Buller [109] on the aluminum alloy were analyzed to determine the ΔK_{eff}-rate relation to make crack growth predictions on the round robin problem. Because the specimens were thick (17.5 mm), nearly plane strain conditions (α = 2.5) were found to give a reasonable correlation of the data. Figure 78 shows the ΔK_{eff}-rate data for all of the high-R results (R = 0.7 and 0.9), but some of the R = 0.1 and 0.4 data has been eliminated at lower rates. For the aluminum alloys, it has been shown that the LR procedure [3] may cause higher thresholds and lower rates in the threshold and near-threshold regimes due to remote closure, which is not accounted for in the steady state equations [94]. Because high-R data in the mid-region is fully open ($\Delta K = \Delta K_{eff}$), the R = 0.7 data are generally used to establish the ΔK_{eff} against rate curve. Recently, Yamada and Newman [24-27] showed that high-R crack closure effects occur in the threshold regime by using local strain gages to measure crack opening loads. High-R closure is suspected to be due to a combination of plasticity-, roughness-, and debris-induced crack closure effects. However, correcting for high-R closure in the low-rate regime is beyond the scope of the present analyses because these measurements were not available. Thus, the ΔK_{eff}-rate curve was fit to the R = 0.7 data in the low- and mid-rate regimes, but fit to the low-R data in the upper region. The curve with open symbols shows the ΔK_{eff}-rate curve table lookup values for FASTRAN (see table 11).

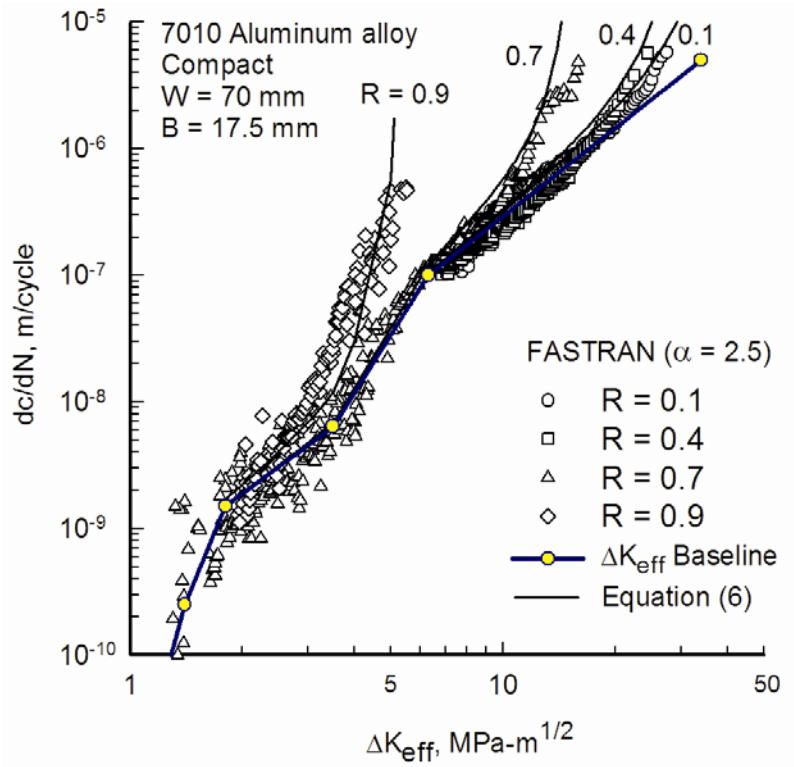

Figure 78. Stress Intensity Factor Range-Against-Rate for 7010-T73651 Aluminum Alloy Neglecting Low *R* Threshold Data

The solid curves in figure 78 show the calculated results from equation 6 with the table lookup ΔK_{eff}-rate curve, C_5 = 52 MPa-m$^{1/2}$ and q = 2, which modeled the approach to fracture reasonably well. The value of C_5 is generally higher than K_{Ic}, the plane strain fracture toughness. The threshold behavior was modeled with the multilinear table and ΔK_o was zero in equation 6.

Table 11. Effective Stress Intensity Factor Range-Against-Rate Relation for 7010-T73651(B = 17.5 mm) Aluminum Alloy

ΔK_{eff}, MPa√m	dc/dN, m/cycle
1.1	1.8e-11
1.4	2.5e-10
1.8	1.5e-9
3.5	6.4e-9
6.3	1.0e-7
34.0	5.0e-6
α = 2.5	All rates
ΔK_o = 0 MPa√m	p = 1
C_5 = 52 MPa√m	q = 2

6.4 STRESS INTENSITY FACTOR SOLUTION FOR ROTORCRAFT COMPONENT.

The helicopter round robin challenge problem was a corner defect (2 mm in radius) at the edge of a large central reinforced hole in a flanged plate made of the 7010 alloy and the component was subjected to the Asterix spectrum loading. The corner flaw was located in a 6-mm-thick part and grew into a thin section (2-mm-thick) after about 5 mm of crack growth. The crack grew into an 8-mm-thick flange (perpendicular to the crack direction) after about 28 mm of growth. Although the initial crack configuration was a corner crack, a ground rule for the round robin was to consider the crack as a two-dimensional crack problem. Participants were supplied with the stress intensity factor solution, as shown in figure 79 (solid curve). The plot shows the boundary correction factor, F, as a function of the normalized crack length, $c/(w-r)$. This figure also shows a schematic of one-half of the configuration with an initial corner crack. In the round robin analysis [106], it was found that the experimental crack length-against-cycles data were faster in the early stages of growth than any of the predictions, suggesting that the supplied stress intensity factors were too low in this region and/or the FCG-rate data fits in the near-threshold regime were causing lower rates than the tests.

Three-dimensional calculations were made for the round robin problem using the BEASY code [110]. BEASY is a boundary element code that can be used to calculate stress intensity factors for three-dimensional crack configurations. In the current study, it was decided to use the average stress intensity factor from the BEASY analysis, and these results are shown as the dashed curve in figure 79. A major difference was observed in the 2-mm- to 4-mm-crack-size range. Because of this difference, a request was made to generate a solution for a 1-mm corner crack and the stress concentration factor at the edge of the hole (without a crack). The stress intensity boundary correction factor for the 1-mm crack was slightly higher than the 2-mm-crack size, indicating that the solution was approaching the limiting solution for a small crack at the edge of the hole. Using the stress concentration factor (2.546) based on the net section stress,

which is the normalizing stress in the *K* equation, the limiting value was calculated from Tada et al. [55] and Newman and Raju [111]. These results are shown in figure 79 as solid symbols on the *y*-axis of the figure. Thus, it can be concluded that the *K* solution from BEASY is most likely the correct solution to the round-robin crack configuration for the early part of the crack growth process.

Recently, Glinka (University of Waterloo, Canada, unpublished) developed a new stress intensity factor (*K*) solution for three-dimensional cracks in the complex rotorcraft component. These results are shown in figure 79 as the solid curve with symbols.

6.5 SIMULATED HELICOPTER LOADING.

The Asterix stress sequence used in this study was derived from strain data measured on a helicopter lift frame. The maximum and minimum normalized stress points in the spectrum were given as 100 and -4, respectively. The normal distribution for the stress ratios [108] indicates that the stress ratio of 0.8 dominates the stress spectrum, which is an extremely high stress ratio spectrum with some negative stress ratio excursions, as shown in figure 80. The Asterix spectrum represented 190.5 flights (or 140 sorties) and was composed of 371,610 cycles.

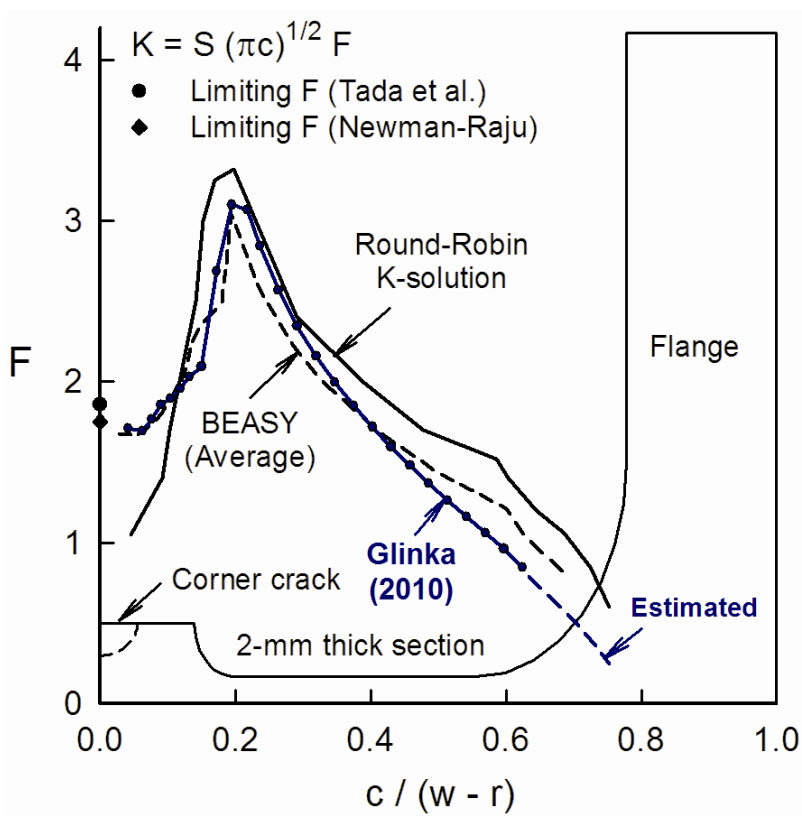

Figure 79. Effective Stress Intensity Factor Range-Against-Rate for Aluminum Alloy at Various *R*

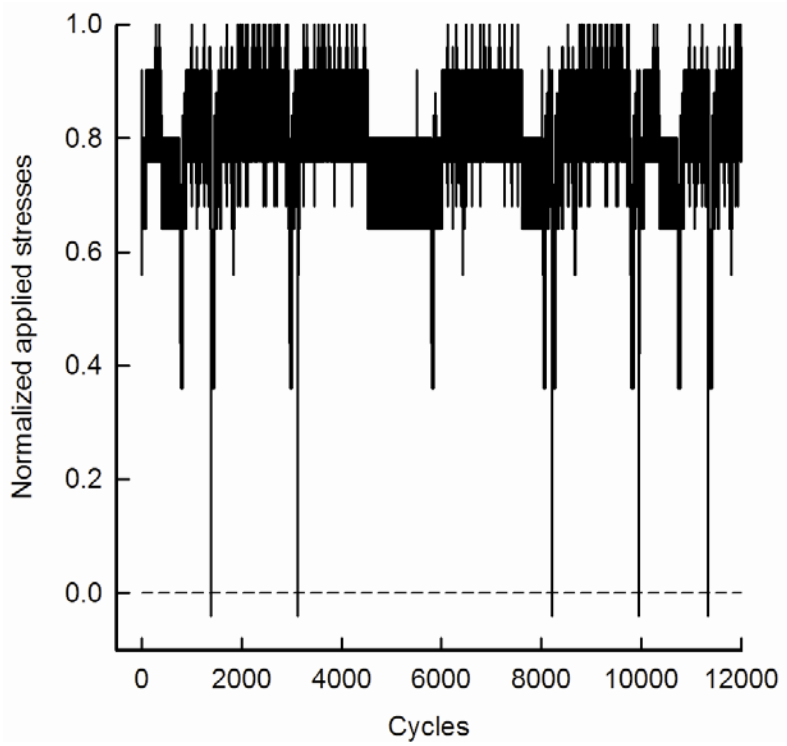

Figure 80. Part of the Stress-Cycle History for Asterix Spectrum Loading

6.6 PREDICTED CRACK-LENGTH-AGAINST-CYCLES BEHAVIOR.

The results of two tests conducted on the round robin crack configuration are shown in figure 81 as symbols. FASTRAN [16] was used to make two predictions. In the first, the dashed curve shows the predicted results made with the original *K*-solution provided in the round robin (these particular results were not submitted to the round robin organizers). However, these results are similar to most of the other predictions submitted in the round robin, in that the predicted shape of the curve does not match the test data, especially in the early stages of crack growth. The predicted results are too long in the early stages of crack growth by a factor of approximately two; however, for crack growth in the 2-mm-thick material region, the rate of growth is significantly faster than the test data (the bar on the figure shows a schematic of the various thickness regions for the round robin configuration). Ironically, the crack growth life at the 25-mm location was exceptionally close to the average of the two tests. The second crack growth calculation (solid curve) was made with the BEASY *K*-solution (average) and, here, the early stages of crack growth compared very well with the test data. Again, however, the FCG rates in the 2-mm-thick section developed too fast. The final flight hour at the 25-mm crack length was 30 percent shorter than the average test results. Based on an estimated *K*-solution for larger crack lengths, the dash curve is an estimated extension of the predicted results.

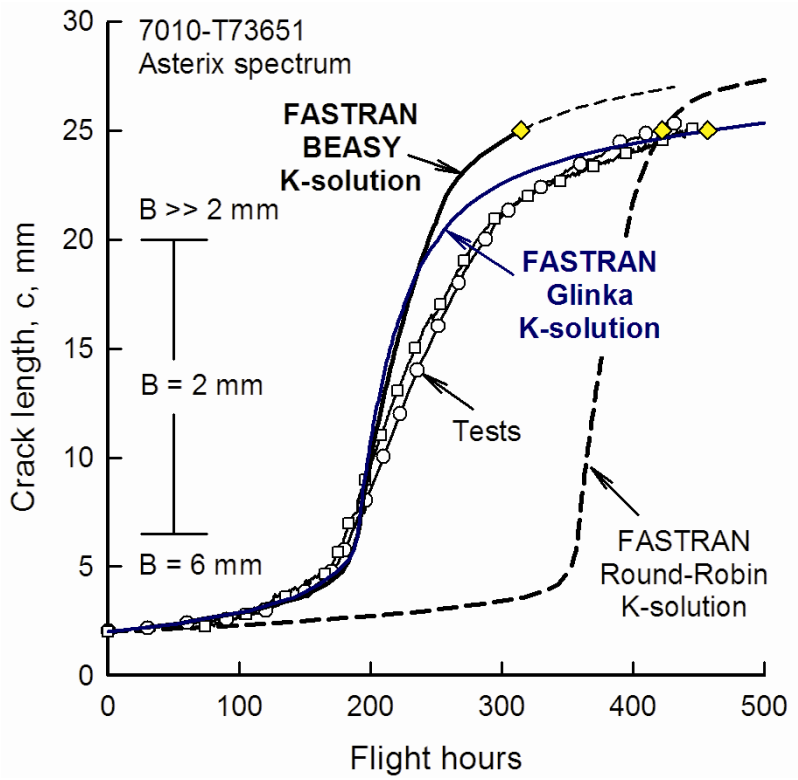

Figure 81. Measured and Predicted Crack Length-Against-Flights for Round-Robin Problem

The 2-mm-thick FCG-rate data was unavailable. However, for the thinner material, it is expected that a lower constraint factor would be operational, which would give higher crack opening stresses and longer FCG lives during this phase. Whether FCG-rate data for the 2-mm-thick material and the lower constraint factor would give better crack growth predictions under the Asterix spectrum is a question that must await further studies.

6.7 RESULTS.

The life prediction code, FASTRAN, was used to predict FCG in the 7010 aluminum alloy under a standard rotorcraft spectrum loading. The CA FCG-rate data on the material and a plane strain constraint factor were used to generate an effective stress intensity factor-against-rate relation. For the round-robin crack configuration, the average stress intensity factors from a three-dimensional BEASY analysis were used. The materials data (the crack length-against-flight hours) agreed very well in the early stages of crack growth. However, the model predicted faster crack growth during the thin (2-mm) section. The predicted crack growth life at a crack length of 25 mm was 30 percent short of two tests conducted under the Asterix helicopter spectrum. Using the new stress intensity factor solution from Glinka resulted in a more accurate life from 2 to 25 mm, but the shape of the crack length-against-flight hour curve, again, developed too fast in the 2-mm-thick section. Further study and more tests are needed to resolve the crack growth inconsistencies for the thin section.

Prediction of crack growth lives in helicopters, unlike in fixed-wing aircraft, requires accurate calculations in the near-threshold regime of the FCG-rate curves, where scatter in material data,

small changes in curve fitting, and errors in stress intensity factor calculations all result in substantial changes in predicted lives. Accurate life calculations under helicopter spectra require more accurate values of stress intensity factors, material FCG-rate data, and load spectra than has been observed with fixed-wing aircraft.

7. CONCLUSION.

Rotorcraft components are subjected to high-cycle fatigue loading where a damage-tolerant crack (1 mm in size) may grow to failure in a short time because of the large number of service cycles. Thus, lifing in a rotorcraft component should be accomplished through a combination of fatigue, small crack, and large crack behavior where crack growth thresholds for small and large cracks are extremely important. Currently, for large cracks, the threshold crack growth regime is experimentally defined by using American Society for Testing and Materials (ASTM) Standard E-647, which has been shown to exhibit anomalies due to load reduction (LR) test procedures, prematurely slow down crack growth, and produce an abnormally high threshold for some materials.

The scope of this research project was to: (1) further develop the CP threshold testing methods, (2) determine fatigue crack growth (FCG) rates in the near-threshold regime and over a wide range in rates (from threshold to near-fracture) for four materials (aluminum alloys 2024-T3, 2324-T39, 7050-T7451, and 9310 steel), (3) measure crack-closure (or crack-opening) behavior for large cracks in the threshold regime for most of the materials considered, (4) conduct fatigue tests on two materials (7050-T7451 aluminum alloy and 9310 steel) using a new fatigue test specimen, (5) compare small and large crack behavior on several of the materials from the literature, and (6) conduct fatigue analyses on the two materials (7050-T7451 aluminum alloy and 9310 steel) using small crack theory. Three types of threshold tests were conducted on most materials. They were: (1) the ASTM E-647 LR procedure, (2) the compression precracking, constant-amplitude CPCA test method, and (3) the compression precracking load-reduction (CPLR) test method. Results on an additional test method, compression precracking constant-ΔK (CPCK) loading, were also presented on one material. All tests were conducted under a laboratory air environment at room temperature. Crack closure measurements using a local (sideface) strain gage indicated that crack closure occurred at all stress (R) ratios, even at very high R values, where test results had been suspected to be crack closure-free data. The crack closure concept was able to correlate the near-threshold FCG-rate behavior onto nearly unique effective stress intensity factor range-against-rate relations. Small crack theory was able to calculate the fatigue stress-life (S-N) behavior using equivalent initial flaw sizes for several materials. Results from single-spike overloads and aircraft spectrum loading on several materials were calculated from the strip-yield model, FASTRAN, reasonably well, except for the 7050-T7451 aluminum alloy that developed a very rough fatigue crack surface. Further studies are needed to develop a combined model of plasticity-, roughness-, and debris-induced crack closure behavior.

The five conclusions and outcomes of this research are as follows:

1. Procedures have been established to prepare test specimens, apply compressive loading to initiate a crack at a crack-starter notch, and generate steady-state, constant amplitude (CA) loading FCG rate data for metallic materials.

2. The CPCA and CPLR test methods tended to generate lower thresholds and faster FCG rates in the near-threshold regime than the standard ASTM LR method for all materials. For some materials, the differences in ΔK_{th} were small (~10%), but for other materials, the differences were as large as 50%.

3. The CA FCG-rate data have been generated on four materials (aluminum alloys 2024-T3, 2324-T39, 7050-T7451, and 9310 steel) from threshold to near-fracture over a wide range in stress ratios.

4. Tests conducted at very high stress ratios (R>0.7) show a continuously shifting FCG-rate curve to lower stress intensity factor ranges with increasing stress ratio, which appear to have been caused by a combination of plasticity-, roughness-, and debris-induced crack closure effects. This observation was based on local crack closure measurements made on the surface of compact specimens in the near-threshold regime.

5. The effective stress intensity factor range-against-rate (ΔK_{eff}-rate) relation has been developed for all of the materials tested and analyzed in this report. These relations may be used in various damage-tolerance life-prediction codes to assess the FCG lives of structural components.

8. REFERENCES.

1. *NASGRO Reference Manual*, Version 5.2, Southwest Research Institute and NASA Johnson Space Center, 2008.

2. Harter, J.A. *AFGROW Users Guide and Technical Manual*, AFRL-VA-WP-TR-2002, Version 4.0005.12.10, Air Force Research Laboratory, Wright Patterson Air Force Base, Ohio, July 2002.

3. ASTM Standard E-647-08, "Standard Test Method for Measurement of Fatigue Crack Growth Rates," ASTM International, West Conshohocken, Pennsylvania, 2009.

4. Hudak, S., Jr., Saxena, S., Bucci, R., and Malcolm, R., "Development of Standard Methods of Testing and Analyzing Fatigue Crack Growth Rate Data—Final Report," AFML TR 78-40, Air Force Materials Laboratory, Wright Patterson Air Force Base, Ohio, 1978.

5. Newman, J.C., Jr., "A Nonlinear Fracture Mechanics Approach to the Growth of Small Cracks," *AGARD Conference Proceedings No. 328*, 1983, pp. 6.1-6.26.

6. Donald, J.K and Paris, P.C., "An Evaluation of ΔK_{eff} Estimation Procedures on 6061-T6 and 2024-T3 Aluminum Alloys," *International Conference on Fatigue Damage of Structural Materials*, Cape Cod, Massachusetts, September 7-11, 1998.

7. Marci, G., "A Fatigue Crack Growth Threshold," *Engineering Fracture Mechanics*, Vol. 42, 1992, pp. 367-385.

8. Tabernig, B., Powell, P., and Pippan, R., "Resistance Curves for the Threshold of Fatigue Crack Propagation in Particle Reinforced Aluminum Alloys," ASTM STP-1372, J. Newman, Jr. and R. Piascik, eds., West Conshohocken, Pennsylvania, 2000, p. 96.

9. Vasudevan, A.K., Sadananda, K., and Louat, N., "A Review of Crack Closure, Fatigue Crack Threshold and Related Phenomena," *Materials Science and Engineering*, A188, 1994, pp. 1-22.

10. Sadananda, K. and Vasudevan, A.K., "Analysis of Fatigue Crack Closure and Thresholds," Fracture Mechanics: 25th Volume, ASTM STP-1220, F. Erdogan, ed., Philadelphia, Pennsylvania, 1995, pp. 484-501.

11. Topper, T.H., Au, P., and El Haddad, M.L., "The Effects of Compressive Overloads on the Threshold Stress Intensity for Short Cracks," AGARD Conference Proceedings, No. 328, 1983, pp. 11.1-11.7.

12. Suresh, S., "Crack Initiation in Cyclic Compression and its Application," *Engineering Fracture Mechanics*, Vol. 21, 1985, pp. 453-463.

13. Pippan, R., Plöchl, L., Klanner, F., and Stüwe, H. P., "The Use of Fatigue Specimens Precracked in Compression for Measuring Threshold Values and Crack Growth," *ASTM Journal of Testing and Evaluation*, Vol. 22, 1994, p. 98.

14. Forth, S.C., Newman, J.C., Jr., and Forman, R. G., "Evaluation of Fatigue Crack Thresholds Using Various Experimental Methods," Fatigue and Fracture Mechanics: 33rd Volume, ASTM STP 1461, S.R. Daniewicz, J.C. Newman, Jr., and K.-H. Schwalbe, eds., West Conshohocken, Pennsylvania, 2005, pp. 203-218.

15. Minakawa, K. and McEvily, A. J., "On Near-Threshold Fatigue Crack Growth in Steels and Aluminum Alloys," *Proceedings International Conference on Fatigue Thresholds*, Vol. 2, Stockholm, Sweden, 1981, pp. 373-390.

16. Newman, J.C., Jr., "FASTRAN-II—A Fatigue Crack Growth Structural Analysis Program," NASA TM 104159, February 1992.

17. Newman, J.C., Jr., Schneider, J. A., Daniel, A., and McKnight, D., "Compression Pre-cracking to Generate Near Threshold Fatigue-Crack-Growth Rates in Two Aluminum Alloys," *International Journal of Fatigue*, Vol. 27, 2005, pp. 1432-1440.

18. James, M.A., Forth, S.C., and Newman, J.A., "Load History Effects Resulting From Compression Precracking", Fatigue and Fracture Mechanics: 33rd Volume, ASTM STP 1461, S.R. Daniewicz, J.C. Newman, Jr., and K.-H. Schwalbe, eds., West Conshohocken, Pennsylvania, 2005, pp. 43-59.

19. Newman, J.C., Jr., Yamada, Y., and Vizzini, T., "Fatigue Crack Growth Databases and Analyses for Threshold Behavior in Rotorcraft Materials," FAA report DOT/FAA/AR-10/3, March 2010.

20. Newman, J.A. and Johnston, W.M., "Evaluation of a Small-Crack Monitoring System," NASA/TM-2010-216201, February 2010.

21. Edwards, P.R. and Newman, J.C., Jr., eds., "Short-Crack Growth Behavior in Various Aircraft Materials," AGARD Report No. 767, 1990.

22. Newman, J.C., Jr. and Edwards, P.R., "Short-Crack Growth Behaviour in an Aluminum Alloy—An AGARD Cooperative Test Programme," AGARD Report No. 732, 1988.

23. Newman, J.C., Jr., Wu, X.R., Venneri, S.L., and Li, C.G., "Small-Crack Effects in High-Strength Aluminum Alloys—A NASA/CAE Cooperative Program," *NASA RP-1309*, May 1994.

24. Yamada, Y. and Newman, J.C., Jr., "Crack Closure Under High Load-Ratio Conditions for Inconel 718 Near Threshold Behavior," *Engineering Fracture Mechanics*, Vol. 76, 2009, pp. 209-220.

25. Yamada, Y. and Newman, J.C., Jr., "Crack Closure Behavior of 2324-T39 Aluminum Alloy Near Threshold Conditions for High Load Ratio and Constant K_{max} Tests," *International Journal of Fatigue*, Vol. 31, 2009, pp. 1780-1787.

26. Yamada, Y. and Newman, J. C., Jr., "Crack Closure Behavior on a Variety of Materials Under High Stress Ratios and K_{max} Test Conditions," *Journal of ASTM International*, 2011.

27. Newman, J.C., Jr., Yamada, Y., and Newman, J.A., "Crack-Closure Behavior of 7050 Aluminum Alloy Near Threshold Conditions for Wide Range in Load Ratios and Constant K_{max} Tests," *Journal of ASTM International*, Vol. 7, No. 4, 2010.

28. Elber, W., "Crack Closure and Crack-Growth Measurements in Surface-Flawed Titanium Alloy Ti-6Al-4V," NASA-TN-D-8010, 1975.

29. Hudson, C.M., "Effect of Stress Ratio on Fatigue-Crack Growth in 7075-T6 and 2024-T3 Aluminum-Alloy Specimens," NASA TN D-5390, August 1969.

30. Phillips, E.P., "The Influence of Crack Closure on Fatigue Crack Growth Thresholds in 2024-T3 Aluminum Alloy," ASTM STP 982, 1988, pp. 505-515.

31. Dubensky, R. G., "Fatigue Crack Propagation in 2024-T3 and 7075-T6 Aluminum Alloys at High Stress," NASA CR-1732, March 1971.

32. *ASM Metals Reference Book*, 2nd Ed., Metals Park, Ohio, American Society for Metals, 1983.

33. Alcoa Mill Products, "Technical Data," www.millproducts-alcoa.com, accessed on January 28, 2013.

34. Latrobe Specialty Steel Company, "Technical Data Sheet," 2007, www.latrobesteel.com, accessed on January 28, 2013.

35. Paris, P.C., Bucci, R., Wessel, E., Clark, W., and Mager, T., "Extensive Study of Low Fatigue Crack Growth Rates in A533 and A508 Steels," ASTM STP 513, American Society for Testing and Materials, Philadelphia, Pennsylvania, 1972, pp. 141-176.

36. Schmidt, R.A. and Paris, P.C., "Threshold for Fatigue Crack Propagation and the Effects of Load Ratio and Frequency," ASTM STP-536, American Society for Testing and Materials, Philadelphia, Pennsylvania, 1973, pp. 79-94.

37. Bucci, R., "Development of a Proposed ASTM Standard Test Method for Near-Threshold Fatigue Crack Growth Rate Measurement," ASTM STP-738, American Society for Testing and Materials, Philadelphia, Pennsylvania, 1981, pp. 5-28.

38. Herman, W., Hertzberg, R., and Jaccard, R., "A Simplified Laboratory Approach for the Prediction of Short Crack Behavior in Engineering Structures," *Fatigue and Fracture of Engineering Materials and Structures*, Vol. 11, 1988, pp. 303-320.

39. Elber, W., "The Significance of Fatigue Crack Closure," *Damage Tolerance in Aircraft Structures*, ASTM STP-486, American Society for Testing and Materials, Philadelphia, Pennsylvania, 1971, pp. 230-242.

40. Walker, N. and Beevers, C.J., "A Fatigue Crack Closure Mechanism in Titanium," *Fatigue of Engineering Materials and Structures*, Vol. 1, No. 1, 1979, pp. 135-148.

41. Suresh, S. and Ritchie, R.O., "A Geometric Model for Fatigue Crack Closure Induced by Fracture Surface Roughness," *Metallurgical Transactions*, Vol. 13A, 1982, pp. 1627-1631.

42. Suresh, S., Parks, D., and Ritchie, R., "Crack Tip Oxide Formation and Its Influence on Fatigue Thresholds," *Fatigue Thresholds*, J. Backlund, A. Blom, and C. Beevers, eds., Engineering Materials Advisory Service Publ. Ltd., Vol. 1, Warley, United Kingdom, 1982, pp. 391-408,.

43. Hubbard, R.P., "Crack Growth Under Cyclic Compression," *Journal of Basic Engineering*, Vol. 91, 1969, pp. 625-631.

44. Topper, T.H. and Au, P., "Fatigue Test Methodology," AGARD Lecture Series 118, Fatigue Test, The Technical University of Denmark, Denmark, 1981.

45. Pippan, R., "The Growth of Short Cracks Under Cyclic Compression," *Fatigue and Fracture of Engineering Materials and Structures*, Vol. 9, 1987, pp. 319-328.

46. Forth, S.C., Newman, J.C., Jr., and Forman, R.G., "On Generating Fatigue Crack Growth Thresholds," *International Journal of Fatigue*, Vol. 25, 2003, pp. 9-15.

47. Newman, J.C., Jr. and Yamada, Y., "Compression Precracking Methods to Generate Near-Threshold Fatigue-Crack-Growth-Rate Data," *International Journal of Fatigue*, Vol. 32, 2010, pp. 879-885.

48. Newman, J.C., Jr., Ruschau, J.J., and Hill, M.R., "Improved Test Method for Very Low Fatigue-Crack-Growth-Rate Data," *Fatigue and Fracture Engineering Materials and Structures*, Vol. 34, No. 4, 2011, pp. 270-279.

49. Ruschau, J. and Newman, J.C., Jr., "Compression Precracking to Generate Near Threshold Fatigue Crack Growth Rates in an Aluminum and Titanium Alloy," *Journal of ASTM International*, Vol. 5, No. 7, 2008.

50. Yamada, Y., Newman, J.C., III, and Newman, J.C., Jr., "Elastic-Plastic Finite-Element Analyses of Compression Precracking and Its Influence on Subsequent Fatigue-Crack Growth," *Journal of ASTM International*, Vol. 5, No. 8, 2008.

51. Donald, J.K., "A Procedure for Standardizing Crack Closure Levels," ASTM STP-982, American Society for Testing and Materials, Philadelphia, Pennsylvania., 1988, pp. 222-229.

52. Newman, J.C., Jr., Yamada, Y., and James, M.A., "Back-face Strain Compliance Relation for Compact Specimens for Wide Range in Crack Lengths," *Engineering Fracture Mechanics*, Vol. 78, 2011, pp. 2707-2711.

53. Chang, C. and Mear, M.E., "A Boundary Element Method for Two-Dimensional Linear Elastic Fracture Analysis," *International Journal of Fracture*, Vol. 74, 1996, pp. 219-251.

54. James, M.A. and Swenson, D.V., "A Software Framework for Two Dimensional Mixed Mode-I/II Elastic-Plastic Fracture," ASTM STP-1359, American Society for Testing and Materials, Philadelphia, Pennsylvania, 1999, pp. 111-126.

55. Tada, H., Paris, P.C., and Irwin, G.R., *The Stress Analysis of Cracks Handbook*, Third Edition, The American Society of Mechanical Engineers, January 1, 2000.

56. Newman, J.C., Jr., Ziegler, B.M., Shaw, J.W., Cordes, T.S., and Lingenfelser, D.J., "Fatigue Crack Growth Rate Behavior of A36 Steel using ASTM Load-Reduction and Compression Precracking Test Methods," *Journal of ASTM International*, Vol. 9, No. 2, 2012, JAI 103966, available at www.astm.org.

57. Dugdale, D.S., "Yielding of Steel Sheets Containing Slits," *Journal of the Mechanics and Physics of Solids*, Vol. 8, 1960, pp. 100-104.

58. "FALSTAFF—A Description of Flight Aircraft Standard for Fatigue Evaluation," Combined Report of F&W, LBF, NLR, and IABG, 1976.

59. Murakami, Y. ed., "The Rainflow Method in Fatigue," *International Symposium Fatigue Damage Measurement and Evaluation Under Complex Loadings*, Fukuoka, Japan, 1991.

60. de Jonge, J.B., Schutz, D., Lowak, H., and Schijve, J., "A Standardized Load Sequence for Flight Simulation Tests on Transport Aircraft Wing Structures," LBF-Bericht FB-106, NLR TR 73029 U, 1973.

61. Lowak, H., de Jonge J. B., Franz, J., and Schutz, D., "MINITWIST: A Shortened Version of TWIST," LBF-Bericht FB-146, Laboratorium fur Betriebsfestigkeit, 1979.

62. Rice, R.C., Jackson, J.L., Bakuckas, J., and Thompson, S., Metallic Materials Properties Development and Standardization, FAA Report DOT/FAA/AR-MMPDS-01, January 2003.

63. Barter, S. A., Sharp, P. K., Holden, G., and Clark, G., "Initiation and Early Growth of Fatigue Cracks in an Aerospace Aluminum Alloy," *Fatigue and Fracture of Engineering Materials and Structures*, Vol. 25, 2002, pp. 111-125.

64. Newman, J.C., Jr., Swain, M.H., and Phillips, E.P., "An Assessment of the Small Crack Effect for 2024-T3 Aluminum Alloy," Small Fatigue Cracks, R.O. Ritchie and J. Lankford, eds., 1986, pp. 427-452.

65. Donald, J.K., "Introducing the Compliance Ratio Concept for Determining Effective Stress Intensity," *International Journal of Fatigue*, Vol. 19, Supp. No. 1, 1997, pp. S191-S195.

66. Donald, J.K. and Blair, A., "Automated Fatigue Crack Growth Testing and Analysis—Series 2001," Version 3.09, Fracture Technology Associates, LLC, Bethlehem, Pennsylvania, March 2009.

67. Dawicke, D., Shivakumar, K., Newman, J.C., Jr., and Grandt, A., "An Inverse Method for the Calculation of Through-Thickness Fatigue Crack Closure Behavior," ASTM STP 1131, 1992, pp. 46-57.

68. Newman, J.C., Jr., "A Crack-Closure Model for Predicting Fatigue Crack Growth Under Aircraft Spectrum Loading," ASTM STP-748, American Society for Testing and Materials, Philadelphia, Pennsylvania, 1981, pp. 53-84.

69. Newman, J.C., Jr., "Analysis of Fatigue Crack Growth and Closure Near Threshold Conditions," ASTM STP-1372, J. C. Newman, Jr. and R. S. Piascik, eds., 2000.

70. Newman, J.C., Jr., "Prediction of Fatigue Crack Growth Under Variable Amplitude and Spectrum Loading Using a Closure Model," Design of Fatigue and Fracture Resistant Structures, ASTM STP-761, 1982, pp. 255-277.

71. Yamada, Y. and Newman, J.C., Jr., "Crack Closure Under High Load Ratio and K_{max} Test Conditions," *Fatigue 2010*, Prague, Czech Republic, June 2010.

72. Newman, J.C., Jr. "Effects of Constraint on Crack Growth Under Aircraft Spectrum Loading", *Fatigue of Aircraft Materials*, A. Beukers et al., eds., Delft University Press, Delft, Netherlands, 1992, pp. 83-109.

73. Miller, M.S. and Gallagher, J.P., "An Analysis of Several Fatigue Crack Growth Rate (FCGR) Descriptions," ASTM STP-738, American Society for Testing and Materials, 1981, pp. 205-251.

74. Newman, J.C., Jr., "Fracture Analysis of Surface- and Through-Cracked Sheets and Plates," *Engineering Fracture Mechanics*, Vol. 5, 1973, pp. 667-689.

75. Newman, J.C., Jr., "Fracture Analysis of Various Cracked Configurations in Sheet and Plate Materials," *Properties Related to Fracture Toughness*, ASTM STP 605, American Society for Testing and Materials, Philadelphia, Pennsylvania, 1976, pp. 104-123.

76. Tomkins, B., "Fatigue Crack Propagation—An Analysis," *Philosophical Magazine*, Vol. 18, 1968, pp. 1041-1066.

77. Bilby, B. A., Cottrell, A. H. and Swinden, K. H., "The Spread of Plastic Yield From a Notch," *Proceedings of the Royal Society*, Vol. 272(A), 1963, p. 304.

78. Rice, J. R., "A Path Independent Integral and the Approximate Analysis of Strain Concentration by Notches and Cracks," *Journal of Applied Mechanics*, Vol. 35, 1968, pp. 379-386.

79. Dowling, N.E. and Begley, J.A., "Fatigue Crack Growth During Gross Plasticity and the J-Integral," ASTM STP-590, American Society for Testing and Materials, 1976, pp. 82-103.

80. Newman, J.C., Jr., "Fracture Mechanics Parameters for Small Fatigue Cracks," ASTM STP-1149, American Society for Testing and Materials, 1992, pp. 6-33.

81. Newman, J.C., Jr., "An Evaluation of Plasticity-Induced Crack Closure Concept and Measurement Methods," ASTM STP-1343, American Society for Testing and Materials, 1999, pp. 128-144.

82. Ogura, K., Miyoshi, Y., and Nishikawa, I., "Fatigue Crack Growth and Closure of Small Cracks at the Notch Root," *Current Research on Fatigue Cracks*, T. Tanaka, M. Jono, and K. Komai, eds., *Society of Material Science*, Japan, 1985, pp. 57-78.

83. Laz, P.J. and Hillberry, B.M., *The Role of Inclusions in Fatigue Crack Formation in Aluminum 2024-T3, Fatigue 96*, Lutjering G. and Nowack, H., eds., Berlin, Germany, 1996, pp. 1293-1298.

84. Manning, S.D. and Yang, J.N., *USAF Durability Design Handbook: Guidelines for the Analysis and Design of Aircraft Structures*, AFWAL-TR-83-3027, 1984.

85. Newman, J.C., Jr., "Modeling Small Fatigue Crack Behavior," *Fatigue 93*, J.P. Bailon and J.I. Dickson, eds., Montreal, Canada, 1993, pp. 33-44.

86. Marines, I., Bin, C., and Bathias, C., "An Understanding of Very High Cycle Fatigue of Metals," *International Journal of Fatigue*, Vol. 25, 2003, pp. 1101-1107.

87. Landers, C. B. and Hardrath, H. F., "Results of Axial-Load Fatigue Tests on Electropolished 2024-T3 and 7075-T6 Aluminum Alloy Sheet Specimens with Central Holes," NACA TN-3631, 1956.

88. Huck, M., Schutz, W., Fischer, R., and Kobler, H., "A Standard Random Load Sequence of Gaussian Type Recommended for General Application in Fatigue Testing." LBF Report No. 2909, Industrieanlagen Betriebsgesellschaft, IABG Report No. TF-570, April, 1976.

89. Everett, R.A., Jr. "A Comparison of Fatigue Life Prediction Methodologies for Rotorcraft," NASA TM 102759, December, 1990.

90. Klesnil, M. and Lukas, P., "Effect of Stress Cycle Asymmetry on Fatigue Crack Growth," *Material Science and Engineering*, Vol. 9, pp. 231-240, 1972.

91. Walker, K.F. and Barter, S.A., "The Critical Importance of Correctly Characterising Fatigue Crack Growth Rates in the Threshold Regime," International Committee on Aeronautical Fatigue, 26th ICAF Symposium, Montreal, Canada, June 1-3, 2011.

92. Yamada, Y., Ziegler, B., and Newman, J.C., Jr., "Application of a Strip-Yield Model to Predict Crack Growth Under Variable-Amplitude and Spectrum Loading—Part 1: Compact Specimens," *Engineering Fracture Mechanics*, Vol. 78, 2011, p. 2597.

93. Elber, W., "Fatigue Crack Closure Under Cyclic Tension," *Engineering Fracture Mechanics*, Vol. 2, No. 1, 1970, pp. 37-45.

94. Newman, J.C., Jr., "A Crack-Opening Stress Equation for Fatigue Crack Growth," *International Journal of Fracture*, Vol. 24, 1984, R131-R135.

95. Newman, J.A., "The Effects of Load Ratio on Threshold Fatigue Crack Growth of Aluminum Alloys," Ph.D. Thesis, Virginia Polytechnic Institute and State University, October 2000.

96. Newman, J.A., Riddell, W.T., and Piascik, R.S., "A Threshold Fatigue Crack Closure Model: Part I—Model Development," *Fatigue and Fracture Engineering Materials and Structures*, Vol. 26, 2003, pp. 603-614.

97. Kim, J.H. and Lee, S.B., "Behavior of Plasticity-Induced Crack Closure and Roughness-Induced Crack Closure in Aluminum Alloy," *International Journal of Fatigue*, Vol. 23, 2001, pp. S247-S251.

98. Barter, S.A., Bishop, B., and Clark, G., "Defect Assessment on F/A-18 488 Bulkhead Tested at ARL," Aircraft Materials Report 125, AR-006-618, Department of Defence, Defence Science and Technology Organisation, Aeronautical Research Laboratory, Melbourne, Victoria, Australia, 1991.

99. Liao, M. Chisholm, K., and Mahendran, M., "Statistical Analysis of Fatigue Related Microstructural Parameters for Airframe Aluminum Alloys," *Journal of ASTM International*, Vol. 6, No. 2, 2009, pp. 1-15.

100. Walker, K.F. and Barter, S.A., "The Critical Importance of Correctly Characterising Fatigue Crack Growth Rates in the Threshold Regime," ICAF 2011 Structural Integrity: Influence and Efficiency of Green Imperatives: Proceedings of the 26th Symposium of the International Committee on Aeronautical Fatigue, J. Komorowski (ed.), Springer, pp. 249-263.

101. Zeigler, B., "Fatigue and Fracture Testing and Analysis on Four Engineering Materials," Ph.D. Thesis, Mississippi State University, April 2011.

102. White, P., Barter, S., and Molent, L., "Observations of Crack Path Changes Caused by Periodic Underloads in AA 7050-T7451," *International Journal of Fatigue*, Vol. 30, No. 7, 2008, pp. 1267-1278.

103. Hudson, C.M. and Hardrath, H.F., "Investigation of the Effects of Variable-Amplitude Loadings on Fatigue Crack Propagation Patterns," NASA TN D-1803, 1963.

104. Liu, J.Z., Wu, X.R., Ding, C.F., et al. "Crack Growth Behavior and Fatigue-Life Prediction Based on Worst-Case Near-Threshold Data of a Large Crack for 9310 Steel," *Fatigue and Fracture of Engineering Materials and Structures*, Vol. 25, 2002, pp. 467-480.

105. Cansdale, R. and Perrett, B., "The Helicopter Damage Tolerance Round-Robin Challenge," *Workshop on Fatigue Design of Helicopters*, University of Pisa, Italy, September 12-13, 2002.

106. Irving, P., Lin, J., and Bristow, J., "Damage Tolerance in Helicopters—Report on the Round-Robin Challenge," *American Helicopter Society 59th Annual Forum*, Phoenix, Arizona, May 6-8, 2003.

107. Newman, J.C., Jr., Irving, P.E., Lin, J., and Le, D.D., "Crack Growth Predictions in a Complex Helicopter Component Under Spectrum Loading," *Fatigue and Fracture of Engineering Materials and Structures*, Vol. 29, No. 11, 2006, pp. 949-958.

108. "A Standardised Fatigue Loading Sequence for Helicopter Airframe Structures (Asterix)," Research Paper RP980, GKN Westland Helicopters, Department of Trade and Industry Link Contract No. RA/6/30/06, 1996.

109. Irving, P. and Buller, R. "Prediction of Fatigue Life Under Helicopter Loading Spectra for Safe Life and Damage Tolerant Design," ASTM STP 1332, American Society of Testing and Materials, West Conshohocken, Pennsylvania, 1999, pp.727-742.

110. Computational Mechanics, Inc., "BEASY—Fatigue and Crack Growth Software," Billerica, Massachusetts, <www.beasy.com>, accessed January 28, 2013.

111. Newman, J.C., Jr. and Raju, I.S., "Stress-Intensity Factor Equations for Cracks in Three-Dimensional Finite Bodies Subjected to Tension and Bending Loads," *Computational Methods in the Mechanics of Fracture*, S.N. Atluri, ed., Elsevier, 1986, pp. 311-334.

APPENDIX A—CRACK OPENING LOAD MEASUREMENT METHOD

A.1 INTRODUCTION.

Elber [A1 and A2] observed fatigue crack surfaces contact under cyclic tensile loading, and this observation and the crack closure concept began to explain many crack growth characteristics under both constant- and variable-amplitude loading. Almost immediately, methods to measure the crack opening load under constant amplitude loading were investigated and developed. But very little effort has been made for variable amplitude loading. Some work has been done under single-spike overloads [A-3]. However, the ability to measure true crack opening loads under cyclic loading has been a very difficult task. Nonlinearities in displacement or strain measurement systems, location of measurements, and electronic noise have contributed to this problem. In addition, the crack closure process is three-dimensional in nature with more closure occurring at and near the free surface than in the interior [A-4].

One of the most widely known methods is the compliance offset method, as standardized in American Society for Testing and Materials (ASTM) E-647 [A-5]. This method uses remote gages, such as the crack mouth opening displacement gage or backface strain gage, to measure the load against displacement or strain record under cyclic loading. Unfortunately, the ASTM-recommended 2% offset value has not proven to be very useful in correlating fatigue crack growth- (FCG)- rate data over a wide range in stress ratios (R) and has led some to question the crack closure concept.

However, Elber [A-6] had originally used a local displacement gage mounted near the fatigue crack tip location to measure the load-against-crack tip opening displacement records during cyclic loading. He then developed a load against reduced displacement method [A-6] to improve the detection of the subtle compliance changes associated with the crack opening load. This method has not been widely used because remote methods were being used to monitor crack length, so it was thought that these remote methods could also be used to measure crack opening loads. The load reduced displacement or strain method is also referred to as the "zero percent offset" method.

Recently, Yamada and Newman [A-7 and A-8] have used the zero percent offset method and have been able to correlate FCG-rate data in the threshold and near-threshold regimes for a wide variety of materials for both low- and high-stress ratio (R) tests, and K_{max} tests. Their results, using local strain gages mounted on the side of compact specimens near the crack tip location, have shown that high R tests, which had previously been thought to be crack closure-free, developed crack closure as threshold conditions were approached. The rise in crack opening loads was thought to be caused by a combination of plasticity-, debris-, and roughness-induced crack closure effects. They also found that at low R, like 0.1, the local and remote (1% offset) methods agreed fairly well. Many years ago, this may have been why the remote methods were thought to be accurate methods to measure crack opening loads. However, major discrepancies occurred under high-R conditions. Elber's reduced displacement or strain method is presented below.

A.2 LOAD-AGAINST-DISPLACEMENT OR STRAIN RECORDS.

Figure A-1 shows a typical load-against-displacement or strain record measured on a fatigue crack that has been grown under cyclic loading. This schematic example has been highly exaggerated to show the cyclic hysteresis curve for loading and unloading. This type of behavior occurs under high applied stress levels that have large-scale yielding around the crack tip location. On unloading, the load displacement or strain behavior is linear and becomes nonlinear as reverse yielding occurs at the crack tip and as the crack surface begins to close. The initial crack closure load cannot be determined because reverse yielding and crack closure have opposite effects on the load displacement or strain record. At lower loads, the crack surfaces close and cause a nonlinear curve. On loading, the crack peels open. When the crack tip opens, the load displacement or strain record is, again, linear at and slightly beyond the crack opening load. As shown here, the precise crack opening load cannot be determined from the load displacement or strain curve. Further loading causes the crack tip region to yield under tensile plastic deformation. The load displacement or strain curve closes to its original value, as before unloading, if the crack has not grown significantly during the tensile portion of the loading curve. Crack extension during one tensile loading is extremely small and may not be detected on the load displacement or strain record.

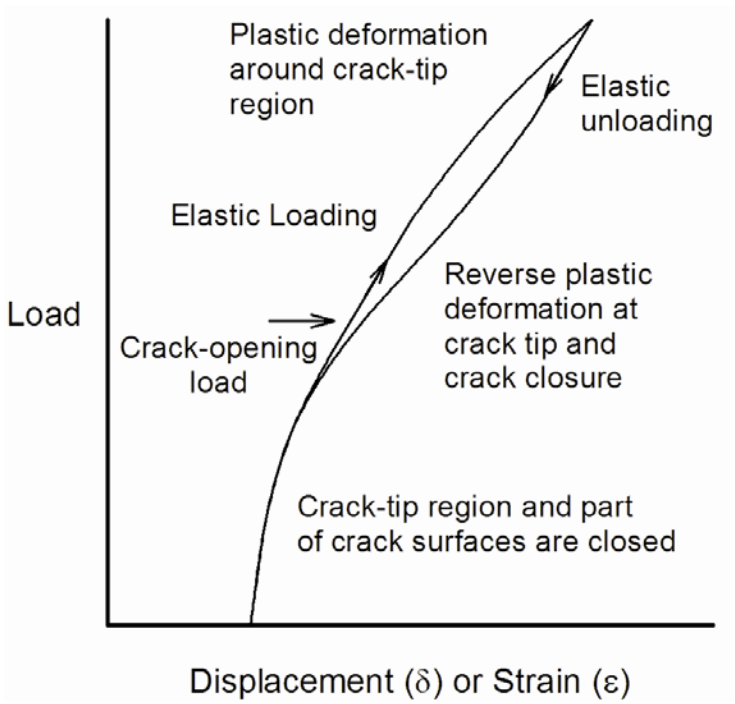

Figure A-1. Load-Against-Displacement or Strain Record

Under normal fatigue loading, at small values of applied stress levels and low FCG rates, the load displacement or strain records have extremely small hysteresis loops and, generally, they cannot be observed. Further processing of the load displacement or strain record is required to determine the proper crack opening load.

A.3 LOAD-AGAINST-REDUCED DISPLACEMENT OR STRAIN RECORDS.

As pointed out by Elber [A-6], the elastic unloading and loading portions of the record can be used to help establish the crack opening load. The elastic unloading portion of the curve is used to establish a straight line, as shown by the dashed line in figure A-2. For the loading and unloading records, the differences in displacement ($\Delta\delta$) or strain ($\Delta\varepsilon$) are calculated; and the load-reduced displacement or strain curve is shown in figure A-3. Then the crack opening load can be more easily determined when the loading portion of the curve becomes vertical.

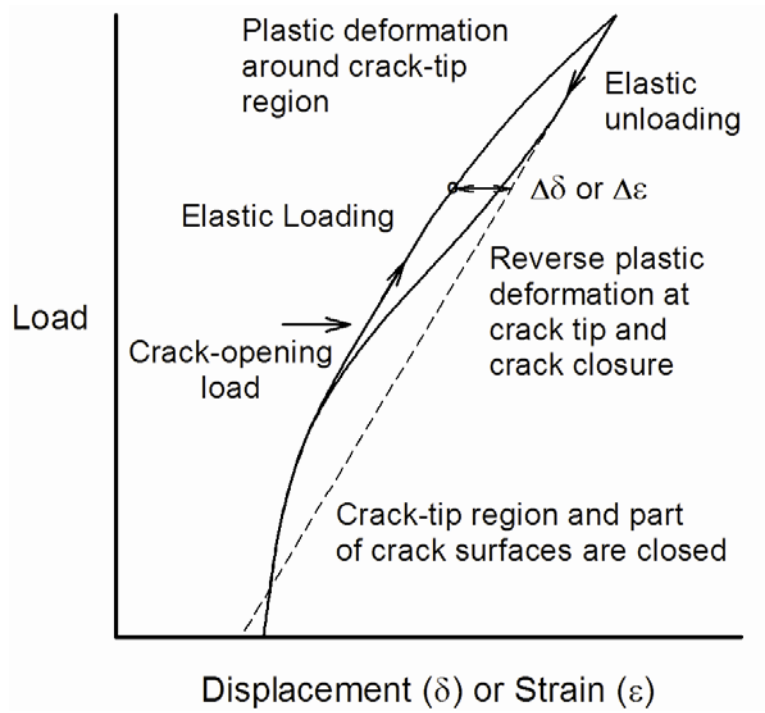

Figure A-2. Load Against Reduced Displacement or Strain Record

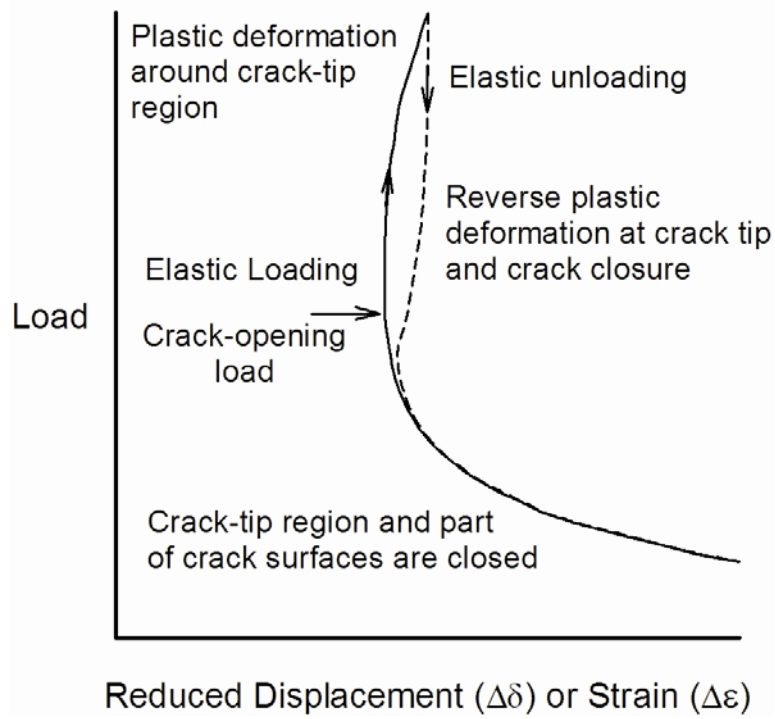

Figure A-3. Determination of Crack Opening (or Zero-Percent Offset) Load

A.4 AN EXAMPLE OF THE DETERMINATION OF THE CRACK OPENING LOAD.

A typical load-against-local (sideface) strain (P-ε) record during a compression precracking load reduction (CPLR) threshold test on a 7050-T7451 aluminum alloy C(T) specimen is presented in figure A-4 for R = 0.1 loading [A-9]. The sideface (local) strain gage was placed near the crack tip location (optimum locations were about one-half thickness in front of the crack tip location, but slightly off the anticipated crack path). The applied load has been normalized by the maximum applied load, P_{max}, and plotted against strain. The unloading compliance is constant at high loads (open crack), which appears as a linear section in the upper portion of figure A-4 and a solid line is fitted to only the upper portion of these data. Note that this straight line must be fitted to load strain data only above the crack opening load. Thus, a trial and error procedure must be used. As the load decreases, crack surfaces contact and produce a change in compliance.

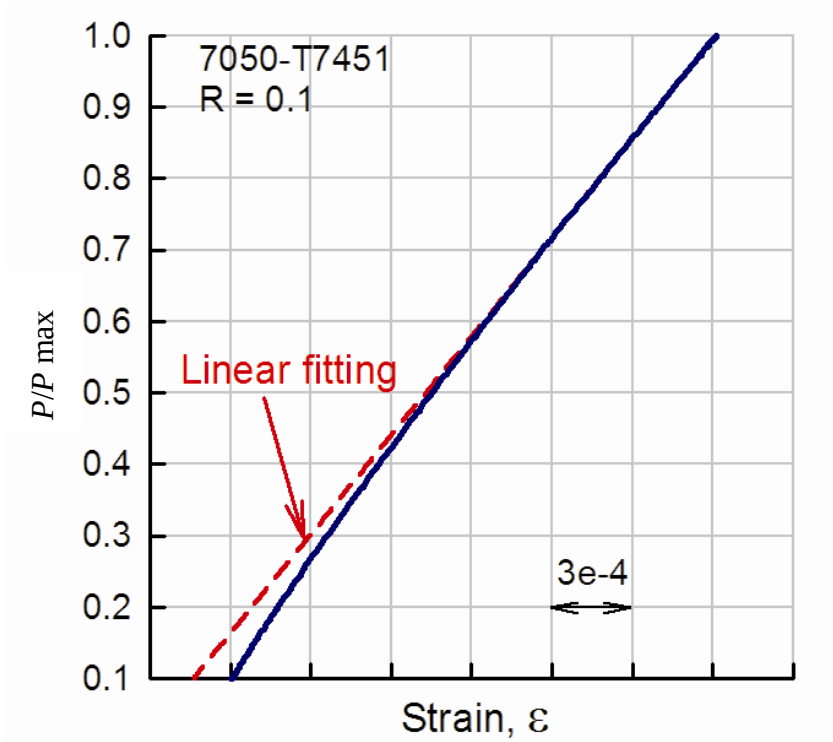

Figure A-4. Load-Against-Local Strain on a Compact Specimen Tested at Low-*R*

The reduced strain (or displacement) technique was developed to improve detection of these subtle compliance changes [A-6] during the crack closure and crack opening events. The reduced strain, $\Delta\varepsilon$, is the deviation from the crack closure-free compliance behavior. Closure-free behavior on these plots becomes a vertical line, making compliance deviations easier to detect from load-against-reduced-strain records. Using the reduced strain method, significant deviation is observed at low loads ($P/P_{max} < 0.7$) in figure A-5. In this case, the crack opening load ratio was 0.7. The very high crack opening load was suspected to have been caused by plasticity- and roughness-induced crack surface contact because the 7050 alloy developed a very rough fatigue crack surface.

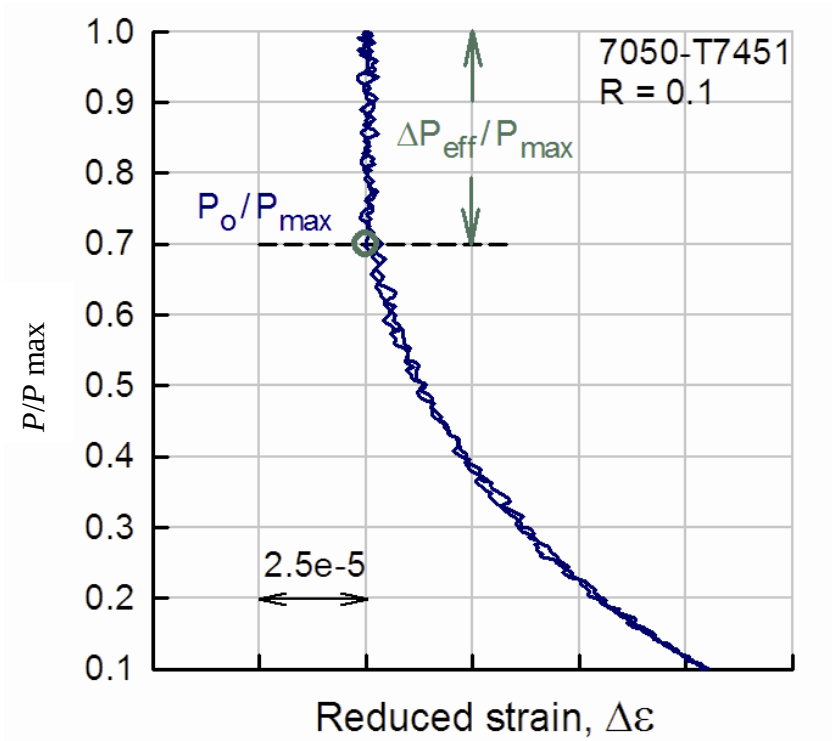

Figure A-5. Load-Against-Reduced Local Strain on a Compact Specimen Tested at Low *R*

A.6 REFERENCES.

A-1. Elber, W., "Fatigue Crack Closure Under Cyclic Tension," *Engineering Fracture Mechanics*, Vol. 2, 1970, pp. 37-45.

A-2. Elber, W., "The Significance of Fatigue Crack Closure," ASTM STP 486, American Society for Testing and Materials, Philadelphia, Pennsylvania, 1971, pp. 230-242.

A-3. Yisheng, W. and Schijve, J., "Fatigue Crack Closure Measurements on 2024-T3 Sheet Specimens," *Fatigue and Fracture of Engineering Materials and Structures Journal*, Vol. 18 1995, pp. 917-921.

A-4. Chermahini, R.G., Shivakumar, K.N., and Newman, J.C., Jr., "Three-Dimensional Finite-Element Simulation of Fatigue Crack Growth and Closure," *Mechanics of Fatigue Crack Closure*, ASTM STP 982, American Society for Testing and Materials, Philadelphia, Pennsylvania, 1988, pp. 398-413.

A-5. "Standard Test Method for Measurement of Fatigue Crack-Growth Rates," ASTM E-647, American Society for Testing and Materials, 2009.

A-6. Elber, W., "Crack Closure and Crack-Growth Measurements in Surface-Flawed Titanium Alloy Ti-6Al-4V," NASA-TN-D-8010, 1975.

A-7. Yamada, Y. and Newman, J.C., Jr., "Crack Closure Under High Load-Ratio Conditions for Inconel-718 Near Threshold Conditions," *Engineering Fracture Mechanics*, Vol. 76, 2009, pp. 209-220.

A-8. Yamada, Y. and Newman, J.C., Jr., "Crack-Closure Behavior of 2324-T39 Aluminum Alloy Near Threshold Conditions for High Load Ratio and Constant K_{max} Tests," *International Journal of Fracture*, Vol. 31, 2009, pp. 1780-1787.

A-9. Newman, J.C., Jr., Yamada, Y., and Newman, J.A., "Crack-Closure Behavior of 7050 Aluminum Alloy Near Threshold Conditions for Wide Range in Load Ratios and Constant K_{max} Tests," *Journal of ASTM International*, Vol. 7, No. 4, 2010.

APPENDIX B—STRESS INTENSITY FACTOR SOLUTION FOR CRACKS IN SINGLE-EDGE-NOTCH BEND SPECIMEN

B.1 INTRODUCTION.

The single-edge-notch bend (SEN(B)) specimen (figure B-1) was developed to perform fatigue and small crack testing using the equipment available in the Fatigue and Fracture Laboratory at Mississippi State University (MSU). Because all of the servohydraulic fatigue test frames at MSU use pin-loading clevises, a pin-loaded specimen was needed. The specimen design centered on modifying the single edge notch tension (SEN(T)) specimen, which has been a standard test specimen used to study the growth of small cracks in a variety of materials [B-1 through B-3]. In the new SEN(B) specimen, the loading pin diameter was undersized (D_{pin} = 0.96 D_{hole}) like the standard compact fatigue crack growth (FCG) test specimen to allow rotation of the specimen about the load line. The load centerline was oriented along the edge of the specimen with the notch, so that an induced bending moment would develop on the test section. In addition, the pinholes were beveled or counter-bored (B-4) to reduce any out-of-plane bending, which allows straighter crack fronts through the thickness.

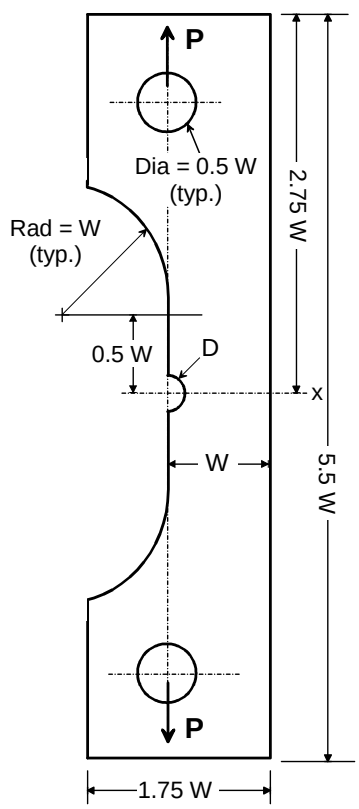

Figure B-1. SEN(B) (L = 5.5W) Specimen Subjected to Pin Loading

Because the SEN(B) specimen was used for conducting fatigue tests and monitoring the growth of small cracks emanating along the notch, the specimen configuration must allow for easy access to the notch surface for both visual inspection and for the application of notch surface replication material, such as acetate replicas. For this reason, it was important to consider how

the specimen configuration fits together with the test frame clevises. As seen in figure B-2, the SEN(B) configuration allows for easy access to the notch with no interference from the clevises.

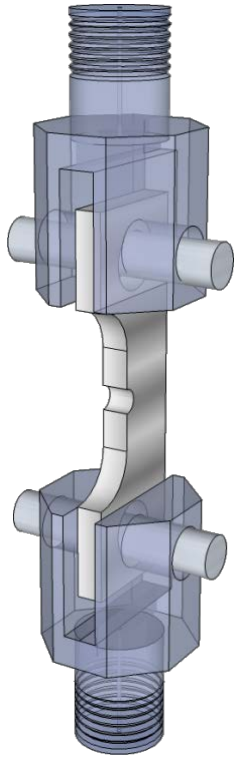

Figure B-2. The SEN(B) Specimen in a Pair of Clevises

The initial design for the SEN(B) specimen for the 9310 steel had a test section that was 25.4-mm (1-in.) wide (W) and a total specimen length (L) of 190.5 mm (7.5 in.). However, an opportunity arose for the SEN(B) specimen to be used on a 7050 aluminum alloy forging block that was only about 140 mm (5.5 in.) in a direction that would allow SEN(B) specimens in the longitudinal-transverse orientation. Desiring to retain the 25.4-mm test section, the specimen configuration was modified to include a change in the total length and pinhole diameter. Again, the load centerline was along the edge of the specimen with the notch. These modifications were made with the assumption that the changes would not alter the stress concentration factor at the notch or the stress intensity factors (K) for a surface or through cracks emanating from the notch. Having two complete sets of machined SEN(B) specimens, each set having a different configuration, necessitated performing a stress analysis for the new specimen with two different configurations.

B.2 STRESS CONCENTRATION FACTOR.

Because of the large amount of experience and test data on the AGARD fatigue and small crack SEN(T) test specimen [1 and 2], MSU wanted to develop a similar specimen. The AGARD small crack test specimen, shown in figure B-3, had a semicircular edge notch that had an elastic stress-concentration factor (K_t) of about 3.15 times the remote applied stress, $S = P/(WB)$, where WB is width times thickness, which simulated the stresses around a hole in an aircraft or

rotorcraft structure. The SEN(T) specimen was friction-gripped to carry the applied loads (the FADD2D boundary-element code [B-5] was used to determine the stress concentration factor). The edge notch allowed for easy access to the notch root surface to photograph or measure the small crack initiation sites and lengths. Several methods have been used to monitor small crack growth, such as plastic replicas, hot glue, and photographic or digital imaging.

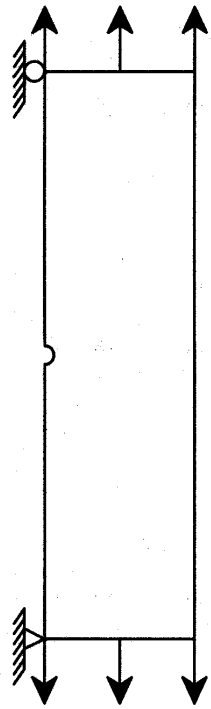

Figure B-3. AGARD Fatigue and Small Crack SEN(T) Test Specimen

Because the AGARD specimen was loaded by remote uniform stress (or uniform displacement), the load requirements for the materials to be tested in the current test program exceed the load capacity of the MSU test machines. Thus, a modified design was developed, which produced a high-stress concentration factor at the notch root with pin loading, as shown in figure B-4(a) (this figure is the FADD2D model to determine the local stresses around the semicircular-edge notch and the pin-loaded holes). The specimen is primarily a bend specimen with a small tensile component. The stress concentration factor is 2.95 times the nominal tensile stress plus bending stress (P/A + My/I) in a specimen without the notch or 11.8 times the nominal tensile stress $P/(WB)$. Thus, the new specimen is referred to as a SEN(B) specimen. To determine the normal stresses along the centerline of the specimen, the upper half of the specimen was analyzed with the FADD2D code, see figure B-4(b). A comparison of the normalized stresses acting on the centerline of the AGARD specimen and the new fatigue and small crack test specimen is shown in figure B-5. The normalized stress is σ_{yy} divided by the maximum tangential stress, σ_{max}, at the edge of the notch plotted against the distance along the centerline, x, normalized by the notch radius, r. Figure B-5(a) shows the normal stress distribution acting across the complete test section, while figure B-5(b) shows an expanded version for smaller x/r values. The stress gradients for small values of x/r were shown to be nearly the same in the two test specimens. This meant that the stress intensity factor equations that had previously been developed from the

National Aeronautics and Space Administration small crack program [B-3] could be modified for the new specimen design. In addition, a stress analysis was conducted on the new specimen design to verify the final stress intensity factor equations.

One major advantage of the SEN(B) specimen is a larger stress concentration at the notch, $K_t = \sigma_{max}/[P/(WB)] = 11.8$, compared to $K_t = \sigma_{max}/[P/(WB)] = 3.15$ for the SEN(T) specimen, where σ_{max} is the maximum notch root circumferential stress. This makes it possible to run a test at the same local stress level using a much lower applied load.

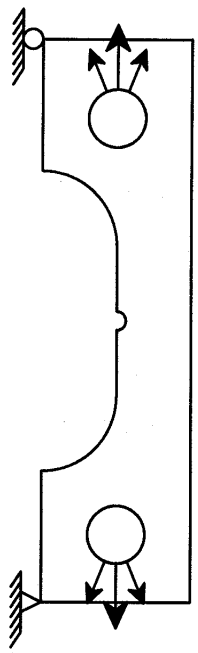

(a)

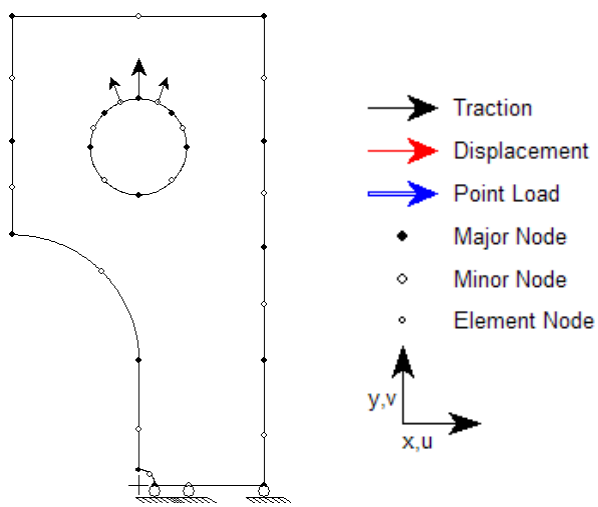

(b)

Figure B-4. (a) New Fatigue and Small Crack Test Specimen, SEN(B), Subjected to Pin Loading and (b) Upper Half of SEN(B) Specimen FADD2D Model Used to Determine Stress Distribution Along Centerline

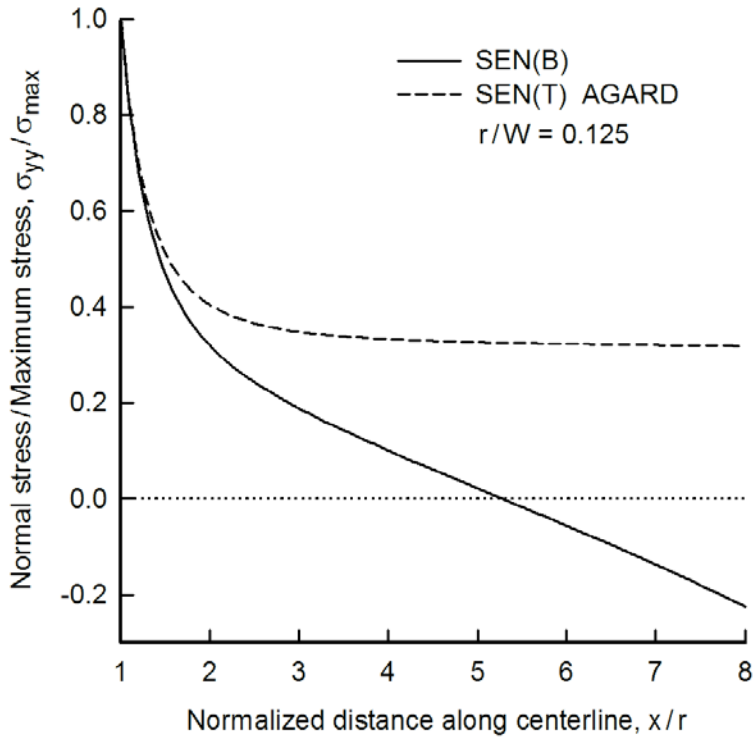

(a)

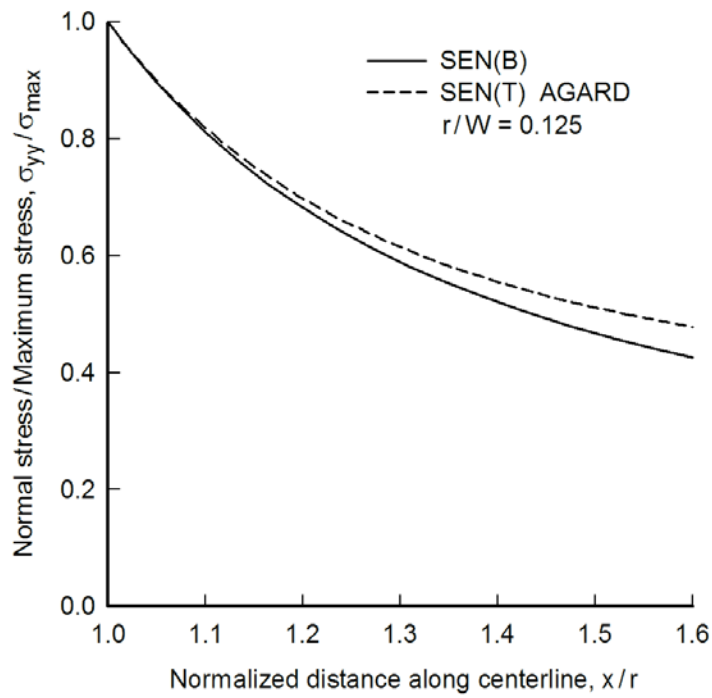

(b)

Figure B-5. (a) Normalized Stress Distribution Along Centerline of the Two Fatigue and Small Crack Test Specimens and (b) Expanded Normalized Stress Distribution Along Centerline of the Two Fatigue and Small Crack Test Specimens

B.3 CRACK STRESS INTENSITY FACTORS.

The goal of the stress analysis was to determine the stress intensity factor, *K*, for different through-the-thickness crack lengths measured from the edge of the notch, as shown in figure B-6. Once the *K* values for multiple discreet crack lengths were determined, a polynomial equation was fitted to the results to give a functional form for the stress intensity factor. In addition, a backface strain (BFS) gage relation was developed to monitor the cracking in the specimens during the fatigue tests. The BFS analyses are presented in section B.4.

B.3.1 TWO-DIMENSIONAL (THROUGH) CRACKS.

Elastic stress analyses began with creating a full boundary element model for the larger specimen with an overall length of L = 7.5W using FADD2D [B5]. The initial model contained a very fine mesh of boundary elements around the notch because this region would have a large stress gradient. An analysis was performed with no crack to determine the stress concentration factor at the notch. Next, a crack boundary was added to the model and the stress intensity factor was calculated for 18 different crack lengths ranging from very small to 80% of the ligament width. As the crack was lengthened, the distribution of boundary elements was altered to decrease the number of elements around the notch and increase the number of elements on the middle of the backface. This process was repeated for the smaller specimen (L = 5.5W) configuration (some typical models are shown in figure B-7 for both specimen sizes). Results showed that the difference between the stress concentration factors of the two specimens was about 0.4%. Also, the stress intensity factors for each crack length differ by less than ±0.5%. Thus, the two configurations have nearly identical stress fields.

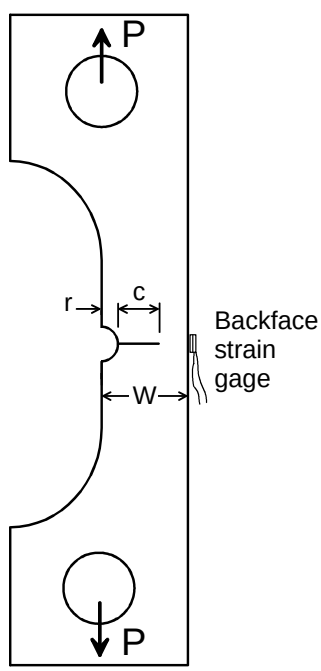

Figure B-6. New Fatigue and Small Crack Test Specimen, SEN(B), Subjected to Pin Loading

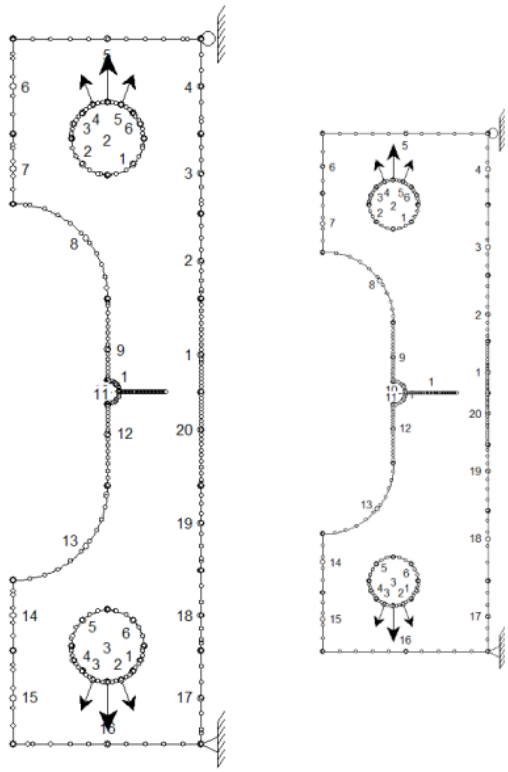

Figure B-7. FADD2D Models for 9310 Steel and 7050 Aluminum Alloy SEN(B) Specimens

The boundary element model solution is most accurate when the crack tip is not near another free boundary. Since the longest crack was only 80% of the ligament width, the effects of the crack tip approaching the backface were easily calculated. However, for very short cracks at the edge of the notch, the FADD2D results are less accurate and require a large number of elements. To accurately obtain the K solution for very short cracks, a limiting solution was determined. In the limit, as the crack length becomes extremely small, the crack should behave like an edge crack with remote loading equal to the concentrated stress and was accurately described by Irwin's solution for an edge crack in a semi-infinite plate [B-6]. To facilitate this calculation and make the curve-fitting process easier, the K values were normalized by the solution for a crack in an infinite plate, resulting in the boundary correction factor, F. The stress intensity factor expression is:

$$K = S\sqrt{\pi c}\,F \tag{B-1}$$

where $S = P/(WB)$ and B is the thickness of the specimen. B was 6.35 (0.25 inches) for all SEN(B) test specimens. For very short crack lengths:

$$K = S\sqrt{\pi c}\,F = 1.122\,\sigma\sqrt{\pi c} = S\,K_T\,1.122\sqrt{\pi c} \tag{B-2}$$

Therefore, as the crack length approaches zero, $F = 1.122\,K_t$. This data point was added to the data set as the value of the boundary-correction factor at zero crack length. The complete FADD2D results are shown in figure B-8.

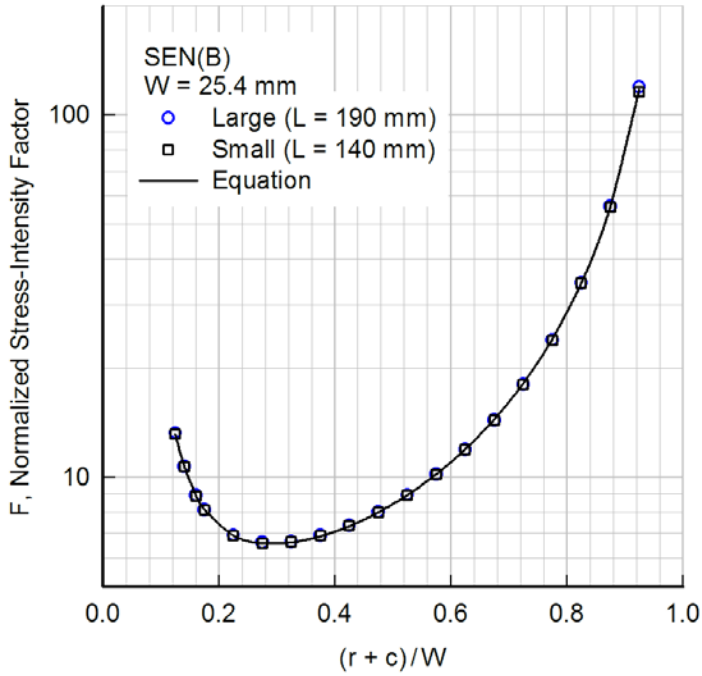

Figure B-8. Normalized Stress Intensity Factors for Both Specimen Configurations

Next, the task of fitting a polynomial to the data set had to be considered. It was decided that the curve fit should be similar to that of the SEN(T) specimen [B-1 and B-3], which defines the boundary-correction factor as the product of three separate polynomials. However, because the characteristic behavior of a bend specimen is different from a tension specimen, the boundary correction for the SEN(B) is defined as the product of four polynomials:

$$F\left(\frac{r}{W},\frac{c}{W},\frac{c}{r}\right) = f_1 g_4 f_b f_w \tag{B-3}$$

The function f_1 was taken directly from Newman et al. [B-3] and g_4 was adapted from the same work. These two polynomials modeled the behavior of short cracks from a circular notch in tension specimens:

$$f_1 = 1 + 0.358\,\lambda + 1.425\,\lambda^2 - 1.578\,\lambda^3 + 2.156\,\lambda^4 \tag{B-4}$$

$$g_4 = K_T\left(0.355 - 0.035\sqrt{\lambda}\right), \tag{B-5}$$

where

$$\lambda = \left(1 + \frac{c}{r}\right)^{-1} \tag{B-6}$$

The third polynomial modeled the behavior of long cracks in the bend specimens. The fourth polynomial was chosen to fit the data through a weighted least-square error-minimization fitting routine:

$$f_b = (1-\gamma)^{\frac{-3}{2}} \tag{B-7}$$

$$f_w = 0.975 - 1.154\,\gamma + 1.24\,\gamma^2 - 0.518\,\gamma^3, \tag{B-8}$$

where:

$$\gamma = \frac{r+c}{W} \tag{B-9}$$

The product of these four polynomials is a function that fits the FADD2D results within ±0.5%, which is about the difference between the two specimen configurations. The stress intensity factor equation is shown as the solid curve in figure B-8.

B.3.2 THREE-DIMENSIONAL (SURFACE) CRACKS.

During the fatigue testing of the SEN(B) specimens, fatigue cracks may initiate either as surface or corner cracks along the notch root. Previous studies on the SEN(T) specimen [B-3] indicated that the majority of cracks initiate as surface cracks for bare materials because of a slightly higher stress concentration factor at the center of the notch than at the edges (a clad material had predominately corner cracks [B-3]). Since only bare materials were considered in the present study, some approximate stress intensity factor equations were developed for a surface crack initiating and growing in the center of the notch root.

The SEN(B) specimen was used to conduct fatigue tests on a variety of materials. Normally, the fatigue process resulted in the initiation of surface cracks along the bore of the notch. Thus, it was important to be able to calculate the stress intensity factor for surface cracks and not just through cracks. Traditionally, this would have required performing three-dimensional stress analyses for both specimen geometries over a range of crack sizes (both crack depth, a, and crack length, c). Instead, the concept of similitude was applied to estimate the three-dimensional stress intensity factors.

A complete three-dimensional stress analysis was already available for the SEN(T) specimen, and the configuration similarities made it possible to use this information. Because surface cracks are present only for short crack lengths, the local stress fields for the tension and bending specimens could be assumed to be similar for surface cracks; the same local stress would produce the same three-dimensional stress intensity factor. Given the available equation for the three-dimensional boundary correction factor for the SEN(T) specimen and the two-dimensional boundary-correction factor equations for both the SEN(B) and SEN(T) specimens, an equation was developed to calculate the three-dimensional behavior of the SEN(B) specimen as:

$$K_{3DSEN(B)} = K_{3DSEN(T)}\,(K_{2DSEN(B)}/K_{2DSEN(T)}) \tag{B-10}$$

For very short cracks, the equation simplifies to include the ratio of stress concentration factors:

$$K_{3DSEN(B)} = K_{3DSEN(T)}\,(K_{TSEN(B)}/K_{TSEN(T)}), \tag{B-11}$$

Where $K_{TSEN(B)}$ is the elastic stress-concentration factor for SEN(B) specimen and $K_{TSEN(T)}$ is the stress concentration factor for SEN(T) specimen.

This similitude method was implemented inside the FASTRAN life prediction code for SEN(B) specimens for both 7050 aluminum alloy and 9310 steel. Once the code calculates that the crack has grown through the full thickness of the specimen ($a = t$), the similitude is no longer necessary and the K calculations rely entirely on the equations derived from the two-dimensional (through crack) stress analysis.

Figure B-9 shows the ratio of stress intensity factors for surface cracks and through cracks in the SEN(B) specimens as a function of crack depth to thickness (a/t) for various crack depth to crack length (a/c) ratios. Here K_{sc} is the average of the stress intensity factors at the free surface and maximum depth locations. These results show that as the crack depth approaches the sheet thickness, the average stress intensity factor approaches that for a through-thickness crack. An equation was found to fit these results as a function of a/t and a/c ratios.

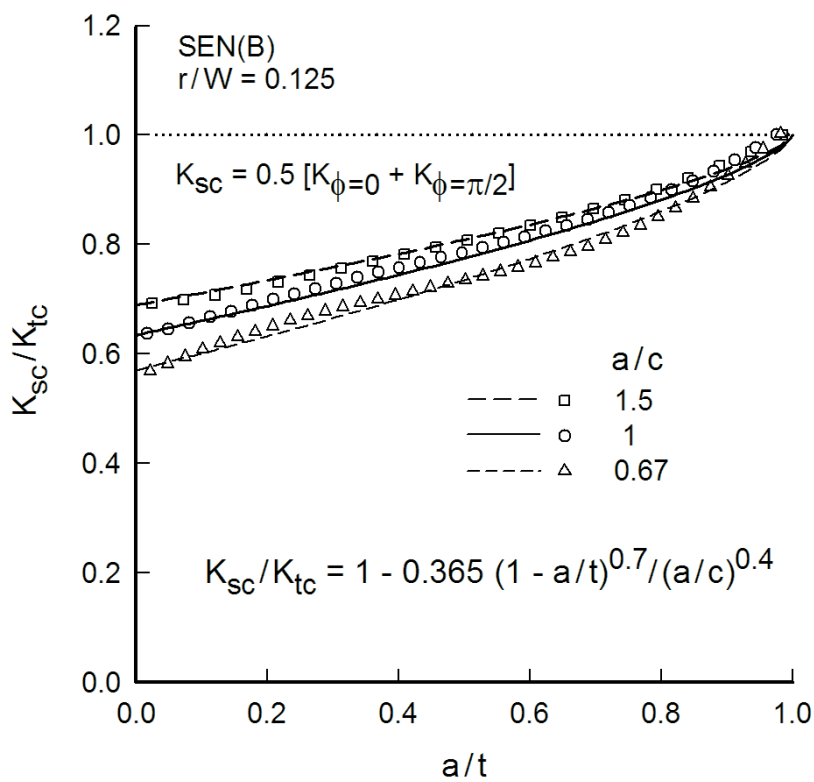

Figure B-9. Normalized Stress Intensity Factors for Both Specimen Configurations

Note that equation B-10 was programmed into the FASTRAN life-prediction code that allowed for independent crack growth in the crack depth (a) and crack length (c) directions.

B.3.3 COMPUTER CODE FOR SURFACE CRACK IN SEN(B) SPECIMEN.

The FORTRAN code, *SENB.for*, was developed and used to calculate the normalized stress intensity factors for a surface crack located at the center of the semicircular-edge notch in the SEN(B) specimen (sections of the *SENB.for* code have been incorporated into the FASTRAN life-prediction code as an option for predicting the fatigue lives of SEN(B) specimens using small crack theory). The semicircular-edge-notch radius (RAD), section width (W), and one-half sheet thickness (T) are input during the execution of the code. Total sheet thickness B is equal to 2T. The crack depth, *a*, is measured in the thickness direction, and the crack half length, *c*, is measured from the notch surface. The crack shape (a/c = crack depth to crack length) is input during the execution of the code, and the normalized stress intensity factors (*FA*, *FC*) are calculated for a wide range in *a*/*t* (crack depth to half-thickness) ratios. For a/t = 1 (a through crack), the code outputs the normalized stress intensity factor solution for a through crack in the SEN(B) configuration.

B.3.3.1 Example Input and Output Data File.

The example interactive input and the corresponding output data file are for a surface crack located at the center of a semicircular-edge notch in the SEN(B) specimen; RAD = 0.125, *W* = 1.0, T = 0.125 (*B* = 0.25), and AOC is input as 1.0 (note that consistent units must be used for all input parameters). In the output file, COW is crack length to width (*c*/*W*) ratio. AOT is crack depth to half thickness (a/t) ratio. FA is normalized stress intensity factor where the crack intersects the notch surface; FC is the normalized stress intensity factor at the maximum crack length from the notch surface in the width direction, *SENBtc* is the normalized stress intensity factor for a through crack of length *c*; and *F*ratio is the ratio of the average of FA and FC to the through crack solution (see section B.3.3.3).

B.3.3.2 Input Interactive Data.

1. ENTER OUTPUT FILENAME (like out1.txt) ?

   Input output filename with .txt extension.

2. RAD, *W*, *T* ?

   Input values of hole radius, RAD; width, *W*; and sheet half-thickness, *T*.

3. AOC ?

   Input value of AOC (a/c) ratio.

B.3.3.3 Output File.

```
SENB

     RAD= 0.125  W= 1.00  T= 0.125
     AOC= 1.000   <--------
```

```
   COW     AOT      FA          FC      SENBtc  Fratio
 0.1251  0.0008  0.2522E+00  0.2214E+00  0.374  0.633
 0.1261  0.0088  0.8251E+00  0.7200E+00  1.217  0.635
 0.1271  0.0168  0.1125E+01  0.9760E+00  1.649  0.637
 0.1281  0.0248  0.1350E+01  0.1164E+01  1.967  0.639
 0.1291  0.0328  0.1535E+01  0.1314E+01  2.220  0.642
 0.1301  0.0408  0.1692E+01  0.1439E+01  2.432  0.644
 0.1311  0.0488  0.1830E+01  0.1546E+01  2.612  0.646
 0.1321  0.0568  0.1954E+01  0.1640E+01  2.769  0.649
 0.1331  0.0648  0.2065E+01  0.1722E+01  2.908  0.651

    ... Data intentionally removed ...

 0.2451  0.9608  0.6288E+01  0.3004E+01  4.704  0.988
 0.2461  0.9688  0.6343E+01  0.3015E+01  4.708  0.994
 0.2471  0.9768  0.6399E+01  0.3027E+01  4.713  1.000
 0.2481  0.9848  0.6456E+01  0.3040E+01  4.718  1.006
 0.2491  0.9928  0.6514E+01  0.3053E+01  4.722  1.013
 0.2501  1.0000  0.0000E+00  0.4727E+01  4.727  1.000
 0.2511  1.0000  0.0000E+00  0.4732E+01  4.732  1.000
 0.2521  1.0000  0.0000E+00  0.4737E+01  4.737  1.000
 0.2531  1.0000  0.0000E+00  0.4742E+01  4.742  1.000

    ... Data intentionally removed ...

 0.8891  1.0000  0.0000E+00  0.6188E+02 61.879  1.000
 0.8901  1.0000  0.0000E+00  0.6271E+02 62.707  1.000
 0.8911  1.0000  0.0000E+00  0.6355E+02 63.554  1.000
 0.8921  1.0000  0.0000E+00  0.6442E+02 64.421  1.000
 0.8931  1.0000  0.0000E+00  0.6531E+02 65.308  1.000
 0.8941  1.0000  0.0000E+00  0.6622E+02 66.216  1.000
 0.8951  1.0000  0.0000E+00  0.6715E+02 67.145  1.000
 0.8961  1.0000  0.0000E+00  0.6810E+02 68.097  1.000
 0.8971  1.0000  0.0000E+00  0.6907E+02 69.071  1.000
 0.8981  1.0000  0.0000E+00  0.7007E+02 70.070  1.000
 0.8991  1.0000  0.0000E+00  0.7109E+02 71.093  1.000
```

B.3.3.4 FORTRAN CODE.

```
C SENB.for
C Program computes BCF for surface crack or through crack SENB specimen
C K = S (pi c*) F
C where c* = r + c and F is the BCF
C   NTYP=-14: Fsenb=Fsentsc(Fsenbtc/Fsenttc)
C   NTYP=-15: Fsenb=Fsenbtc
C     sc=surface crack;tc=through crack
C January 25, 2011
C-----------------------------------------------------------------------
C
      IMPLICIT REAL*8 (A-H,O-Z)
      CHARACTER*4 TITLE(20),TITLE1(20)
      CHARACTER*20 INFILE,OUTFILE
      REAL*8 M1,M2,M3
      TITLE1(1)="SENB"
C
```

```
      PRINT *,'ENTER OUTPUT FILENAME (like out1.txt) ?'
      READ(5,11) OUTFILE
   11 FORMAT(A20)
      OPEN(4,FILE=OUTFILE,STATUS='UNKNOWN')
C
      WRITE(4,15) TITLE1
   15 FORMAT(1X,19A4)
c RAD=hole radius; W=width; T=one-half thickness
      PRINT *,'RAD, W, T ?'
      READ(5,*) RAD,W,T      WRITE(4,20) RAD,W,T
   20 FORMAT(5X,'RAD=',F6.3,2X,'W=',F5.2,2X,'T=',F6.3)
C
   19 PRINT *,'AOC ?'
      READ(5,*) AOC
      WRITE(4,21) AOC
   21 FORMAT(5X,'AOC=',F6.3,3X,'<--------')
C
      Q=1.+1.464*AOC**1.65
      IF(AOC.GT.1.0) Q=1.+1.464*AOC**(-1.65)
C     BREFF IS USED TO REDUCE 3D SIF (0 TO 10 PERCENT) AT FREE SURFACES
c      R=SMINSP/SMAXSP
c      BREFF=0.9+0.2*R**2-0.1*R**4
c      IF(R.LT.0.0) BREFF=0.9
      BREFF=1.0
C
C c* = r + c
C COW = (r+c)/w = r/w + c/w
C
      WRITE(4,22)
   22 FORMAT(/4X,'COW',5X,'AOT',6X,'FA',10X,'FC',
     1 6X,'SENBtc',2X,'Fratio')
      DCOW=0.001
      COW=RAD/W-DCOW+0.0001
   30 COW=COW+DCOW
      IF(COW.GT.0.9) GOTO 999
      C=COW*W-RAD
      A=AOC*C
      AOT=A/T
      IF(A.GT.T) AOT=1.0
      IF(A.GT.T) A=T
      DRP=0.0
      B=A+DRP
      CX=C+RAD
      D=CX+DRP
      PI=3.14159
      PIW=0.5*PI/W
c      write(4,111) A,C
c  111 format(2X,'A=',e11.4,2X,'C=',e11.4)
      IF(A.GE.T) GOTO 1415
C
C*** SURFACE CRACK CENTER SEMI-CIRCULAR EDGE NOTCH BEND (NTYP=-14) ***
C    Pin-loaded (S = P/(WB))
C-----------------------------------------------------
C*** New NTYP = -8 for RAD/W = 0.125 ***  UNIFORM STRESS
 1400 Z=D/W
      DOW=Z
      IF(DOW.GT.0.9) GOTO 990
```

```
      FW=0.912-1.10*Z+3.83*Z**2-4.9*Z**3+2.28*Z**4
      FB=(1-Z)**-1.5
      Z=RAD/D
      XKT=3.41
      F2=XKT*(0.36-0.032*DSQRT(Z))
      G1=1.+0.358*Z+1.425*Z**2-1.578*Z**3+2.156*Z**4
      G2=G1*DSQRT(1.-Z)
c      FC8=FW*XKT
      FC8=F2*G2*FW*FB
C*** NTYP = -15 ***
      Z=D/W
      DOW=Z
      IF(DOW.GT.0.9) GOTO 990
      FW=0.962-1.178*Z+1.307*Z**2-0.554*Z**3
      FB=(1-Z)**-1.5
      Z=RAD/D
      XKTB=11.8
      F2=XKTB*(0.36-0.032*DSQRT(Z))
      G1=1.+0.358*Z+1.425*Z**2-1.578*Z**3+2.156*Z**4
      G2=G1*DSQRT(1.-Z)
c      FC15=FW*XKTB
      FC15=F2*G2*FW*FB
      FC158=FC15/FC8
C ---------------------------------------------------
      IF(AOC.GT.10.) GOTO 990
      IF(AOC.LT.0.1) GOTO 990
      Z=RAD/T
      ROT=Z
      IF(ROT.LT.0.5) GOTO 990
      IF(ROT.GT.3.5) GOTO 990
      M1=1.0
      M2=0.05/(0.11+AOC**1.5)
      M3=0.29/(0.23+AOC**1.5)
      G1A=1.0
      Z=1./(1.+0.1564*(D-RAD)/RAD)
      G2A=FHOLE(Z)/(1.+0.08*Z**2)
      G1C=1.-AOT**4*(2.6-2.*AOT)**0.5/(1.+4.*AOC)
      Z=RAD/D
      G2C=FHOLE(Z)/(1.+0.08*Z**2)
      FPHIA=1.0
      IF(AOC.GT.1.0) FPHIA=1.0/DSQRT(AOC)
      FPHIC=1.0
      IF(AOC.LE.1.0) FPHIC=DSQRT(AOC)
      G3=1.+0.1*(1.-AOT)**10
C*** New NTYP = -7 for RAD/W = 0.125  *** UNIFORM STRESS
 1401 Z=RAD/W
      ROW=Z
      IF(ROW.LT.0.05.OR.ROW.GT.0.195) GOTO 990
      IF(AOC.GT.1.0) M1=1./DSQRT(AOC)*(1.04-.04/AOC)
      FO=(M1+M2*AOT**2+M3*AOT**4)*DSQRT(AOT*T/(D*Q))
      XKT=3.41
      G4=XKT*(0.36-0.032/DSQRT(D/RAD))
      G5A=1.+DSQRT(AOC)*(0.003*ROT**2+0.035*ROT)
      G5C=1.+DSQRT(AOC)*0.003*ROT**2-0.35*AOT**2*(1.-0.5*AOC)**3
      Z=DSQRT(AOT)*(D-RAD)/W + RAD/W
C  UNIFORM STRESS
      FW=0.912-1.10*Z+3.83*Z**2-4.9*Z**3+2.28*Z**4
```

```
      FB=(1-Z)**-1.5
      FWC=FW*FB
      FA=FO*FWC*G1A*G2A*G3*FPHIA*G4*G5A*BREFF*FC158
      FC=FO*FWC*G1C*G2C*FPHIC*G4*G5C*FC158
C      write(4,333) Fsenba,Fsenbc,fc158,fa,fc
c  333 format(2x,5(2x,e10.3))
      GOTO 5
C*** THROUGH CRACK AT SEMI-CIRCULAR EDGE NOTCH BEND (NTYP = -15) ***
 1415 Z=D/W
      DOW=Z
c     IF(DOW.GT.0.9) GOTO 990
      FW=0.962-1.178*Z+1.307*Z**2-0.554*Z**3
      FB=(1-Z)**-1.5
      Z=RAD/D
      XKTB=11.8
      F2=XKTB*(0.36-0.032*DSQRT(Z))
      G1=1.+0.358*Z+1.425*Z**2-1.578*Z**3+2.156*Z**4
      G2=G1*DSQRT(1.-Z)
      FC=F2*G2*FW*FB
      FA=0.0
C-------------------------------
    5 CONTINUE
C
C*** NTYP = -15 ***********************************
      Z=D/W
      DOW=Z
c     IF(DOW.GT.0.9) GOTO 990
      FW=0.962-1.178*Z+1.307*Z**2-0.554*Z**3
      FB=(1-Z)**-1.5
      Z=RAD/D
      XKTB=11.8
      F2=XKTB*(0.36-0.032*DSQRT(Z))
      G1=1.+0.358*Z+1.425*Z**2-1.578*Z**3+2.156*Z**4
      G2=G1*DSQRT(1.-Z)
      FC15=F2*G2*FW*FB
C**************************************************
C
      Fratio=0.5*(FA+FC)/FC15
      IF(AOT.GE.1.0) Fratio=1.0
      WRITE(4,1499) COW,AOT,FA,FC,FC15,Fratio
 1499 FORMAT(1X,F7.4,1X,F7.4,1X,e11.4,1X,e11.4,1X,F6.3,1X,F6.3)
      GOTO 30
  990 WRITE(4,998) AOC,ROT,ROW,DOW
  998 FORMAT(/5X,'LIMIT EXCEEDED', 4(2X,F7.4))
  999 STOP
      END
C
      REAL*8 FUNCTION FHOLE(Z)
      IMPLICIT REAL*8 (A-H,O-Z)
      FHOLE=1.+0.358*Z+1.425*Z**2-1.578*Z**3+2.156*Z**4
      RETURN
      END
C
```

B.4 BACKFACE STRAIN RELATION.

A crack monitoring system [B-7] and a backface strain (BFS) gage were used to automate the fatigue tests on the SEN(B) specimens (as shown in figure B-6). The normalized backface strain, $|\varepsilon EBW/P|$, is plotted against the hole radius plus crack length-to-width, $(r + c)/W$, ratio. Two methods were used to determine the BFS: (1) displacement, δ, over a very small gage length, L (or $\varepsilon = \delta/L$) and (2) normal stress at the centerline ($\varepsilon = \sigma_{yy}/E$). The equation that was developed had the same functional form as that used in ASTM E-647 [8] for the crack mouth opening displacement (CMOD) method. The BFS relation developed and used is:

$$(r + c)/W = A_0 + A_1 U + A_2 U^2 + A_3 U^3 + A_4 U^4 + A_5 U^5 \qquad \text{(B-10)}$$

for $0.125 < (r + c)/W < 0.9$, where $U = 1/[A^{1/2} + 1]$ and $A = |\varepsilon EBW/P|$. The coefficients are:

$A_0 = 1.024$ $A_1 = -3.225$ $A_2 = 13.79$ $A_3 = -90.08$ $A_4 = 264.73$ $A_5 = -282.46$

The solid curve shows equation B-10. Also shown for comparison is The ESE(T) specimen using an equation (dashed curve) developed by Johnston et al. (2009) at the NASA Langley Research Center. The ESE(T) equation was independently verified by using the FADD2D boundary element code (open-square symbols).

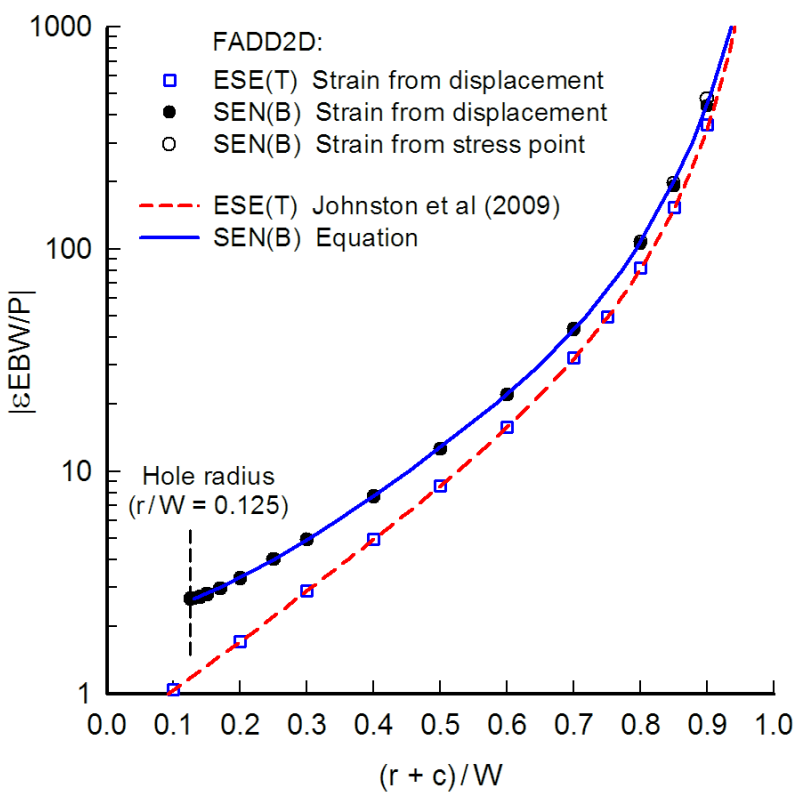

Figure B-9. Normalized BFS and an Equation for SEN(B) Specimen as a Function of $(r + c)/W$ Ratio

B.5 REFERENCES.

B-1. Newman, J.C., Jr. and Edwards, P.R., "Short-Crack Growth Behaviour in an Aluminum Alloy—An AGARD Cooperative Test Programme," AGARD Report No. 732, 1988.

B-2. Edwards, P.R. and Newman, J.C., Jr., eds., "Short-Crack Growth Behavior in Various Aircraft Materials," AGARD Report No. 767, 1990.

B-3. Newman, J.C., Jr., Wu, X.R., Venneri, S.L., and Li, C.G. "Small-Crack Effects in High-Strength Aluminum Alloys" *NASA Reference Publication 1309*, May 1994.

B-4. Newman, J.C., Jr., Yamada, Y., and Newman, J.A., "Crack-Closure Behavior of 7050 Aluminum Alloy Near Threshold Conditions for Wide Range in Load Ratios and Constant *K*max Tests," *Journal of ASTM International*, Vol. 7, No. 4, 2010.

B-5. Chang, C.C. and Mear, M.E., "A Boundary Element Method for Two-Dimensional Linear Elastic Fracture Analysis," *International Journal of Fracture*, Vol. 74, 1996, pp. 219-251.

B-6. Tada, H., Paris, P.C., and Irwin, G.R., "The Stress Analysis of Cracks Handbook," 3rd edition, The American Society of Mechanical Engineers, 2000, p. 52.

B-7. Donald, J.K., "A Procedure for Standardizing Crack Closure Levels," ASTM STP-982, American Society for Testing and Materials, Philadelphia, Pennsylvania, 1988, pp. 222-229.

B-8. Standard Test Method for Measurement of Fatigue Crack Growth Rates, ASTM E-647, American Society for Testing and Materials, 2009.

APPENDIX C—MACHINING AND HEAT TREATMENT PROCEDURES FOR 9310 STEEL SPECIMENS

C.1 INTRODUCTION.

The Boeing Company provided a 9310 steel rod (150-mm diameter by 750-mm long). Boeing also provided standard machining and heat-treatment procedures of the carburized 9310 steel. The large steel rod is shown in the upper insert in figure C-1. The rod was cut into four blocks. Each block had the same pattern of specimens machined in the same orientation (see figure C-1). Compact, C(T), single-edge-notch bend (SEN(B)), and tensile specimens were machined from the rod in the longitudinal direction of maximum grain flow orientation, as shown in figure C-2, and heat treated by procedures described below.

C.2 MACHINING REQUIREMENTS.

A reference centerline was marked on the complete rod, as shown in figure C-1. The round rod was cut into four blocks (A, B, C, and D). Each block was 150 mm (6 in.) in diameter by roughly 230 mm (9 in.) in length. From each block, a number of blanks (17) were machined (each blank was labeled with the blank number) and the thickness of each blank was roughly 11 mm (0.45 in.). Blanks were roughly perpendicular to the reference centerline plane, as shown. The total number of blanks was 68. After rough cutting the blanks, heat treatment on all blanks was performed as described below.

C.3 HEAT TREATMENT REQUIREMENTS.

(1) Rough machine specimen blanks from rod that are 11mm (0.45 in.) thick (final thickness of 6.35 mm (0.25 in.)).
(2) Pseudocarburize 1700°F for 4 to 6 hours, cool to 1500°F, then air cool to room temperature.
(3) Subcritical anneal at 1250°F for 3 hours (within 5 hours after pseudo-carburization).
(4) Harden at 1525°F for one hour, oil quench.
(5) Freeze within 30 minutes of hardening. Freeze at -110°F for 3 hours minimum.
(6) Draw (temper) at 300°F for 2 hours minimum. Hardness should be 34-42 R_c.
(7) Second draw (temper) at 300°F for 2 hours minimum. Hardness should be 34-42 R_c.
(8) Final machine and grind to final dimensions.
(9) Nital etch inspect for grinding burns.

C.4 TEST SPECIMENS.

Figure C-2 shows the layout of the respective blanks that were subsequently machined into C(T), SEN(B), and tensile specimens. This pattern was repeated for the other three blocks. There was a total of 24 C(T) specimens, 36 SEN(B) specimens, and 8 tensile specimens. Unfortunately, the tensile specimens were not tested because of the lack of test equipment at Mississippi State University.

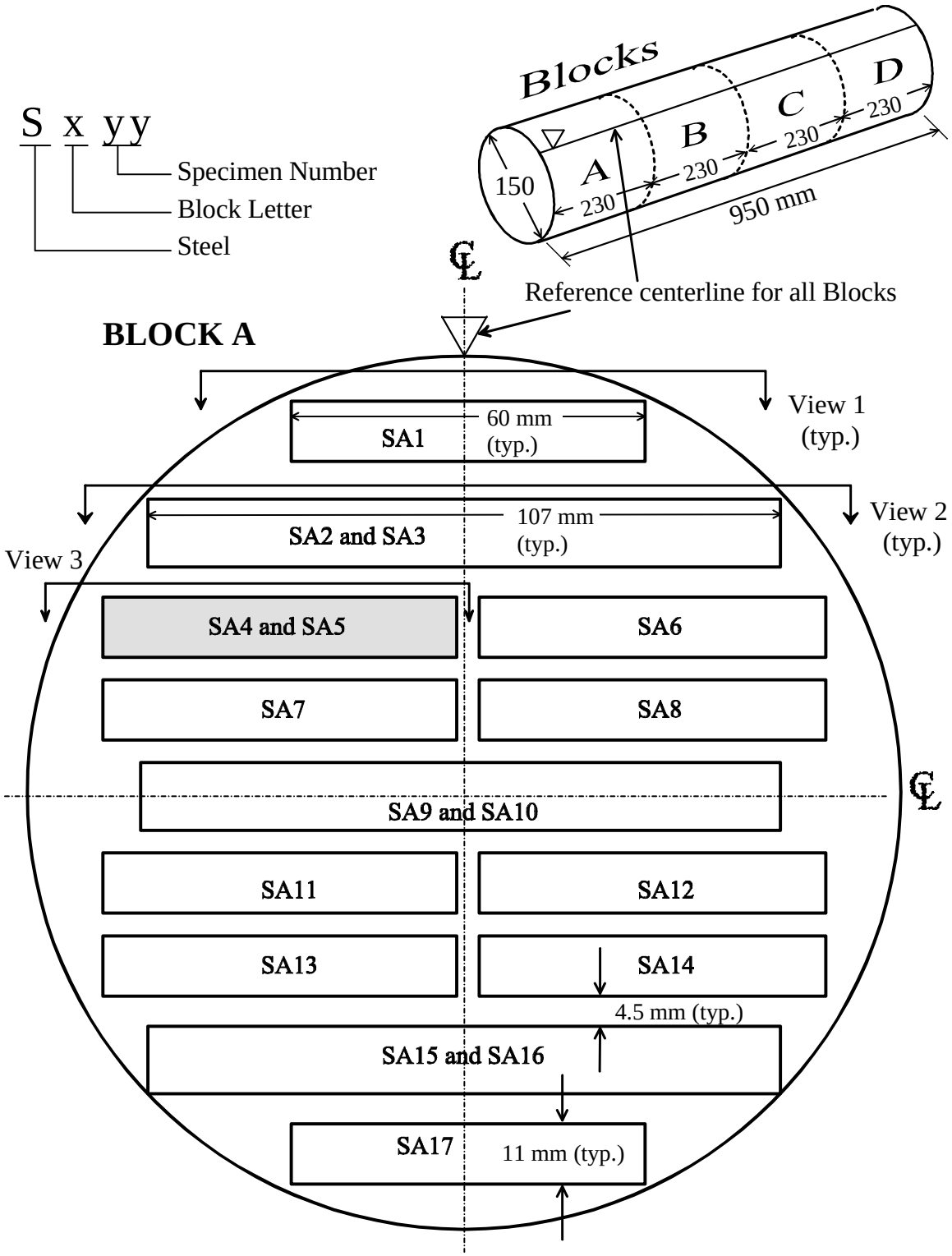

Figure C-1. Specimen Layout for Block A (typical)

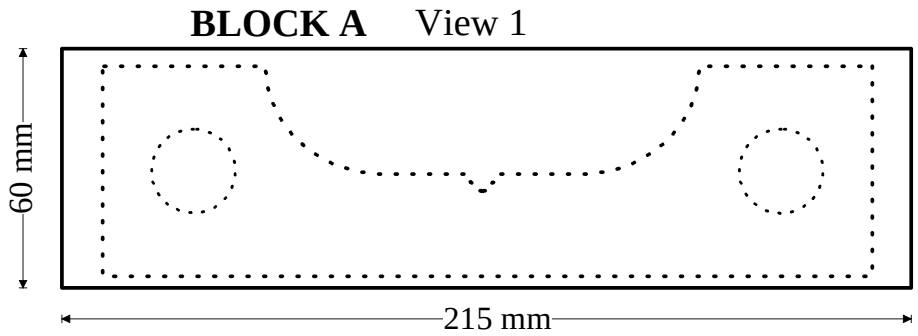

(a) SEN (B) specimen (SA1, 6, 7, 8, 11, 12, 13, 14, and 17)

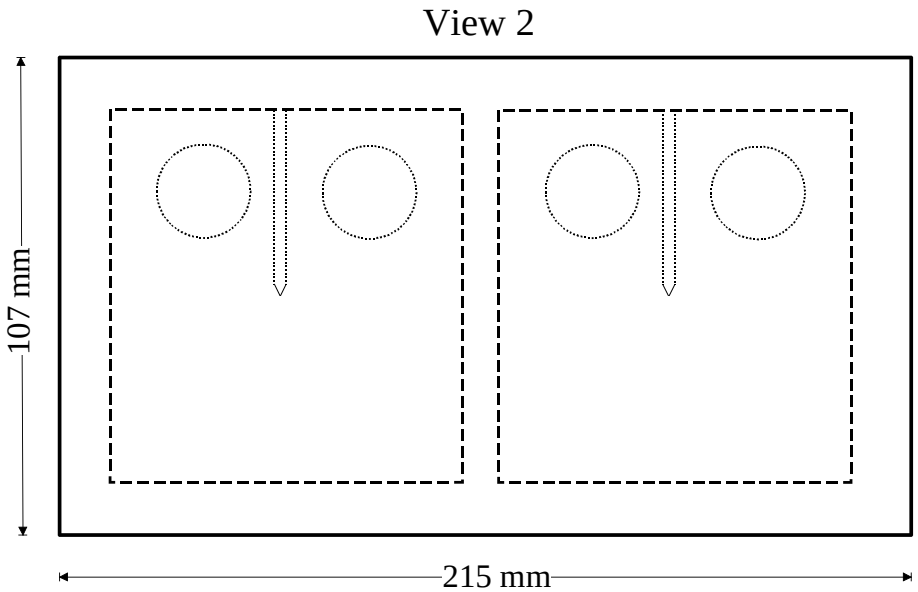

(b) C(T) specimens (SA2, 3, 9, 10, 15, and 16)

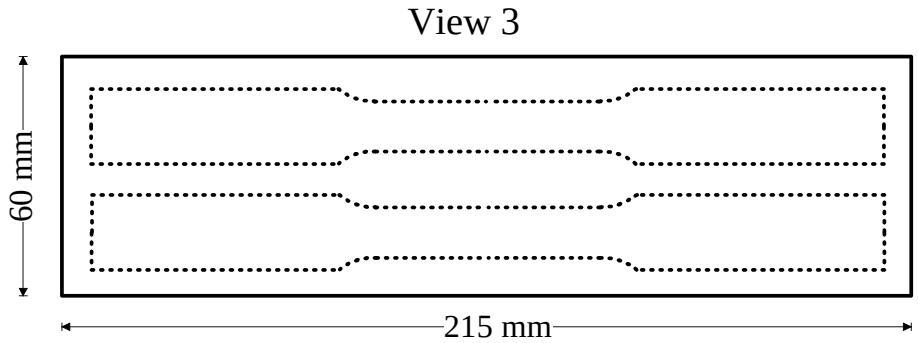

(c) Tensile specimens (SA4 and 5)

Figure C-2. C(T), SEN(B), and Tensile Specimens (typical)